FINITE ELEMENT ANALYSIS FOR THE DESIGN OF NOVEL CERAMIC PROPELLERS

By

KATELYNN HARMON

Bachelor of Science in Mechanical Engineering
Oklahoma Christian University
Edmond, Oklahoma
2017

Submitted to the Faculty of the
Graduate College of the
Oklahoma State University
in partial fulfillment of
the requirements for
the Degree of
MASTER OF SCIENCE
DECEMBER, 2022

FINITE ELEMENT ANALYSIS FOR THE

DESIGN OF

NOVEL CERAMIC PROPELLERS

Thesis Approved:

Dr. Jamey Jacob

Thesis Advisor

Dr. Ranji Vaidyanathan

Dr. Shuodao Wang

ACKNOWLEDGMENTS

Thank you to everyone who supported me and encouraged me along the way, so that I could know that the journey that took longer than expected offers no less joy at the end.

Name: KATELYNN HARMON

Date of Degree: DECEMBER, 2022

Title of Study: FINITE ELEMENT ANALYSIS FOR THE DESIGN OF NOVEL CERAMIC PROPELLERS

Major Field: MECHANICAL AND AEROSPACE ENGINEERING

Abstract:

Ceramics are stiff, lightweight and less prone to deflection. However, ceramics have not historically been used in propeller applications. Little is known about how ceramics will react to the various loading situations of the application. Finite Element Analysis (FEA) was performed to simulate the loading due to thrust, torque and centrifugal forces on various blade geometries. The first geometry was based on a physical test assembly made from commercially available ceramic knives. Additional geometries were created based on the scan data of a known propeller, and then removing aspects of the blade-the airfoil and the twist. Each geometry was iterated to failure for each loading mechanism. The thrust and torque distribution was determined for each blade geometry at 12,000 RPM. The combined loading for all mechanisms was simulated at this rotational speed. The blade twist lowered the deflection in centrifugal loading and the added thickness of an airfoil increased the structural integrity of the blade in flexural loading. Minimal deflection was experienced by the blade design with both a twist and an airfoil.

TABLE OF CONTENTS

LIST OF TABLES

LIST OF FIGURES

CHAPTER I

INTRODUCTION

Small, unmanned aerial systems (SUAS) have a multitude of potential applications ranging from surveillance to conservation efforts. Some of the limitations of these systems come from the effectiveness of the propellers. Efficiency losses are experienced when the propellers bend. Higher noise levels can be expected when the propellers are too heavy. Therefore, there is a need to have high efficiency, stiff, propellers that are also lightweight and generate less noise.

Ceramics were identified as a material to be explored to meet this criteria. Ceramics have a high modulus and are very stiff, meaning they are less prone to deflection. They are lightweight and will not produce as much noise. Additionally, ceramics are resistant to weathering and not subject to corrosion and UV degradation in the way metals and plastics are. However, ceramics have not historically been used in these types of applications. Little is known about how they will behave or react to the many forces acting on them in this application. Hydronalix and OSU have partnered to fabricate, simulate, test and optimize thin-airfoil ceramic propellers [27].

1.1 Thesis Goals and Objectives

1.1.1 Overall Goal

Little is known about how ceramics will perform as propellers. The overall goal of this project is to understand the structural constraints of using this material in this application. Finite

Element Analysis will be performed to understand how the material will behave under the expected forces and to understand the risks associated with the various loading mechanisms during the design process. Additionally, the effect of blade geometry will be studied in regards to failure in the direction of expected loading conditions.

1.1.2 Goal 1: Model the Propellers

The first goal is to analyze an existing propeller and create a 3D model of the part that will allow for the creation of additional geometries.

Objectives

- Measure current designs through 3D scan data
- Section and create airfoil curves for each plane
- Validate 3D-scanner with known airfoil
- Create multiple blade geometries

1.1.3 Goal 2: Finite Element Analysis

With 3D models available for multiple geometries, FEA will be performed to simulate various expected loads and understand the changes in failure modes between different geometries.

Objectives

- Test Assembly
    - -Simulate loading conditions
    - -Determine displacement and failure modes
- Propeller blade geometry analysis

-Simulate loading conditions

-Determine displacement and failure modes

-Compare failure modes based on blade type

1.1.4 Goal 3: Implications for Manufacturing

Determine how the FEA results can help inform the manufacturing process.

Objectives

- Understand current material selection constraints within the application
- Determine structural advantages of blade geometry selection
- Evaluate alternative material options for this application

CHAPTER II

LITERATURE REVIEW

Previous work on propellers, Small Unmanned Aerial Systems (SUAS) and unmanned aerial vehicles (UAVs) was explored. Current and advanced manufacturing options of ceramics were reviewed, including advantages and limitations. Alternate materials and their relative advantages and disadvantages were explored as well.

2.1 Previous Work

Previous relevant work involving propellers, UAVs and SUAS were explored and relevant findings reviewed.

2.1.1 Propeller Noise Reduction

Designing aircraft for a low sound pressure level (SPL) can have significant performance reductions [19]. But lowering the SPL has advantages for the general public, such as lower noise around airports in higher populated areas. Additionally, lowering the minimum altitude would allow for more traffic without the added noise. Lowering the propeller noise is not the only way to reduce the acoustic profile of an aircraft. There are other factors that add to the SPL, such as the engine and the exhaust. However, the propeller is the dominant contributor to the noise. Most unmanned aerial vehicles are propeller driven.

The main contributors to the SPL in a propeller come from the blade thickness and load-

ing. Reducing the tip mach number will reduce the overall noise. Lowering the SPL while retaining performance was studied for three, four and five-blade configurations. XROTOR software was used to generate 2-D geometries. This software has a function that allows for blade modification and design, but does not account for atmospheric noise, only the noise due to thickness and loading of the propeller blades. It was was determined that the design options to reduce the SPL were blade number, radius, RPM, chord ratio, thickness, twist distribution and airfoil shape. The optimal propellers from the 3 configurations were compared to a reference propeller. The five-blade configurations offered the lowest drop in performance for the highest reduction in noise level, showing a 1.4% performance penalty for a 33.8% reduction in SPL.

A secondary analysis was performed as a purely theoretical analysis with the aim of dropping the performance to understand the limits of noise reduction. In this analysis, the RPM was dropped until the performance dropped below 20%. The tip mach number was lowered to 0.359 and the SPL reduced to 38dB at 1000'AGL. The theoretical configuration was not analyzed for safe operational values.

2.1.2 Composite SUAS Propellers

Small unmanned aerial systems have applications ranging form military purposes to wildlife monitoring. The acoustic signature of these aircraft is a limiting factor in many of these applications. To combat this undesired effect, a unique method was developed to create multi-bladed optimized composite propellers [4]. The aim of the study was to create quiet, optimal propellers using simple manufacturing techniques.

With the goal of maintaining propeller efficiency while reducing noise, the propellers were designed. Two configurations were optimized- a 3-blade and a 5-blade propeller. SolidWorks was used to generate a model of the desired multi-blade propeller. Airfoil geometries were imported and the the airfoil surfaces were lofted with guide curves to to achieve a single

blade. This was used to create the full propeller model for both configurations.

To manufacture the propellers, molds were created. The previously discussed model was used to create a mold geometry. This geometry was used to create a tool path for CNC processing and subsequent mold creation. Then carbon-fiber composite propellers were created through a wet-layup process. Finally, the end propeller was finished and balanced.

The finished propellers were tested past theoretical performance parameters in a wind tunnel with a dynamometer. The dynamometer evaluated the torque, thrust and RPM. A second test was performed to measure the tip deflection of the blades. The 5-bladed propeller experienced vibration effects with the gas-motor set-up. This effects the performance negatively and damages the propeller. This was not the case for the 3-blade propeller or when tested with an electric motor. Overall, both configurations performed efficiently with an electric motor set-up and the manufacturing process was successful.

2.1.3 3D Scanning for UAS Propeller Design

Modular UAS components were 3D scanned in order to replicate the design and replace in existing platforms [13]. This was due to the difficulties in understanding an existing airfoil through measurements alone. Multi-stripe laser triangulation (MLT) was used on an existing wing section. Then a coordinate measuring machine was used to measure the same airfoil section. When this was super-imposed, it showed differences in the mid-chord to trailing edge sections of the airfoil. This required minor adjustments to be made to the coordinates obtained in the 3D-scanned file. This highlights the importance of validating the scanned data.

2.2 Ceramics

2.2.1 Advanced Manufacturing

Traditional manufacturing of ceramics has it's limitations. Post-hard machining of ceramics is time-consuming, expensive and requires specialized equipment [31]. The expense is estimated to be 80% of the total cost to manufacture a part. This makes additive manufacturing options for ceramics particularly appealing. AM methods generally include processing geometrical information and then controlling the layer-by-layer deposition of the material. Each layer is adhered to the next by various processes, including curing, binding, deposition and sintering. Much of AM research has been focused on polymers and metals, with relatively few options for ceramics. Some applications developed for other materials have been adapted for ceramics as well.

Three-dimensional printing (3DP) includes both direct and indirect techniques. Direct printing (DIP) deposits ceramic material via a nozzle, is fast, efficient and useful for complex shapes. The accuracy of the dimensional resolution is affected by the printing parameters. This is the only AM process for ceramics that allows for dense parts without post processing. DIP has also been used for coatings.

Indirect printing techniques are used as well. In this case, a binder liquid is distributed on a powder bed. This method can be used for complex shapes and overhangs. Thinner layers create finer resolution parts. There is high porosity in such printed parts due to the layer thickness and the packing density of the powder.

Selective Laser Sintering (SLS) is the process of fusing particles in a powder bed with a laser. This pattern is defined by a CAD model that has been sliced into layers. Thermoplastics are easier in this process due to low melting temperatures. High-melting temperature materials, such as certain metals and ceramics, are not as easy to process. Ceramics also possess low thermal shock resistance, which predisposes them to cracking in the manufacturing process.

Direct sintering has been explored less than other types due to the poor densification of parts manufactured with this method. Higher density powder beds led to higher density objects. Slurry methods were explored to up the densification. However, the porosity of the end product was still sub-optimal.

When the particles are bonded through the binder phase instead of directly, this is refereed to as indirect laser sintering. Full densification requires pyrolization. Binders can be inorganic or organic. Inorganic binders cannot be burned out. Most organic binders are thermoplastics. The laser energy level affects the densification ans structural integrity of the part. Low energy leads to fragility. High energy leads to degradation. SLS parameters heavily effected the densification of green parts. Ultimately, the shortened interaction between the laser and the material leads to poor densification which renders SLS relatively unusable for the purposes of manufacturing usable ceramic parts.

Extrusion free-forming (EFF) refers to the 3D extrusion process. In this manufacturing type, continuous deposition of a ceramic paste or pre-ceramic precursor is applied. The extrudate is wire-like and prone to buckling. The sintering process leads to anisotropic shrinkage. New developments in this ceramic AM type primarily target bio-material applications.

Stereolithography (SLA) is another AM method that can be either indirect or direct. For direct applications, a photo-curing liquid with ceramic fillers is cured. The resultant green body is heat treated. In indirect SLA, a non-filled photo-curing liquid is used as a mold for ceramic casting. These are consolidated are consolidated after the heat treatment process. Some limitations with SLA include discrepancies in the cure track profile an linewidth compensation. Another ceramic AM type is laminate object manufacturing (LOM). This is primarily used to manufacture ceramic tapes.

In one study, Lithography-based Ceramic Manufacturing (LCM) was compared to milled Zirconia blocks under compressive loading [16]. Samples were 3D printed using an LCM

printer where each layer of the suspension was cured with visible blue light. Each sample was post-treated with a cleaning fluid. Then samples were sintered in a thermal post-processing. Control samples were milled and sintered. Uniaxial compression tests were formed on all samples. The milled samples did not fracture, but several of the LCM samples did. The LCM samples were less mechanically reliable than the milled ones in compression. However, the LCM samples showed less deformation under pressure and a preferable modulus of elasticity. Porosity control is critical to mechanical reliability, as porosities result in cracks and brittle fracture. Control of the printer parameters was observed to be of value for controlling unwanted porosity in the LCM printed samples.

In another study, LCM was used to make a heat exchanger [29]. LCM is a form of indirect additive manufacturing, as opposed to direct deposition of the material. Heat exchangers have complex geometries, and demolding them in typical manufacturing processes can be challenging. Additive manufacturing has the potential to overcome these challenges. LCM differs from stereolithography (SLA). With LCM, visible blue light cures a photo-sensitive suspension with dispersed ceramic particles. One limitation of this method is that curing small areas and large ones in the same layer is not feasible with the same process parameters. Additionally, during sintering, deformations were found in thin structures. This study concluded with the importance of design in creating LCM parts.

2.2.2 Ceramics as Coatings

Ceramic coatings are typical applied to a rigid substrate through sintering processes [6]. The sintering process forms a composite at the metal/ceramic interconnects. This composite is considered a film on a rigid substrate and micro-structural changes take place during the sintering process. The in-plane stresses between the film and the substrate lead to the generation of processing defects [5]. These stresses drive a slower densification and propagate flaws. This damage occurs early in the densification process and near pre-existing defects. These defects are generally macroscopic cracks and diffuse damage. This is dependent on

the wavelength of the substrate. The film constraint to the rigid substrate leads to cracking.

Silicon based polymers can be converted into ceramics and used as effective coatings [3]. These coatings modify the surface properties in order to gain strong chemical, thermal and UV resistance. Mist polymer coatings are inexpensive but lack desirable hardness, chemical and thermal properties. Metallic coatings are expensive and prone to corrosion. General ceramic coatings offer high hardness, good wear characteristics and temperature resistance, but are costly and prone to brittle fracture. Alternatively, polymer-derived ceramics (PDCs), can offer these same advantages after undergoing thermal, chemical and radiative processes.

In order for a silicon based polymer to be converted to a ceramic, there must be a latent reactivity. This process is called ceramization. A thermoset polymer can be converted to an amorphous ceramic, or a preceramic into a crystalline ceramic. This is an organic to inorganic transition. There is a risk of residual porosity in the final product, a common flaw in ceramic applications. An amorphous ceramic can be converted into a crystalline ceramic after more processing if needed. This processing is referred to as pyrolysis, and is characterized by processing temperatures of 300C. There is a certain amount of shrinkage in the processing. Therefore, the critical coating thickness for PDCs is generally under 10mm to reduce the risk of cracking.

Adhesion to the substrate is a critical step in the coating process. There a multiple methods for coating different geometries. Dip coating can be used on simple geometries. It is limited to low-viscosity applications and has a high volume of liquid with a low output. Objects that undergo dip coating a subjected to in-homogeneity and edge effects. Spin coating is another option for simple geometries. It has a low volume of liquid relative to the output, but causes a lot of waste. It is only appropriate for low viscosity applications on flat geometries. Spray coating is the best option for complex geometries. It offers more flexibility but generally requires complex parameters.

After application, ceramization takes place. Thermal treatment is the most common curing method. This format is limited to high melt temperature substrates, which makes the treatment inappropriate for many types of polymers with lower melt temperatures. There are alternative methods to pyrolysis, such as UV application, sol-gel and chemical vapor deposition (CVD). PDCs are great environmental barrier coatings. They offer high stability in harsh environments and are anti-corrosive. Additionally they have high hardness, modulus and strength.

2.2.3 Relevant Applications

Most previous work with ceramics for aerospace are for high temperature applications. Ceramic matrix composites (CMCs) were studied for turbine engine components undergoing temperatures above 1000C [20]. These diverging flaps were also subjected to temperature gradients at a rate of 20C/mm over 40mm on the edge of the flap. These thermal gradients led to thermal stress formation. The CMC flaps experienced tensile stress along the edge and consequent compressive stresses at the center. Additionally, the edge defects led to crack propagation during cyclical thermal loading.

Ceramics with melt temperatures above 3200C are referred to a ultra-high temperature (UHT) ceramics [25]. The normal restriction for ceramics outside the UHT group is 1800C. These materials are useful for applications such as crucibles and heat induction units. These UHT ceramics were investigated for use in thermal protective systems as leading edges and nosecones in hyper-sonic re-entry vehicles. The thermal shock resistance was investigated as it is related to mechanical and thermo-physical characteristics (Figure 1). There is a critical thermal shock value where the material undergoes significant changes as a function of the size and geometry as well.

Table III. Mechanical Properties of the Hot-Pressed ZSM and ZHSM Materials: Elastic Moduli E (Resonance Frequency Method) and E_{M0} (Load-Deflection Method), $\Delta E = (E–E_{M0})/E$, Poisson's Ratio ν, Micro-Hardness HV1.0, Fracture Toughness K_{Ic}, and Flexure Strength at Room Temperature σ_{R0}

Sample	$E^{\dagger}$ (GPa)	$E_{M0}{}^{\ddagger}$ (GPa)	ΔE (%)	ν	‡HV1.0 (GPa)	$^{\ddagger}K_{Ic}$ (MPa$\sqrt{m}$)	$^{\ddagger}\sigma_{R0}$ (MPa)
ZSM	480±4	444±5	7.5	0.12	17.7±0.4	4.1±0.05	795±105
ZHSM	508±4	473±9	6.9	0.128	18.2±0.5	4.1±0.75	765±75

†Uncertainity. ‡Mean ± 1 standard deviation.

Table IV. Thermo-Physical Properties and TSR Parameters (R and R') of the Hot-Pressed ZSM and ZHSM Materials: Linear Coefficient of Thermal Expansion α (25°–1300°C), Thermal Conductivity K_{TH}, and Critical Thermal Shock ΔT_C

		K_{TH}(W/m·°C)				TSR parameters			
							$^{\dagger}R'$ (kW/m)		
Sample	α (10^{-6}/°C)	30°C	500°C	1000°C	1200°C	$^{\dagger}R$ (°C)	30°C	500°C	ΔT_C (°C)
ZSM	6.68	62.5	64.5	65.1	65.2	218	13.6	14.0	385
ZHSM	6.74	79.9	83.5	84.2	85.0	196	15.7	16.4	475

†Calculated using σ_{R0} in Eq. (1). TSR, resistance to thermal shock.

Figure 1: Mechanical and Thermo-physical Properties of UHT Ceramics [25]

2.3 Polymers, Composites and Metals

The advantages of suing ceramics in the proposed applications hinge on the material mechanical properties. Ceramics are stiff (high modulus), hard and UV stable. However, they are expensive and hard to manufacture into complex geometries. They also lack toughness and are prone to brittle failure. Ceramics can be heat resistant but can also lack thermal shock resistance. Polymers are relatively inexpensive. There has been a lot of work put into advanced manufacturing techniques, such as 3D printing, that make complex geometries possible. However, polymers tend to lack hardness, UV stability, can have undesirable surface roughness and while their failure mode is generally ductile, they lack stiffness and are prone to deflection at sub-optimal loading conditions. The primary limitations of polymers in general in this proposed application stem from these material property limitations.

The surface hardness of polymers is limited, and dynamic applications with intense loading conditions require a degree of surface hardness to ensure the integrity of connections and resistance to surface abrasion and penetration. Indentation hardness testing is a non-destructive form of material testing that can be used to evaluate how a material responds to stress and wear[8]. Because a single sample can be tested multiple times, hardness testing is an intriguing method for characterizing material integrity. This testing has been used to predict the overall structural integrity of a material by correlating the values to destructive

tensile testing. Increases in hardness testing can predict increases in tensile properties for 3D printed polymers for a number of printing parameters.For example, increased nozzle temperatures were correlated with a decrease in hardness (Shore D durometer per BS EN ISO 868:2003) and was paired with a similar drop in tensile strength. Hardness testing yields useful data about the surface of the material, but can also predict advanced properties of the material, without the destruction of the sample.

Another study correlated the surface hardness of materials with the tensile properties for different variations of print parameters [18]. These 3D printing parameters were build orientation, raster direction/angle and layer thickness. Each sample was subjected to Shore D hardness testing per ASTM D2240. Both the hardness and tensile properties were optimal in an on-edge print orientation. The raster had no effect on the hardness. A lower layer thickness yielded a higher hardness value.

The Charpy impact test is a well known form of impact testing that characterizes the fracture toughness of polymers [15]. The test primarily measures the consumed energy of a cross sectional area of a sample, but can also be used to determine crack initiation energy and crack propagation energy. In one study, Charpy impact testing was determined to be sensitive enough to detect deterioration in photooxidated samples. each sample was irradiated with UV to initiate the process. Then each sample was impact tested to determine the absorbed impact energy. UV irradiation caused the deterioration of samples. In other study, the incorporation of fibers in an epoxy polymer matrix was determined to increase notch toughness compared to pure epoxy samples in a Charpy impact test [14].

Surface roughness needs to be controlled for fluid applications. The surface roughness of 3D printed materials can vary due to defects in the layers of a 3D printed part [7]. generally, a defect in one layer propagates throughout the material to the final finished surface. Additionally, ineffective cooling between layer application can lead to warping that cause layer unevenness that propagates to the finished surface. One study aimed to mitigate these

effects by proving in-situ data on layer inconsistencies with a laser profilometer set-up. The instrument was applied to the extruder rig and took measurements between each layer application step. the slicer software was altered to provide feedback on the current layer mapping, and adjust any unevenness due to under-fill or overfill by compensating on the next layer. This was able to overcome defects in the build and mitigate the effects to the end surface profile.

Profilometry has also been used to determine abrasive properties in wear applications [9].A 3D optical profilometer was used to determine the wear track of a epoxy-multi-walled carbon nanotube (MWCNT) sample. Along with scanning electron microscopy, it was determined that the percentage and type of MWCNTs effected the wear behavior during dry sliding.

A major limitation of polymers in outdoor applications is degradation due to UV exposure. Photo-degeneration happens in polymers after the absorption of UV radiation [15]. As the material is irradiated with UV, the photo-oxidation and subsequent auto-oxidation process is initiated, propagated and ultimately terminated. There is limited diffusion of the process into the bulk of the material relative to the surface, Consequently, most studies are performed on thin film samples.

The effect of heat and artificial weathering on material hardness was studied in relation to polymers used in prosthetic applications [32]. Prosthetic devices are subjected to environmental factors such as UV exposure, moisture and heat. These environmental conditions were simulated for PET, PP, PE, ethylene methacrylate isomer, cellulose acetate polymers. A 307L Type D Durometer was used to test the hardness per ASTM D2240. PET was shown to have the highest harness values after testing, likely due to the amorphous non-crystalline nature of the material. All the materials showed variations in hardness over various time periods due to the UV exposure.

Due to its appealing mechanical properties, solutions to the adhesive limitations of PEEK

were studied. While PEEK is useful for its high chemical resistance, operating temperature, biodegradability and good mechanical properties relative to other polymer groups, it has limited adhesive abilities. Air plasma treatment was applied to the surface of chitosan coated PEEK samples. This was effective in increasing the adhesive properties but sacrificed thermal stability. [33]

Fiber reinforced composites offer intriguing directional mechanical properties [28]. However, there are trade-offs between the print and fiber parameters to obtain a desired end result. Most carbon-fiber reinforced polymers (CFRP) AM research and development has gone into Fused deposition method (FDM) applications. There are two types of fiber printing methods: chopped and continuous.

For continuous fiber applications, the matrix is in a separate spool from the filament. These are combined as they are deposited. Chopped fiber applications use prepreg filament.

There are many factors that affect the printed material end result. These parameters include:

- Layer Thickness
- Infill Density
- Infill Pattern
- Raster Angle
- Raster Width
- Air Gaps
- Building Orientation
- Flow Rate

- Extrusion Temperature
- Deposition Speed
- Number of Perimeter Shells
- Fiber Volume Fraction
- Fiber Orientation

The main commercially available printer available for continuous fiber applications is the Markforged. This gives the user the matrix options of nylon or mixed nylon with chopped fiber. The user can also control the volume fraction and layer selection, In-nozzle impregnation for continuous fiber applications is not commercially available but the research is promising.

CFRP are subject to the intrinsic anisotropy common to composites. When 3D printed, there is additional anisotropy due to the manufacturing method. Therefore, several parameters affect the directional mechanical properties of a printed part. A higher volume fraction has led to increased impact characteristics, strength and stiffness. Alternating layers of fiber/matrix increased the compressive modulus. A flat build orientation led to higher tensile and impact properties. CFRP parts are prone to porosity defects and waviness of fibers due to limitations in the AM process, such as the lack of pre-tension.

Carbon fiber length and orientation have an effect on the mechanical properties [21]. In one study, this was studied with both chopped and continuous fiber. Short fiber samples were created with fiber lengths ranging from 200-500μm at 0-90°orientation were in a phenolic resin matrix. This was compared with continuous fiber samples in a Markforged printer. Tensile testing was performed and the cross-sections were analyzed. Additionally, FEA analysis was performed. They concluded that the FEA simulation matched the experimental data (despite being modeled as isotropic) but the failure location could not be predicted.

Additionally, longer fibers showed the best bending properties. The print path affected the failure location, and the fiber alignment affected the material properties (stronger when oriented in the path of the force applied). Another study focused on sandwiching layers of carbon fiber between layers of ABS plastic [26]. In this application, layers ABS and carbon fiber were printed with a thermal bonding step in between. CFRP are appealing in aircraft applications due to the reduction in weight relative to the directional mechanical properties.

One major advantage of polymers is the ability to produce complex geometries using advanced manufacturing techniques. Additive manufacturing (AM) refers to the layering of materials to form a part as opposed to traditional methods that subtract from a part to create a new one. There are multiple types of 3D-printers, but they generally rely on the same process. A part is created with a CAD package, converted to a mesh file and then a slicer creates the layers for the 3D-printing process [12].

Extrusion printers are primarily used with plastics with a melt point below 300°C, such as PolyLactic Acid (PLA) and acrylonitrile butadiene styrene (ABS). Various other materials, including non-plastics, can be printed with this method a well. The process is generally referred to as Fused Deposition Modelling (FDM). While versatile and easy to use, one of the main disadvantages of FDM is the need for support material on over-hang structures.

Granular printers can be used to print metals, plastics, ceramics and silicons. In this set-up, a powder distribution system is used in conjunction with an energy source. Each layer is formed with sintering. There is a significant risk of heightened porosity in the material when printing with this method. therefore, materials printed in this format are not suitable for applications where good mechanical properties are expected.

Photo-polymer printers, such as stereolithography (SLA) and solid ground curing (SGC) have also been used to create parts. In this process, a resin is cured in specific locations through a light or laser. An additional UV hardening step takes place after the initial printing

Property	Value	Units
Elastic Modulus	2.78E+11	N/m^2
Tensile Strength	482630000	N/m^2
Compressive Strength	2930300000	N/m^2
Fracture Toughness	6.5	MPa m 1/2
Flexural Strength	758	MPa

Table 1: CerCo Material Datasheet [10]

process. These processes are expensive and storing the raw materials for the application is not ideal. Additionally, the resultant mechanical properties are unimpressive.

Wire printing is an additional format of AM that has not been robustly explored. A wire is used to melt one layer onto the next with electron beam free-form fabrication. It is an efficient process, but prohibitively expensive. However, it does not require post-processing.

The use of AM for manufacturing ship propellers was investigated [12]. Several formats of AM were used to compare to a traditionally manufactured bronze propeller. There were discrepancies between the CAD file and the printed propellers primarily on the leading and trailing edges of the parts. The propellers were tested in a cavitation chamber, using the existing hub. There were critical issues identified with the propellers in the cavitation chamber that were primarily attributed to thermal-related defects in the printed blades resultant of the printing process. The 3D scanning process of the propeller was also questioned for it's reliability.

The material properties of various Markforged composites were recorded in Table 2. The Markforged 3D printer is one of the only commercially available options for continuous fiber printing, and has several proprietary composite bases as well (short fiber). For comparison, the current ceramic material properties for the target application are recorded in Table 1.

	Property	Carbon	Carbon FR	Kevlar®	Fiberglass	HSHT FG
Continuous Fiber	Tensile Strength (MPa)	800	760	610	590	600
	Tensile Modulus (GPa)	60	57	27	21	21
	Tensile Strain at Break (%)	1.5	1.6	2.7	3.8	3.9
	Flexural Strength (MPa)	540	540	240	200	420
	Flexural Modulus (GPa)	51	50	26	22	21
	Flexural Strain at Break (%)	1.2	1.6	2.1	1.1	2.2
	Compressive Strength (MPa)	420	300	130	180	216
	Compressive Modulus (GPa)	62	59	25	24	21
	Compressive Strain at Break (%)	0.7	0.5	1.5	—	0.8
	Izod Impact-notched (J/m)	960	810	2000	2600	3100
	Property	Onyx	Onyx FR	Onyx ESD	Nylon	
Composite Base	Tensile Modulus (GPa)	2.4	3	4.2	1.7	
	Tensile Stress at Yield (MPa)	40	41	52	51	
	Tensile Stress at Break (MPa)	37	40	50	36	
	Tensile Strain at Break (%)	25	18	25	150	
	Flexural Strength (MPa)	71	71	83	50	
	Flexural Modulus (GPa)	3	3.6	3.7	1.4	
	Izod Impact - notched (J/m)	330	—	44	110	

Table 2: Markforged Composite Material Datasheet [24]

2.4 Finite Element Analysis

Previous work involving FEA for relevant applications was explored. As no prior work on ceramic propellers was found, FEA on propellers manufactured with alternate materials were explored as well as the failure criteria for brittle materials and FEA on ceramic denture applications.

2.4.1 Failure Criteria

The definition of failure varies for isotropic materials. For ductile materials, failure is generally described as the point of yield [17]. For brittle materials however, this failure is described as the initiation of fracture. The Mohr-Coulomb criterion is typically viewed as a brittle fracture criterion. However, it can actually be expanded to all isotropic materials. The Mohr-Coulomb theory is based on the transformation of a 3D stress state into an equivalent principal stress state. Mohr's circle is represented in Equation 2.4.1.

$$(\sigma_n - \frac{\sigma_1 + \sigma_3}{2})^2 + \tau_n^2 = (\frac{\sigma_1 - \sigma_3}{2})^2 \tag{2.4.1}$$

In this theory, the fracture limit of a brittle material is determined by the stresses acting on the failure plane. For this criteria, failure is determined at the line tangential to the Mohr's circles for tensile and compressive strengths characterized by Equation 2.4.2.

$$\tau_n + \mu\sigma_n = c \tag{2.4.2}$$

2.4.2 Ceramics

One group investigated the use of a ceramic inlay for the use in an all-ceramic fixed partial denture due to bio-compatibility [30]. The ceramic structures are more durable and have the potential for higher longevity, but have limited strength and fracture toughness. For this application, traditional load-to-failure analysis was not relevant to the failure seen in clinical specimens. The Von Mises stress peaked at 209 MPa for the all-ceramic inlay, and the principal stresses peaked at 177 MPa in compression under a 200N load. The fracture strength of the modeled material was between 900-1200 MPA, so the material could withstand an ultimate load of 1150N according to Von Mises theory and 1240N according to Maximum Principal Stress Theory. For an all-ceramic inlay as opposed to the traditional cast-metal option, the stresses were 20% higher. This indicated that incidence of failure would still be higher than a traditional inlay, but not prohibitively so.

2.4.3 Vibration

Quadcopters are a UAV type that is subjected to forces that make them sensible to vibration [1]. The propeller blades, which rotate to provide thrust, are optimal when as rigid and light as possible. However in flight vibration can cause problematic cracking when the natural frequency is reached and resonance occurs. The natural frequencies of optimized propeller geometries were determined using modal analysis. A mesh discretization study was preformed on the first natural frequency. Overall, the first 6 natural frequencies were

determined for 3 propeller designs based on the risk of cracking.

2.4.4 Composite Propellers

Fiber-reinforced polymer members have uses in many applications due to their relatively high stiffness given the weight. They are also easy to process, but the anisotropy of the material creates difficulties in modeling them [22]. In one analysis of a wind turbine blade, FRP beams were modeled using a combination of section analysis and Finite Element Modeling (FEM). With section analysis, sections are characterized by stiffness matrices. When combined with FEM, the approach was able to account for the complex anisotropy of the composite material.

Fiber-based composites have high in-plane strength but are weak in the through-thickness [11]. Due to this, a shell mesh is not appropriate and a 3D mesh must be used instead. This is due to the anisotropy induced by the fiber orientation. The fiber orientation must be properly accounted for and defined in order to accurately represent the material. Defining fiber orientation in a 3D mesh is more challenging for multiple curved bodies, such as airfoils. This was addressed by creating and applying a pre-processor to account for the orientation needs. in another study, a method was developed where the stiffness properties of small composite marine propellers were determined from static experimental data [23].

CHAPTER III

Methodology

3.1 3D Scanning

Propellers were 3D scanned in order to help model the complex geometry. Objects were scanned in the 3D scanner and converted to STL or OBJ files. To understand the accuracy of the scan, the scanner was first validated with known airfoils.

3.1.1 Airfoil

Known airfoils were modeled using export data for a standard Clark Y airfoil [2]. The chord was 100mm at 100% thickness (Figure 2). This curve was exported (Figure 3) and used to create a model in SolidWorks (Figure 4). Then, the model was 3D printed on a Creality CR-10 V3 printer at 80% infill on a raft support. The flat edge of the model was in contact with the bed/raft support so that the airfoil shape was created with each layer and would have the highest print accuracy. After the print, the chord of the airfoil was measured vs the expected value. Three measurements were taken for an average of 98.75mm, which is 1.25% error.

The printed airfoil was then 3D scanned (Figure 5). The 3D scanned file was converted to an STL file and imported into SolidWorks. The scanned file was then sectioned in order to measure the airfoil shape. The airfoil curve sketch was determined and extruded as a separate part. This was placed into an assembly with the modeled reference airfoil. The

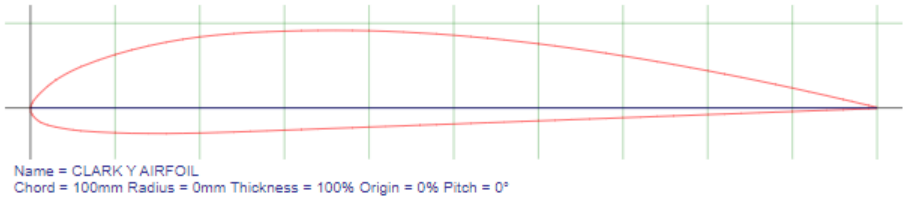

Figure 2: Example Airfoil Plot [2]

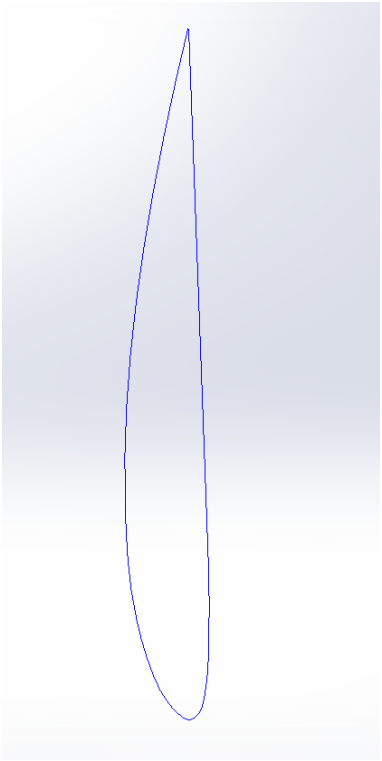

Figure 3: SolidWorks Imported Airfoil Curve

parts were superimposed on each other (Figure 6).

3.1.2 Scanned Propeller

A propeller was provided by Hydronalix and scanned at OSU. The OBJ file was imported into SolidWorks. This file was converted into a format that could be sectioned. Planes were generated from a datum in the file, spanning ever 10mm in a direction where the airfoil cross-section was in the plane. These sections were continued throughout the full length of the blade (Figure 7). The full propeller contained 2 blades, but the scan was of half. Once the blade was sectioned by planes at known intervals, the the mesh intersection points were

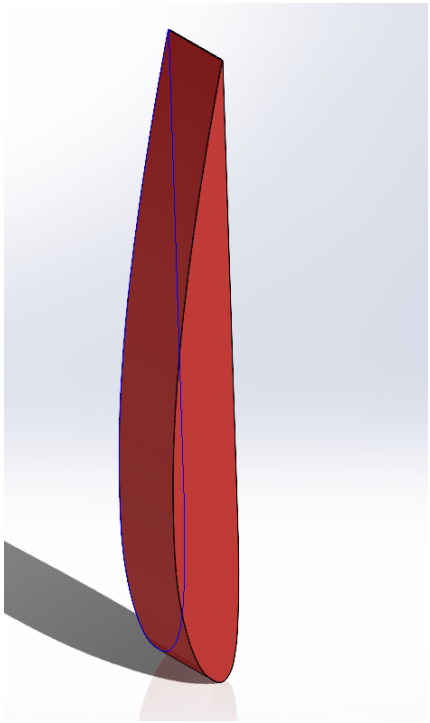

Figure 4: SolidWorks Model-Extruded Airfoil Curve

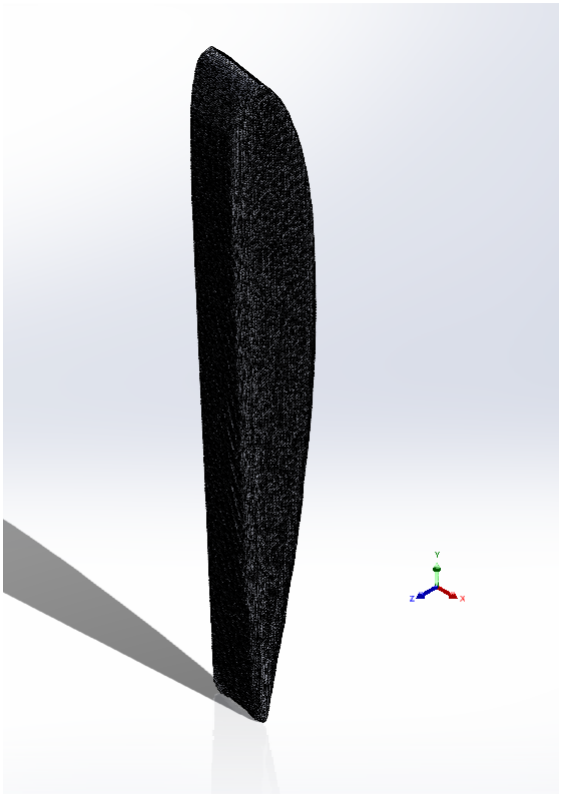

Figure 5: 3D Scan of 3D Printed Extruded Airfoil Curve

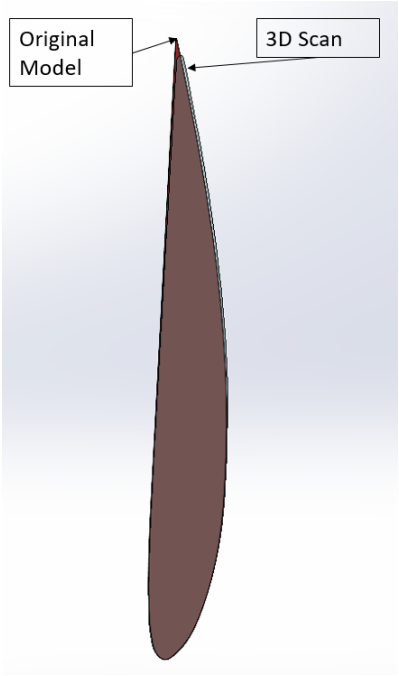

Figure 6: Reference SolidWorks Model Superimposed on 3D Scan of 3D Printed Part (Top-View)

mapped (Figure 8). These were exported into separate files by section for analysis due to limitations given the amount of data in the file. These sections were compared to known airfoils [2] and determined to be Clark Y. Given this assumption, each airfoil section was measured the thickness, chord and pitch. The curve representing the section was extruded and SolidWorks evaluation tools for material thickness were used. The thickness was then used to determine the percentage thickness in order to generate a known Clark Y airfoil for each section. The measured chord length was adjusted based on the error observed in the airfoil scanning validation. the pitch was measured based of the true vertical axis of the 2D element and not the relative axis of the blade, which was not coincident with the expected planes. This required an x and y component calculation and correction for each section. This correction was applied to the exported airfoil data before it was imported as curves into SolidWorks. After each section airfoil data was determined, the curves were imported and converted into sketches. These were closed off using the tangent arc function given that they are imported as open shapes that cannot be extruded or lofted. After these curves were

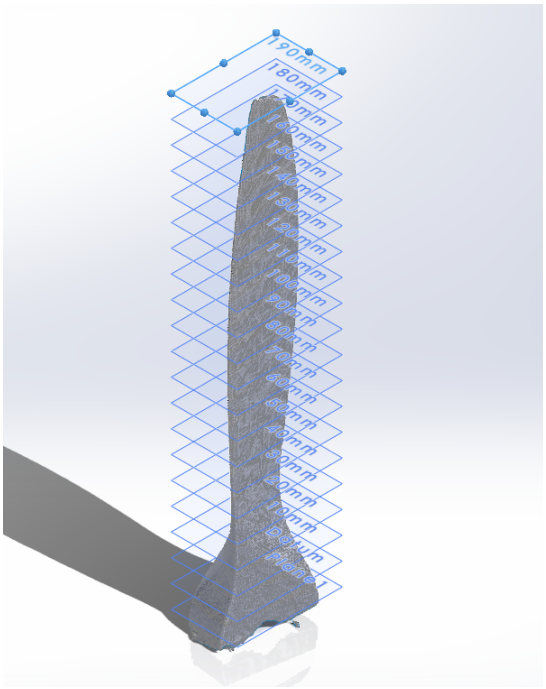

Figure 7: Sectioned 17x10 Scanned Propeller Blade

imported, converted and closed, the features were lofted together to form a twisted blade geometry. The remaining planes that did not form an airfoil shape were lofted into the hub base. The hub was was estimated using the scan data. The full SolidWorks geometry was superimposed onto the original scan data.

3.2 Test Assembly

In order to understand the behavior of ceramic propellers, a test assembly was constructed using commercially available ceramic knives. This was constructed by Hydronalix and the CAD file was sent to OSU for FEA. The hub assembly was constructed with the intent to conduct spin testing, with the knives acting as propeller blades. The knives were positioned at an angle designed to generate some thrust.

3.2.1 Test Assembly CAD Model

In this assembly, a titanium hub holds the commercially available knives at a 10°angle of attack, compressed between two washers by bolts (Figure 9).

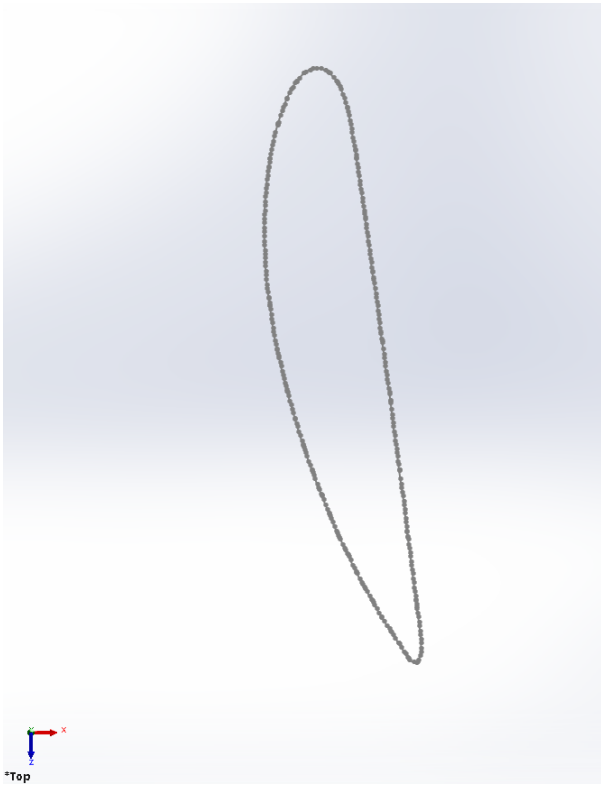

Figure 8: Plane Intersection Plot From Scanned Data

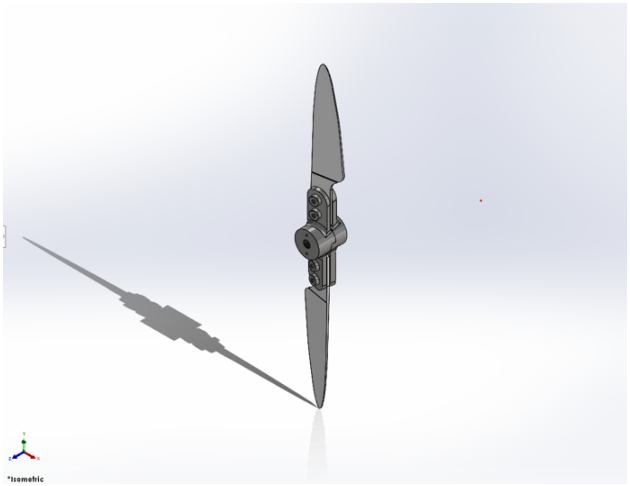

Figure 9: Test Assembly Model-10°Angle of Attack

Property	Value	Units
Elastic Modulus	2.7786e+11	N/m^2
Poisson's Ratio	0.22	
Shear Modulus	1.1376e+11	N/m^2
Mass Density	4480	kg/m^3
Tensile Strength	482630000	N/m^2
Compressive Strength	2930300000	N/m^2
Thermal Expansion Coefficient	850000	/K
Thermal Conductivity	1.4949	W/(m·K)
Specific Heat	877.96	J/(kg·K)

Table 3: Ceramic Knife Property Values

Part	SolidWorks Material
Custom Hub	Commercially Pure CP-Ti UNS R50400(SS)
12mm Low-Profile Socket Head Screw	Alloy Steel
Hub Washer	Alloy Steel
Locknut	Alloy Steel
Nylon-insert to Locknut	Nylon

Table 4: Standard SolidWorks Materials by Part

3.2.2 Test Assembly Failure Analysis

The expected forces on the test assembly were simulated using SolidWorks Simulation in static loading. Five studies were completed in total. The loading situation simulated the forces exerted on the test assembly due to thrust, torque and centrifugal loading. Additionally, the compression on the knives between the washers was simulated. For each test type, FEA was performed until the ceramic knives failed using Mohr Coulomb failure criteria for brittle materials. Custom material properties were entered for the ceramic knives based on the values for Zirmonite in [10]. These are listed in Table 3. The other materials in the assembly were represented by SolidWorks standard property values listed in Table 4. Each study was run with the finest mesh allowed in SolidWorks as there were no computational limitations with doing so.

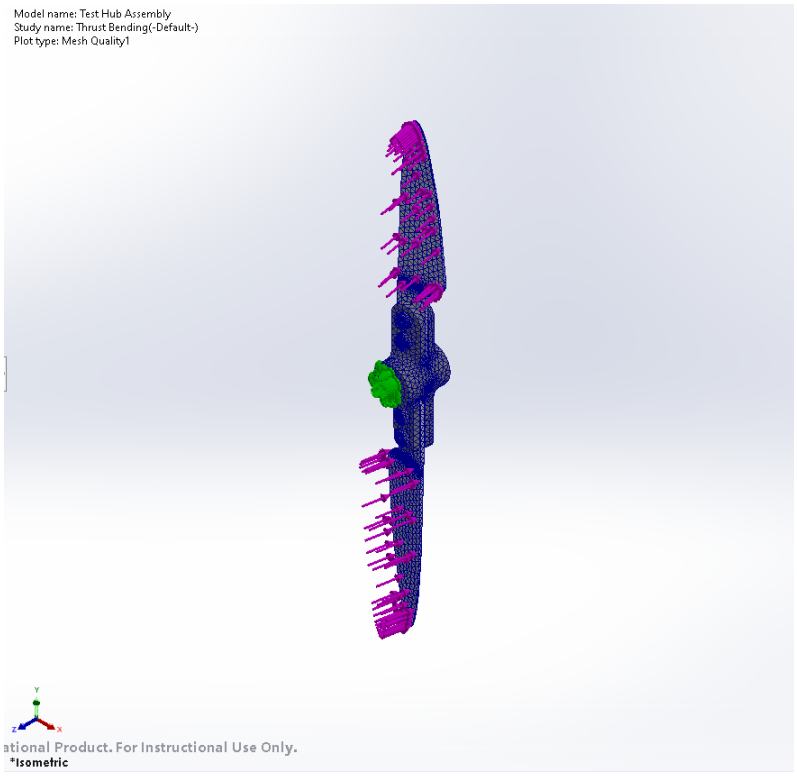

Figure 10: Test Assembly-Thrust Bending Forces

Thrust Bending Forces

The bending forces exerted on the propeller via thrust were simulated as seen in Figure 10. This models the tendency of the propeller to bend in thrust, pushing the blade tips away from the fixation point of the assembly. In this mesh, the test assembly is fixed on the face that would be connected to the greater motor assembly. The force is exerted away from this point to model the direction of the thrust bending forces if the assembly was spun counter-clockwise from the direction of the fixed geometry. The resultant force magnitude is an input in SolidWorks, and the resultant location of that magnitude is determined by SolidWorks assuming a normal distribution on the surface the force is applied to. For this assembly, the force is applied to the ceramic knives in the direction normal to the plane of rotation. The thrust bending study was iterated to failure according to Mohr Coulomb criteria using this set-up.

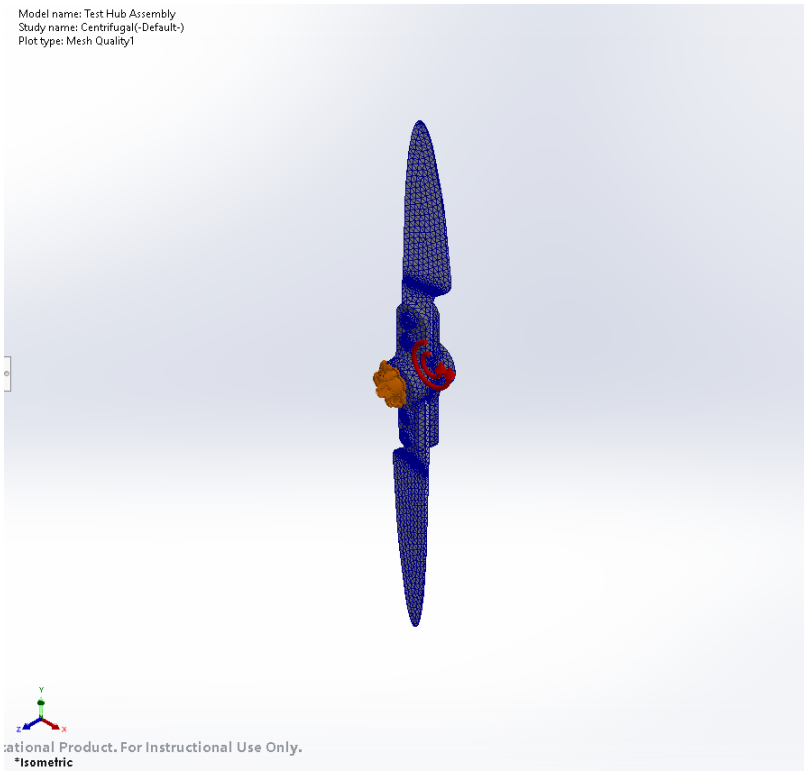

Figure 11: Test Assembly-Centrifugal Loading

Centrifugal Loading

Centrifugal loading was modeled, with the direction of rotation indicated, as shown in Figure 11. This models the forces exerted on the propeller due to spinning. In this mesh, the test assembly is fixed on the face that would be connected to the greater motor assembly. The forces are modeled as if the assembly was spun counter-clockwise from the direction of the fixed geometry. The rotational speed is input into SolidWorks for the centrifugal force, as well as the rotational direction-which determines the magnitude. The centrifugal loading study was iterated to failure according to Mohr Coulomb criteria using this set-up.

Torque Bending Forces

Bending forces due to torque were modeled as shown in Figure 12. This models the bending forces due to torque exerted on the propeller while spinning. In this mesh, the test assembly is fixed on the face that would be connected to the greater motor assembly. The forces

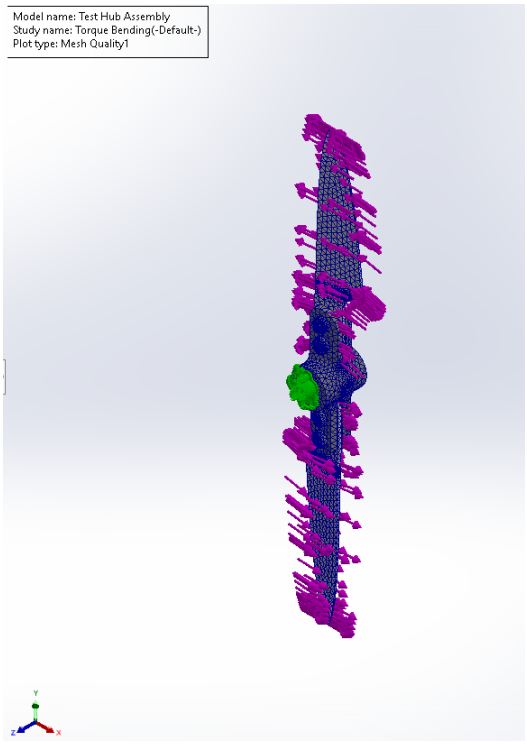

Figure 12: Test Assembly-Torque Bending Forces

are modeled as if the assembly was spun counter-clockwise from the direction of the fixed geometry. The resultant torque magnitude is an input in SolidWorks, and the resultant location of that magnitude is determined by SolidWorks assuming a normal distribution on the surface the torque is applied to. For this assembly, the force is applied to the ceramic knives in the direction of the plane of rotation. The torque bending study was iterated to failure according to Mohr Coulomb criteria using this set-up.

Knife Compression

The test Assembly set-up is built with the assumption that the ceramic knives are affixed firmly in place between the hub washers with no slipping. In order for this to be true, the ceramic knives must be bolted down firmly. Therefore, the maximum compression between the washers in contact with the knife were modeled as shown in Figure 13. The knife compression study was iterated to failure according to Mohr Coulomb criteria using this set-up, at increments of 1kN, starting arbitrarily at 17kN.

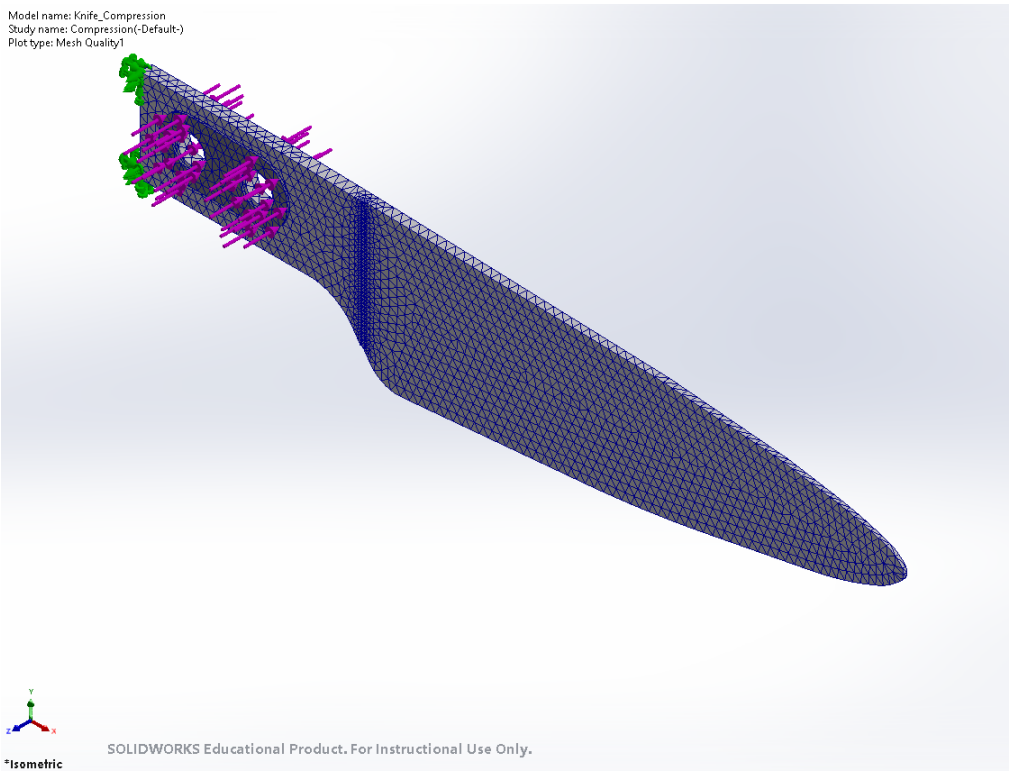

Figure 13: Test Assembly-Knife Compression

3.3 Failure Analysis By Propeller Blade Geometry

Failure analysis was carried out on multiple blade geometry types. An aspect of each blade type was varied specifically, and each type of force was iterated to failure with the intent to see how the variations to the geometry affected the failure modes.

3.3.1 Propeller Blade Variations

The first blade type, twisted blade with airfoil, was modeled based on a known propeller type and 3D scanned data. Then, each other blade type was made based on variations to this geometry.

Twisted Blade with Airfoil

This blade in Figure 14 was modeled using the 3D scan data of a known propeller (see previous sections).

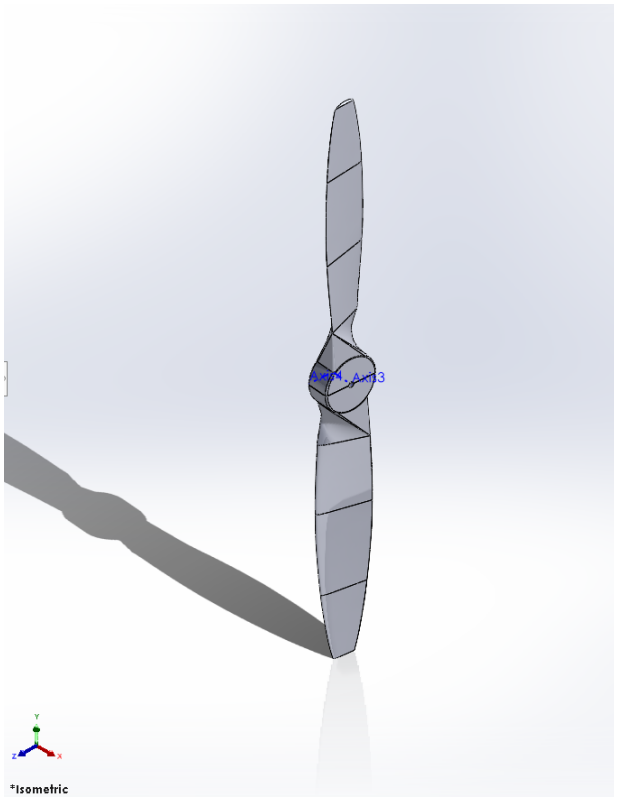

Figure 14: Twisted Blade with Airfoil Model

Thin Blade

The thin blade geometry was created using the same hub and dimensions as the known blade, but with a rectangular cross-section, no chord variations and a 10°angle of attack (Figure15).

Simple Airfoil Blade

The simple airfoil blade was created using the same hub and dimensions as the known blade, with the same airfoil (Clark Y). The airfoil dimensions used were that of the 60mm plane cross section of the scan data on the known propeller and carried throughout the radial length with no chord variations. A 10°angle of attack was used (Figure 16).

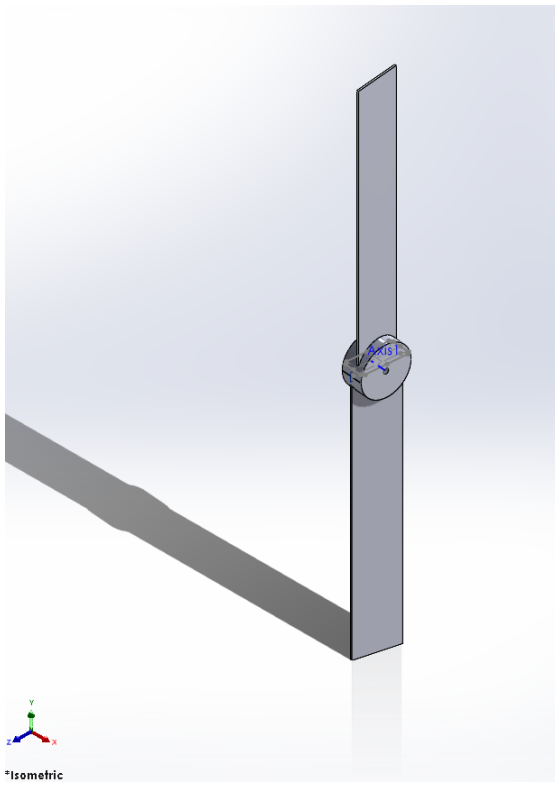

Figure 15: Thin Blade Model

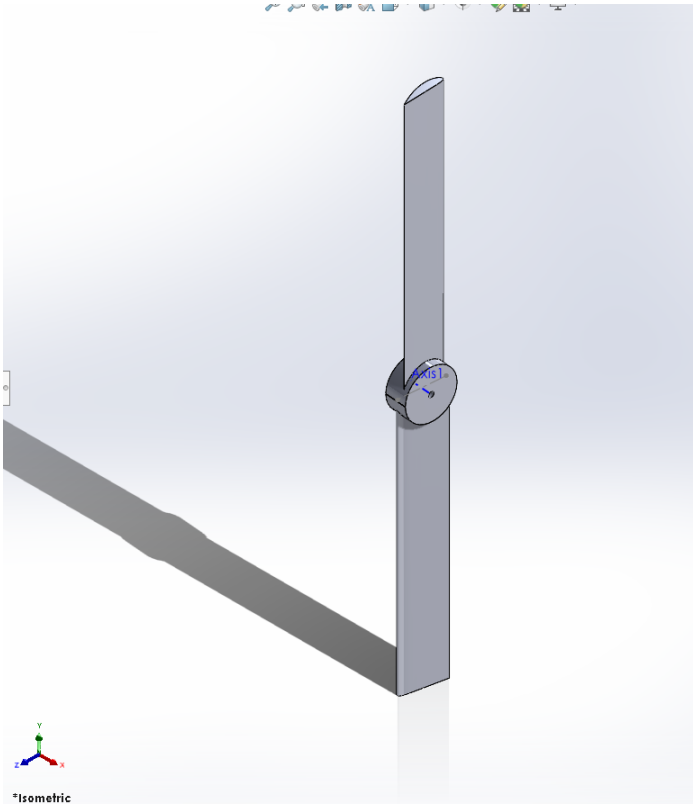

Figure 16: Simple Airfoil Blade Model

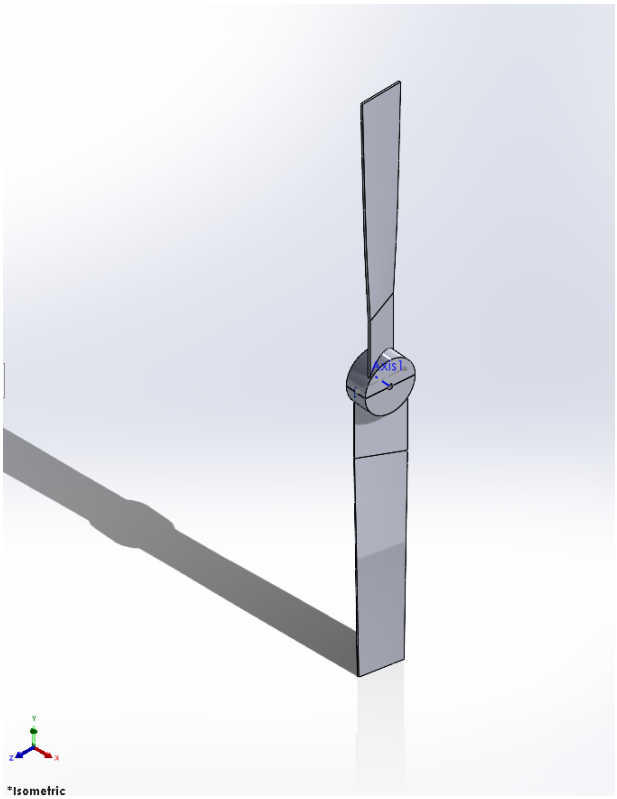

Figure 17: Twisted Thin Blade Model

Twisted Thin Blade

The twisted thin blade geometry was created using the same hub and dimensions as the known blade, but with a rectangular cross-section. The pitch was varied to match the section data of the known scanned propeller (Figure 17).

3.3.2 Thrust Bending Forces

The thrust bending study models the tendency of the propeller to bend in thrust, pushing the blade tips away from the fixation point of the assembly as seen in Figures 18, 20, 19 and 21. In this mesh, the test assembly is fixed on the face that would be connected to the greater motor assembly. The force is exerted away from this point to model the direction of the thrust bending forces if the assembly was spun counter-clockwise from the direction of the fixed geometry. The resultant force magnitude is an input in SolidWorks, and the resultant location of that magnitude is determined by SolidWorks assuming a normal distribution on

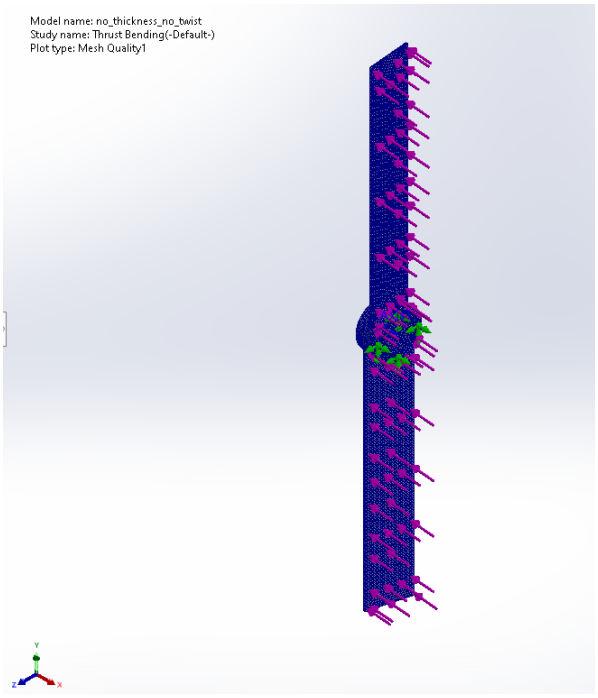

Figure 18: Thin Blade Thrust Bending Mesh

the surface the force is applied to. For these geometries, the force is applied to the blades in the direction normal to the plane of rotation. The thrust bending study was iterated to failure according to Mohr Coulomb criteria using this set-up.

3.3.3 Centrifugal Loading

Centrifugal loading was modeled, with the direction of rotation indicated, as shown in Figure 22, 23, 24 and 25. This models the forces exerted on the propeller due to spinning. In this mesh, the test assembly is fixed on the face that would be connected to the greater motor assembly. The forces are modeled as if the assembly was spun counter-clockwise from the direction of the fixed geometry. The rotational speed is input into SolidWorks for the centrifugal force, as well as the rotational direction-which determines the magnitude. The centrifugal loading study was iterated to failure according to Mohr Coulomb criteria using this set-up.

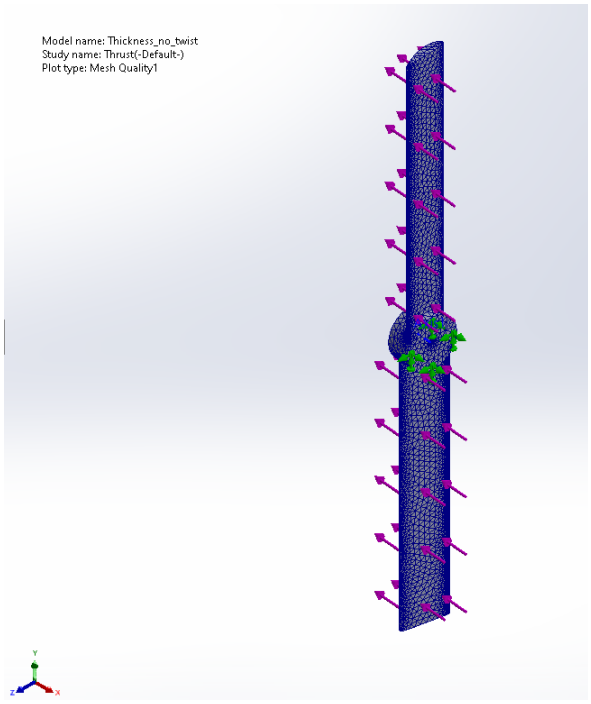

Figure 19: Simple Airfoil Thrust Bending Mesh

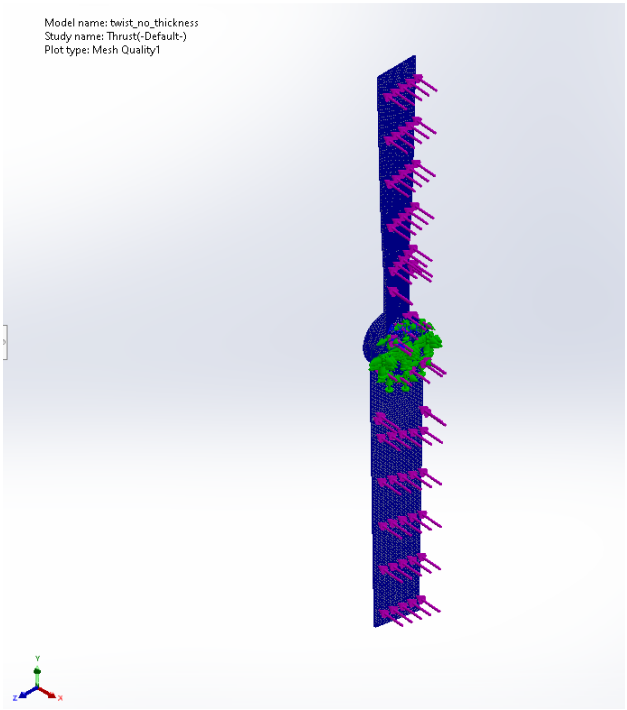

Figure 20: Twisted Thin Blade Thrust Bending Mesh

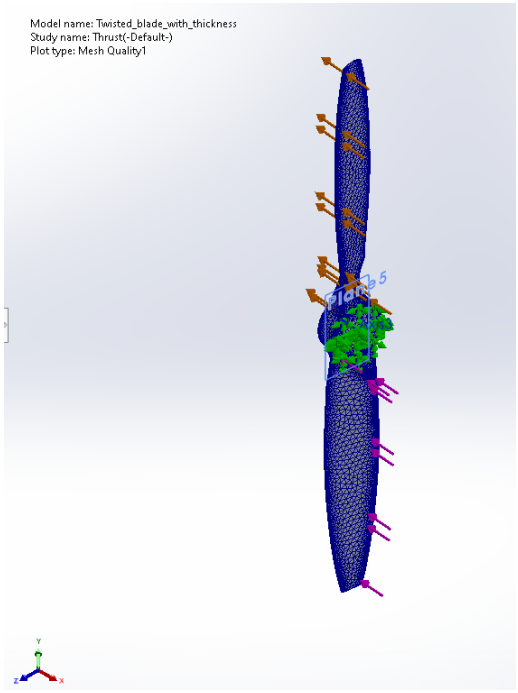

Figure 21: Twisted Blade with Airfoil Thrust Bending Mesh

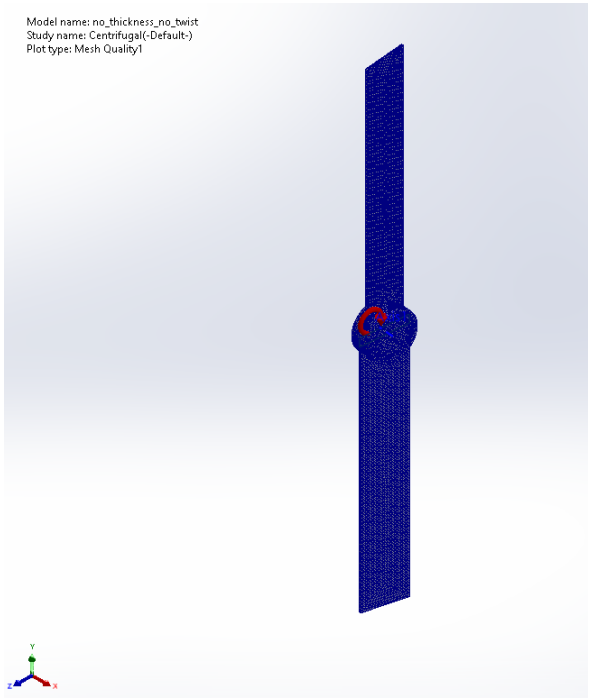

Figure 22: Thin Blade Centrifugal Loading Mesh

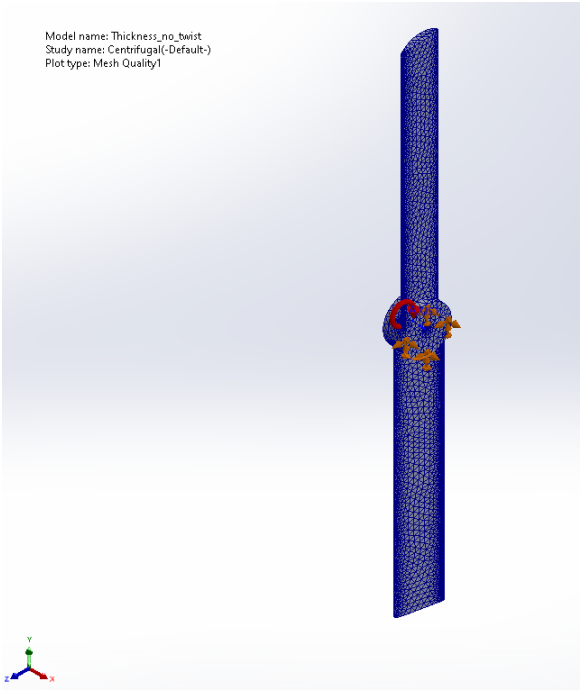

Figure 23: Simple Airfoil Centrifugal Loading Mesh

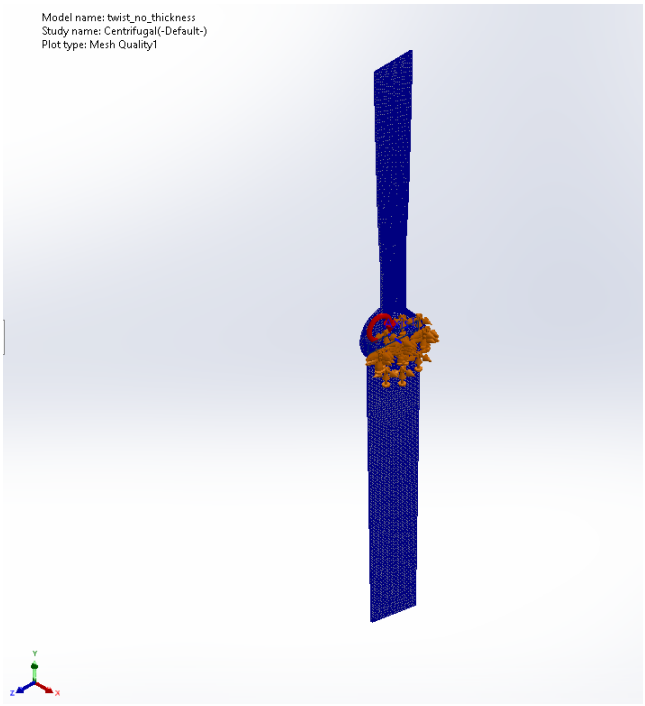

Figure 24: Twisted Thin Blade Centrifugal Loading Mesh

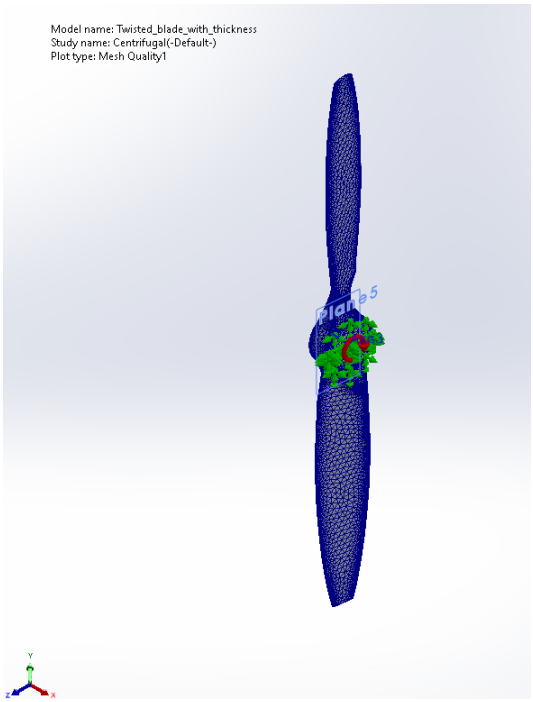

Figure 25: Twisted Blade with Airfoil Centrifugal Loading Mesh

3.3.4 Torque Bending Forces

Bending forces due to torque were modeled as shown in Figure 26, 27, 28 and 29. This models the bending forces due to torque exerted on the propeller while spinning. In this mesh, the test assembly is fixed on the face that would be connected to the greater motor assembly. The forces are modeled as if the assembly was spun counter-clockwise from the direction of the fixed geometry. The resultant torque magnitude is an input in SolidWorks, and the resultant location of that magnitude is determined by SolidWorks assuming a normal distribution on the surface the torque is applied to. For these geometries, the force is applied to the blades in the direction of the plane of rotation. The torque bending study was iterated to failure according to Mohr Coulomb criteria using this set-up.

3.4 Propeller Blade with Expected Forces

In the failure analysis, specific loading situations were applied to all propeller types separately. This section aims to understand all the forces acting on the propeller simultaneously.

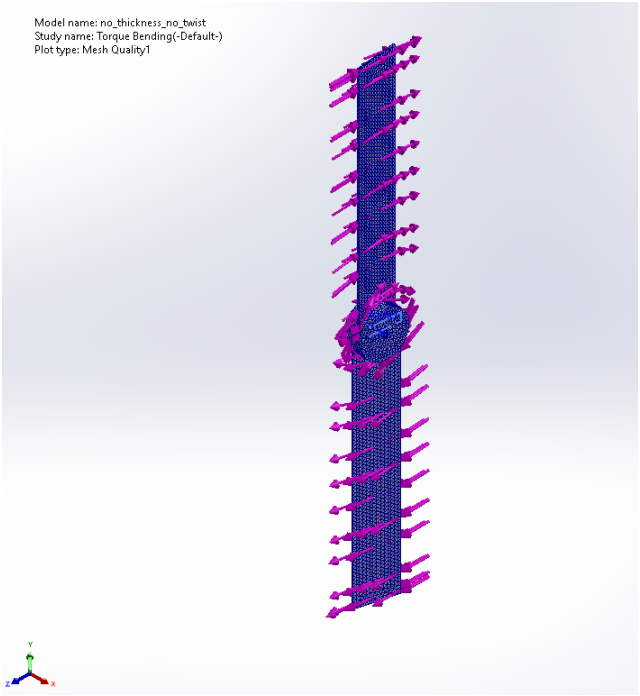

Figure 26: Thin Blade Torque Bending Mesh

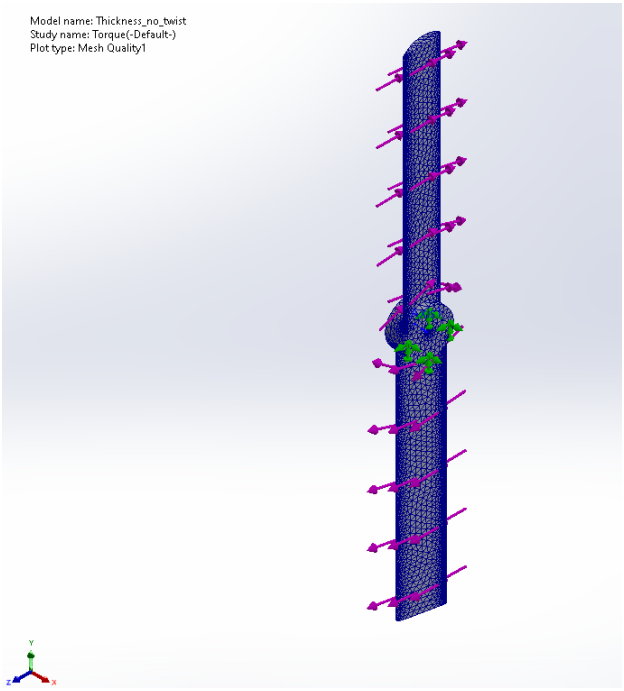

Figure 27: Simple Airfoil Torque Bending Mesh

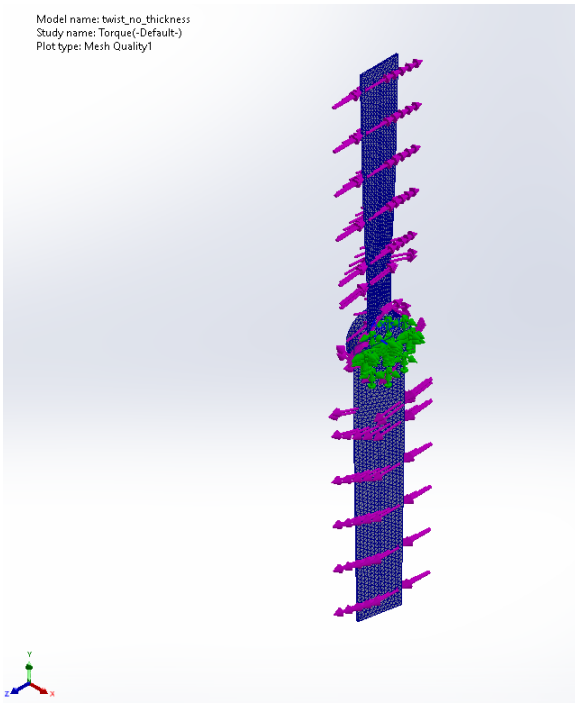

Figure 28: Twisted Thin Blade Torque Bending Mesh

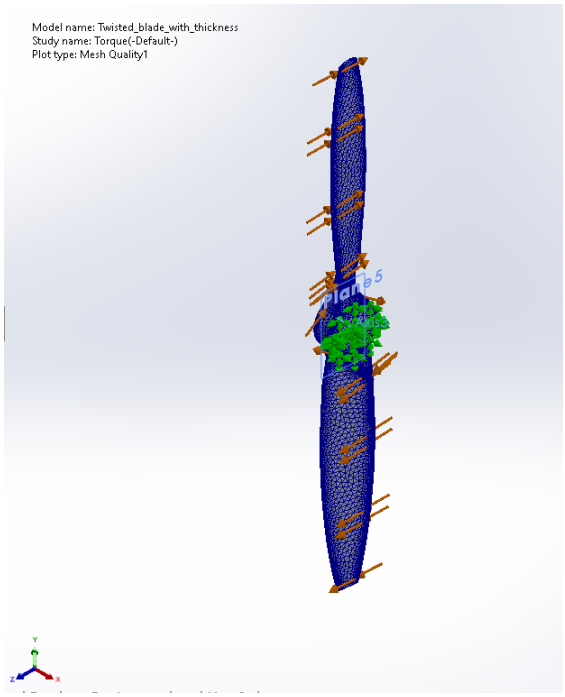

Figure 29: Twisted Blade with Airfoil Torque Bending Mesh

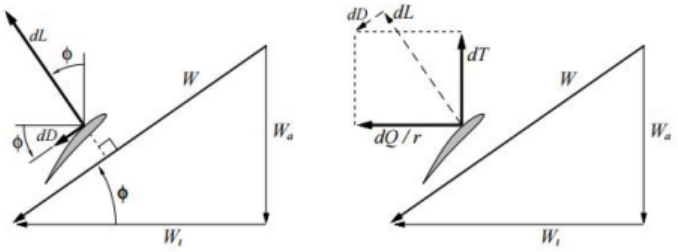

Figure 30: Thrust(T) and Torque(Q) Components of Lift(L) and Drag(D) [19]

3.4.1 Matlab code

Coefficient of lift (CL) and coefficient of drag (CD) distributions based on relative radial lengths were provided using CROTOR, a numerical code for propeller blade analysis. Using these exports, the angle of attack β, the relative dimensions related to the known radius (c/R and r/R), CL and CD arrays were imported. The c/R and r/R were converted to known dimensions using the radius. Then, the lift (L) and drag (D) were determined using equation 3.4.1 and equation 3.4.2.

$$L = \frac{\rho(\frac{\omega}{r})^2 cCL}{2} \tag{3.4.1}$$

$$D = \frac{\rho(\frac{\omega}{r})^2 cCD}{2} \tag{3.4.2}$$

With the lift and drag components defined, these could be converted to Thrust (T) and Torque (Q) components based on the angle of attack (Figure 30), β using equation 3.4.4 and equation 3.4.3.

$$T = L\cos\beta - D\cos\beta \tag{3.4.3}$$

$$Q = L \sin \beta - D \sin \beta r \tag{3.4.4}$$

The resulting arrays were then curve fit to a 3rd degree polynomial based on radial length. Then the magnitude of the resultant thrust and torque and location were determined by integrating the curve fit equations.

3.4.2 Combined Loading Studies

With the resultant thrust and torque determined, the blade geometries and test assembly were studied under combined loading. All tests were generated at 12,000 RPM. Centrifugal loading was represented at this speed. The thrust was calculated assuming this speed as well, and the resultant was applied to each blade using the nonuniform loading section in SolidWorks. The torque was also applied, but the resultant location was not accounted for in SolidWorks.

Test Assembly

The forces due to thrust, torque and centrifugal loading were simulated using the model in Figure 31.

Twisted Blade with Airfoil

The forces due to thrust, torque and centrifugal loading were simulated using the model in Figure 35.

Thin Blade

The forces due to thrust, torque and centrifugal loading were simulated using the model in Figure 33.

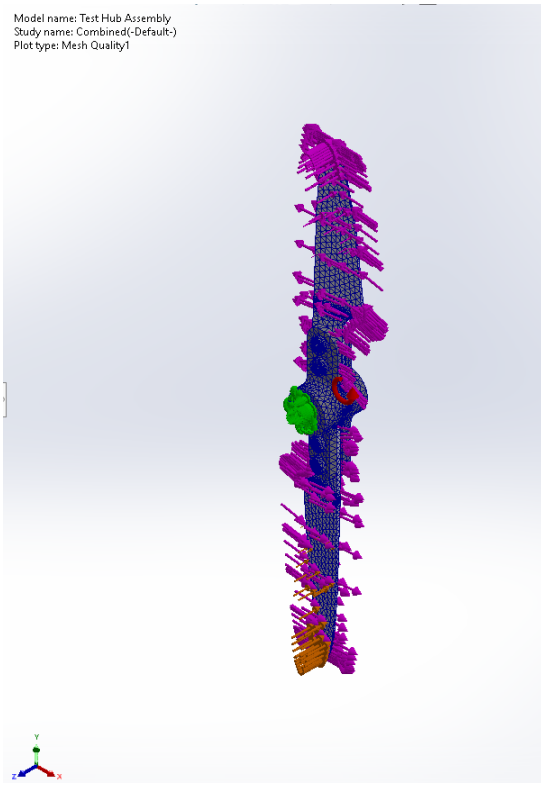

Figure 31: Test Assembly Combined Loading Mesh

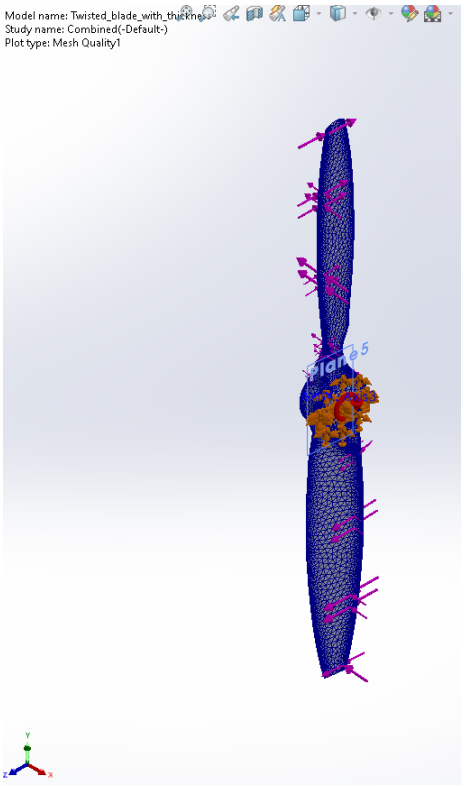

Figure 32: Twisted Blade with Airfoil Combined Loading Mesh

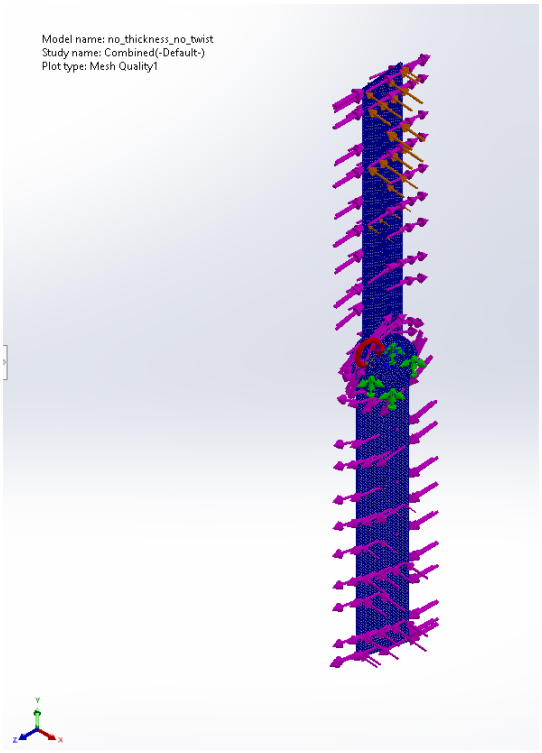

Figure 33: Thin Blade Combined Loading Mesh

Simple Airfoil Blade

The forces due to thrust, torque and centrifugal loading were simulated using the model in Figure 34.

Twisted Thin Blade

The forces due to thrust, torque and centrifugal loading were simulated using the model in Figure 35.

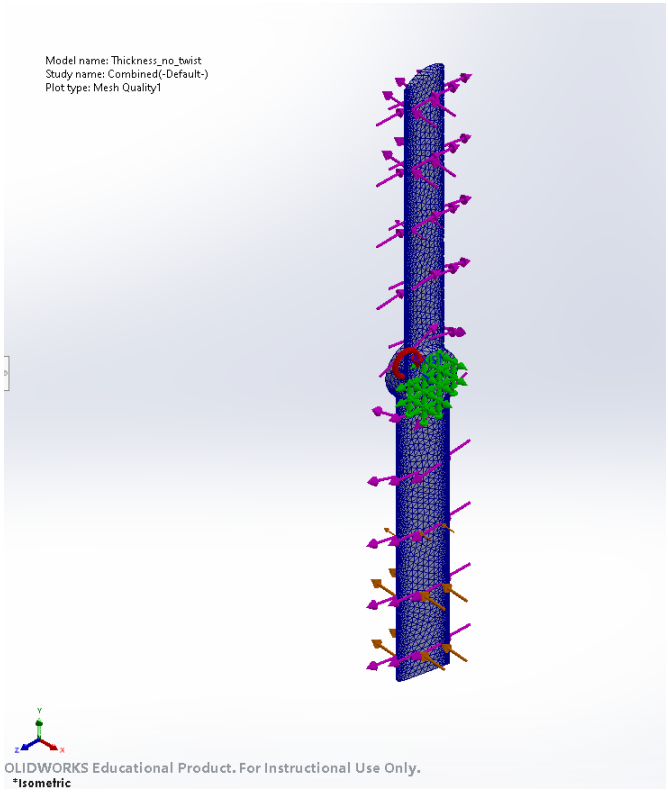

Figure 34: Simple Airfoil Blade Combined Loading Mesh

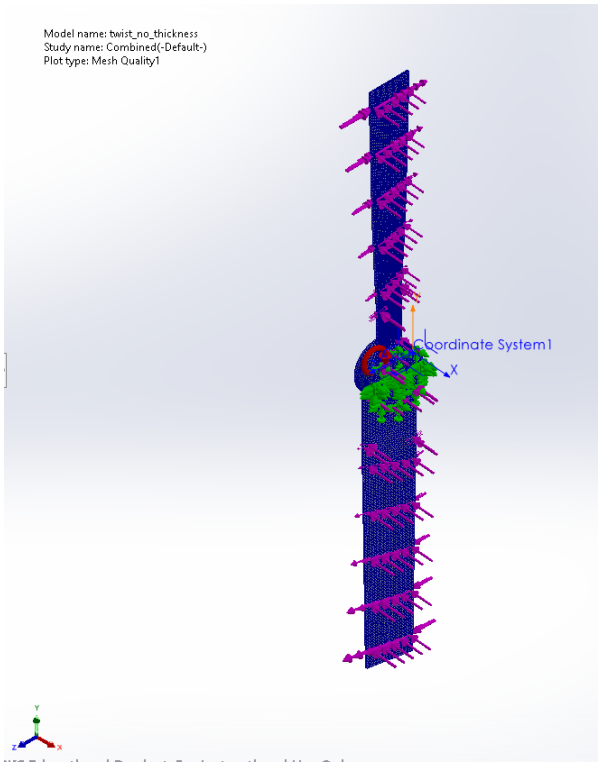

Figure 35: Twisted Thin Blade Combined Loading Mesh

CHAPTER IV

Results

4.1 3D Scanning Airfoil Validation Results

In the superimposed model, the leading edges matched well (Figure 36). Closer to the mid-chord, some differences can be seen (Figure 37). At the trailing edge, the main differences can be spotted (Figure 39 and 38). The difference between these was measured in SolidWorks to be 2.77mm in the direction of the chord length. The error in the 3D print was 1.25mm, meaning that 1.52mm of the difference can be attributed solely to the error of the scan. The difference in area was also determined to be 0.39% (Figure 40 and 41).

4.2 Scanned Propeller Results

The measurements of each section of the scanned propeller were captured in Table 5.

Section Plane	Thickness (mm)	Thickness (%)	Chord measured	Chord Adjusted	Pitch Measured	Pitch adjusted	Y component	Y Correction	X component	X correction
40mm	217.75	217.75	32.08	33.60	19.99	70.01	31.58	3.21	11.49	-5.74
50mm	185.33	185.33	32.93	34.45	18.54	71.46	32.66	2.67	10.95	-5.48
60mm	166.36	166.36	34.29	35.81	16.77	73.23	34.29	1.86	10.33	-5.17
70mm	156.94	156.94	35.24	36.76	14.96	75.04	35.51	1.24	9.49	-4.74
80mm	151.38	151.38	36.14	37.66	13.33	76.67	36.65	0.68	8.68	-4.34
90mm	148.64	148.64	36.43	37.95	11.96	78.04	37.13	0.44	7.86	-3.93
100mm	147.01	147.01	36.56	38.08	10.34	79.66	37.46	0.27	6.83	-3.42
110mm	144.71	144.71	36.34	37.86	9.56	80.44	37.33	0.33	6.29	-3.14
120mm	143.12	143.12	35.44	36.96	8.43	81.57	36.56	0.72	5.42	-2.71
130mm	140.04	140.04	34.35	35.87	7.45	82.55	35.57	1.22	4.65	-2.33
140mm	138.61	138.61	32.95	34.47	6.35	83.65	34.26	1.87	3.81	-1.91
150mm	138.35	138.35	31.16	32.68	5.48	84.52	32.53	2.73	3.12	-1.56
160mm	138.54	138.54	29.08	30.60	4.64	85.36	30.50	3.75	2.48	-1.24
170mm	138.12	138.12	26.45	27.97	3.39	86.61	27.92	5.04	1.65	-0.83
180mm	139.27	139.27	23.09	24.61	2.83	87.17	24.58	6.71	1.22	-0.61
190mm	143.41	143.41	19.34	20.86	1.91	88.09	20.85	8.58	0.70	-0.35
200mm	143.35	143.35	14.28	15.80	0.83	89.17	15.80	11.10	0.23	-0.11

Table 5: Scanned Propeller-Section Data

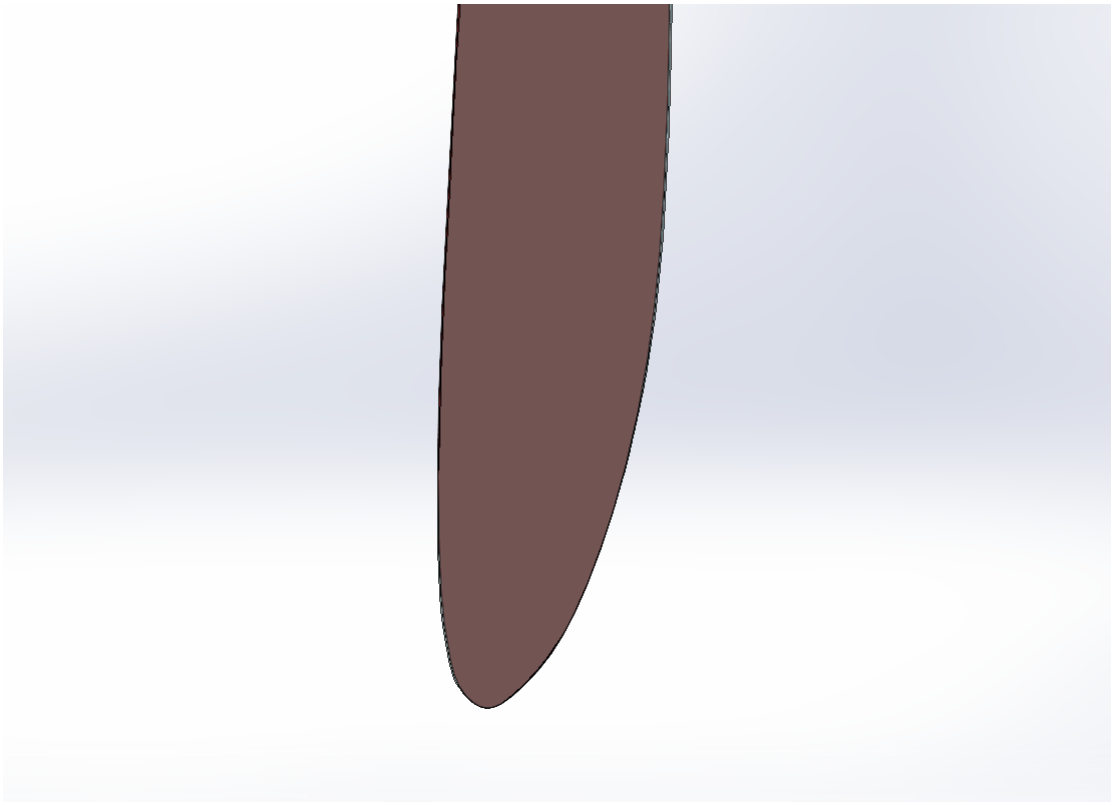

Figure 36: Reference Airfoil Superimposed on 3D Scan (Leading Edge)

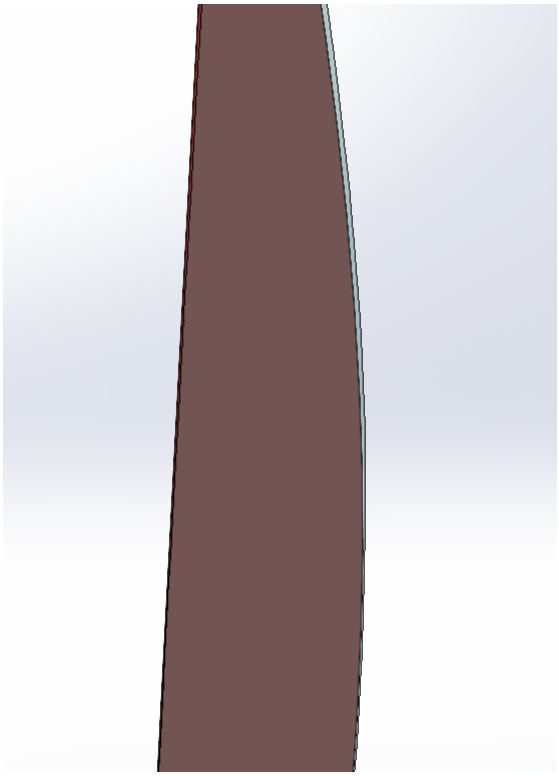

Figure 37: Reference Airfoil Superimposed on 3D Scan (Mid-chord)

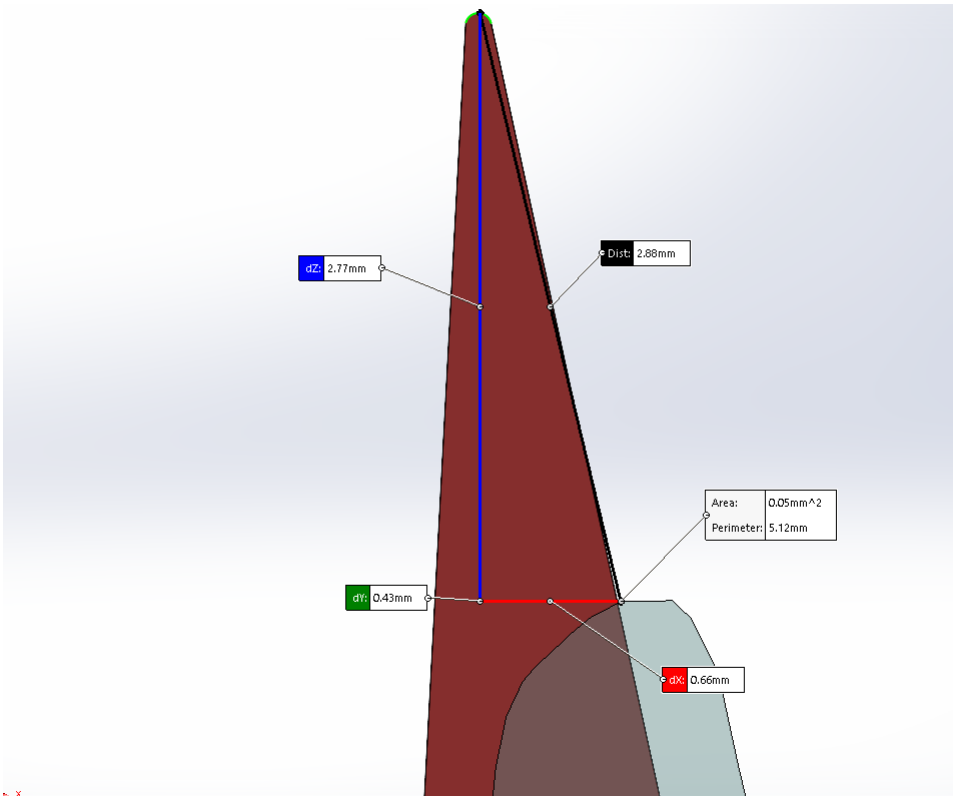

Figure 38: Reference Airfoil Superimposed on 3D Scan (Trailing Edge-Top)

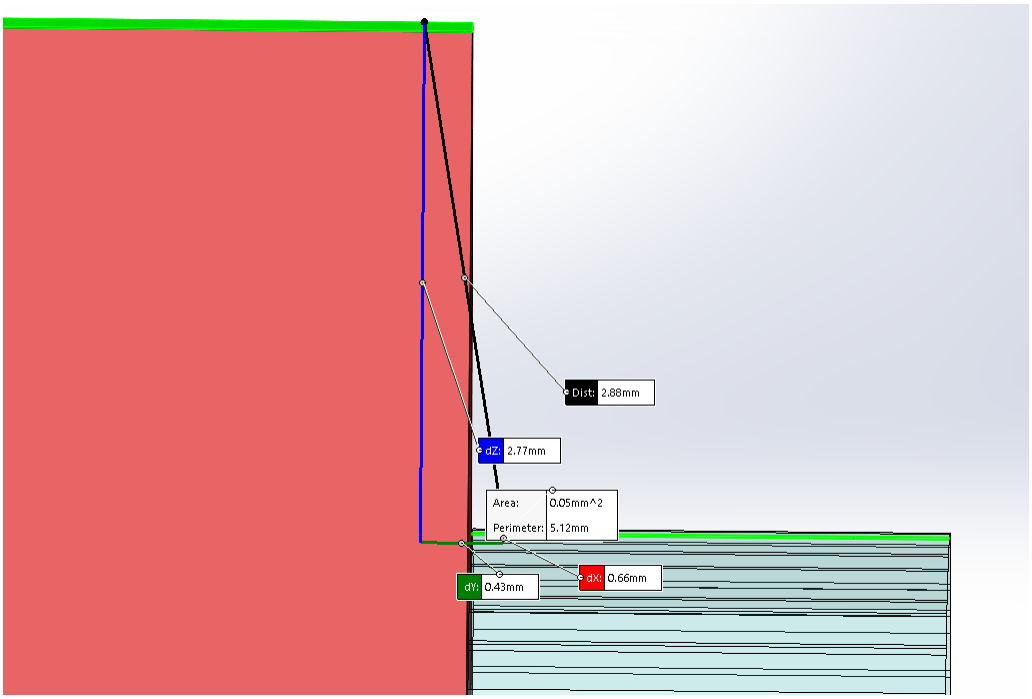

Figure 39: Reference Airfoil Superimposed on 3D Scan (Trailing Edge-Side)

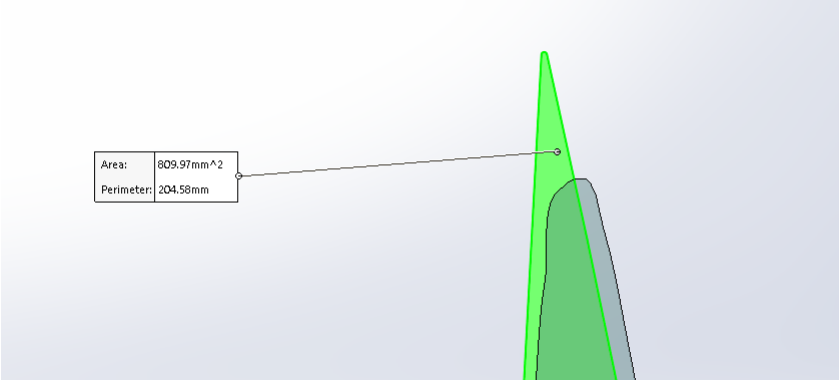

Figure 40: Reference Airfoil Area

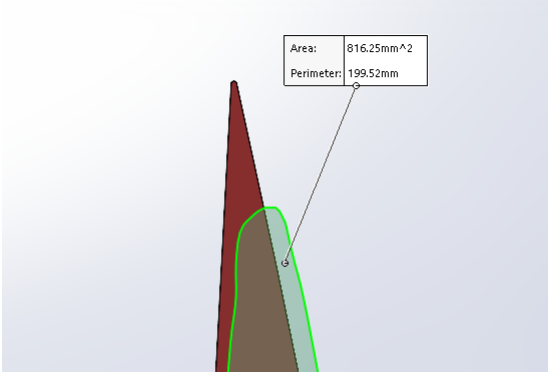

Figure 41: 3D Scanned Airfoil Area

Analysis	Force Applied	FOS-Mohr Coulomb	Max Displacement (mm)
2	10N	6.8	0.7483
4	20N	3.4	1.498
6	30N	2.3	2.247
10	40N	1.7	2.994
12	50N	1.4	3.74
14	60N	1.1	4.485
15	70N	0.96	5.23

Table 6: Test Assembly Thrust Bending Study Results

4.3 Test Assembly Failure Analysis Results

Finite Element Analysis was performed on the test assembly to understand the response to various loading conditions typically experienced during spinning of a propeller. Each study was iterated until failure. Additionally, the maximum allowable compression force exerted on the ceramic knife by the washers was determined as well.

4.3.1 Thrust Bending Study

The thrust bending simulation was iterated until failure according to Mohr Coulomb criteria for brittle materials. The maximum deflection and minimum Factor of Safety (FOS) was determined for each simulation and recorded in table 6. Failure was categorized as the applied force at which the Mohr Coulomb FOS was 1. For thrust bending, this occurred at 65N applied force (44). The maximum deflection due to thrust bending was 4.936mm at 65N (Figure 42 and 43). The stress and strain were also captured for this loading situation 45 and 46).

4.3.2 Centrifugal Loading study

The centrifugal loading simulation was iterated until failure according to Mohr Coulomb criteria for brittle materials. The maximum deflection and minimum Factor of Safety (FOS) was determined for each simulation and recorded in table 7. Failure was categorized as the applied force at which the Mohr Coulomb FOS was 1. For centrifugal loading, this occurred

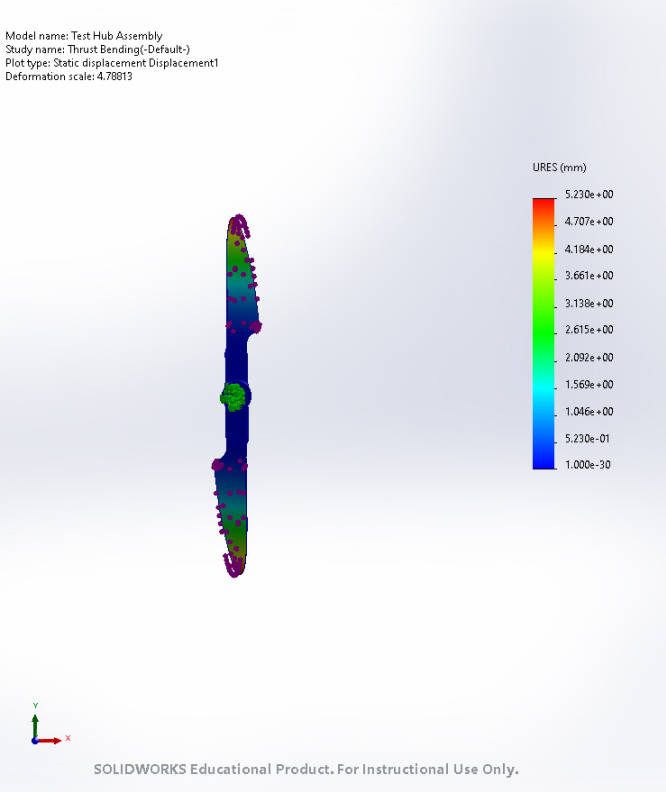

Figure 42: Test Assembly Displacement due to Thrust Bending at 70N (Front)

between 19,000 and 20,000 RPM (49). The maximum deflection due to centrifugal loading was 0.2609mm at 19,000 (Figure 47 and 48). The stress and strain were also captured for this loading situation at 19,000 RPM (Figures 50 and 51).

4.3.3 Torque Bending Study

The torque bending simulation was iterated until failure according to Mohr Coulomb criteria for brittle materials. The maximum deflection and minimum Factor of Safety (FOS) was determined for each simulation and recorded in table 8. Failure was categorized as the applied force at which the Mohr Coulomb FOS was 1. For torque bending, this occurred between 19,000 and 20,000 RPM (54). The maximum deflection due to torque bending was 0.2609mm at 19,000 (Figure 52 and 53). The stress and strain were also captured for this loading situation at 19,000 RPM 55 and 56).

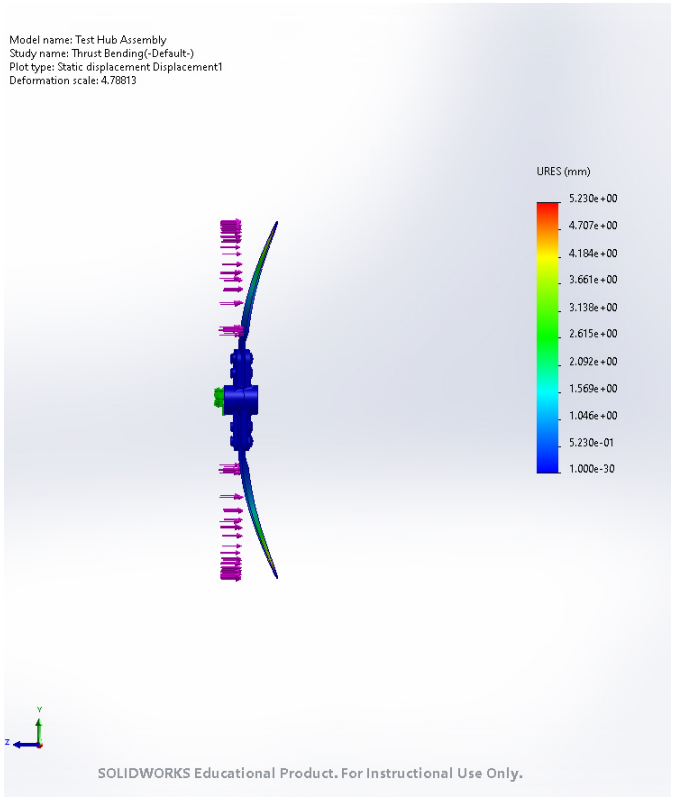

Figure 43: Test Assembly Displacement due to Thrust Bending at 70N (Right)

Analysis	Rad/s	RPM	FOS-Mohr Coulomb	Max Displacement
1	942	9,000	4.4	0.1015mm
2	1047	10,000	3.5	0.1184mm
3	1152	11,000	3	0.1379mm
4	1256	12,000	2.5	0.1544mm
5	1361	13,000	2.1	0.1706mm
6	1466	14,000	1.9	0.1862mm
7	1570	15,000	1.6	0.2011mm
8	1657	16,000	1.5	0.2132mm
9	1780	17,000	1.3	0.297mm
10	1884	18,000	1.1	0.2431mm
11	1989	19,000	1.1	0.2609mm
12	2094	20,000	0.95	0.2742mm

Table 7: Test Assembly Centrifugal Loading Results

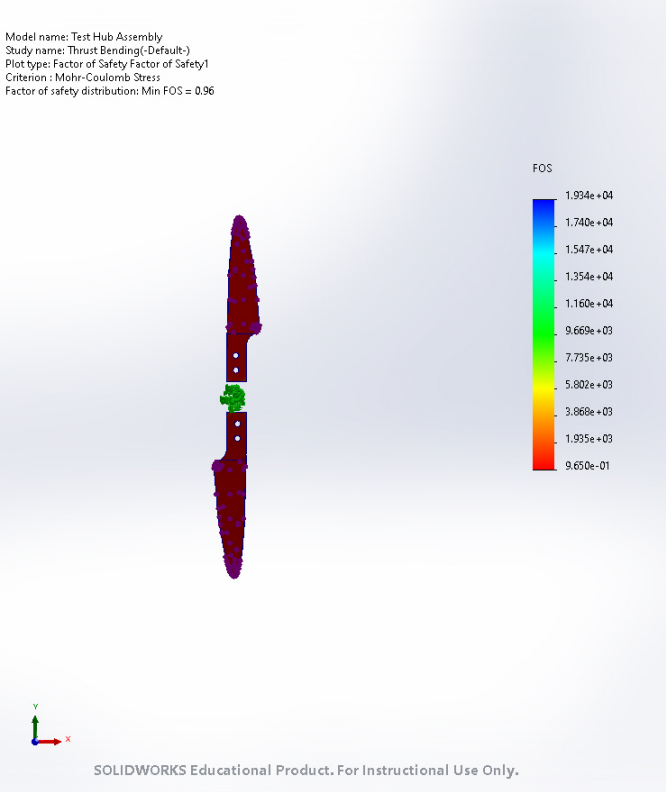

Figure 44: Test Assembly Thrust Bending Factor of Safety at 70N

Analysis	Torque Applied	FOS-Mohr Coulomb	Max Displacement (mm)
1	5Nm	9.3	0.3256
2	10Nm	4.7	0.6518
3	15Nm	3.1	0.9778
4	20Nm	2.3	1.306
5	25Nm	1.9	1.633
6	30Nm	1.6	1.959
7	35Nm	1.3	2.287
8	40Nm	1.2	2.615
9	45Nm	1	2.943
10	50Nm	0.93	3.272

Table 8: Test Assembly Torque Bending Study Results

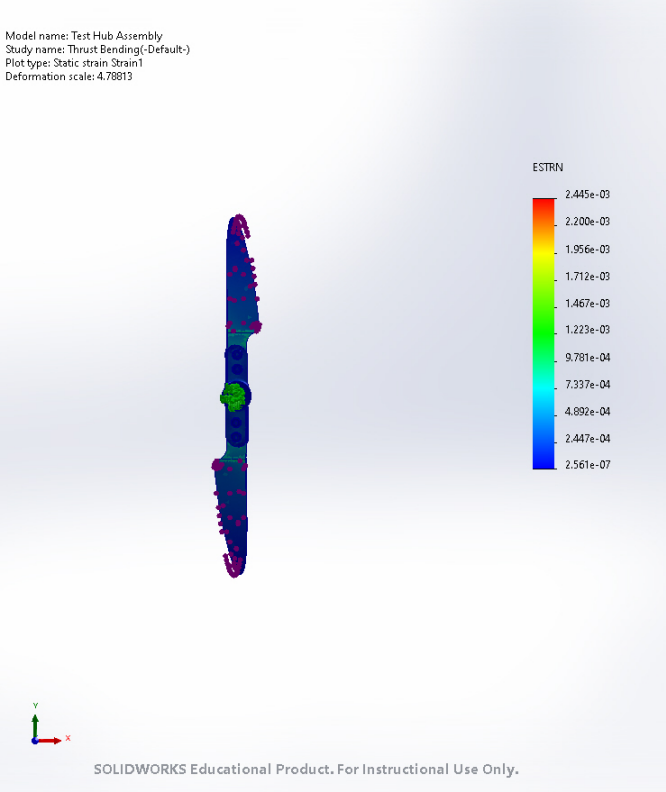

Figure 45: Test Assembly Thrust Bending Strain at 70N

4.3.4 Knife Compression Study

The compression of the ceramic knife between the washers in the hub assembly was modeled as well. The study was iterated until the Mohr Coulomb FOS reached 1 as shown in 9. The FOS of 1 was reached at 26kN of applied force in both directions on the washers attached to the ceramic knife (Figure 57).

4.4 Failure Analysis By Propeller Blade Geometry Results

Finite Element Analysis was performed on the test assembly to understand the response to various loading conditions typically experienced during spinning of a propeller. Each study was iterated until failure.

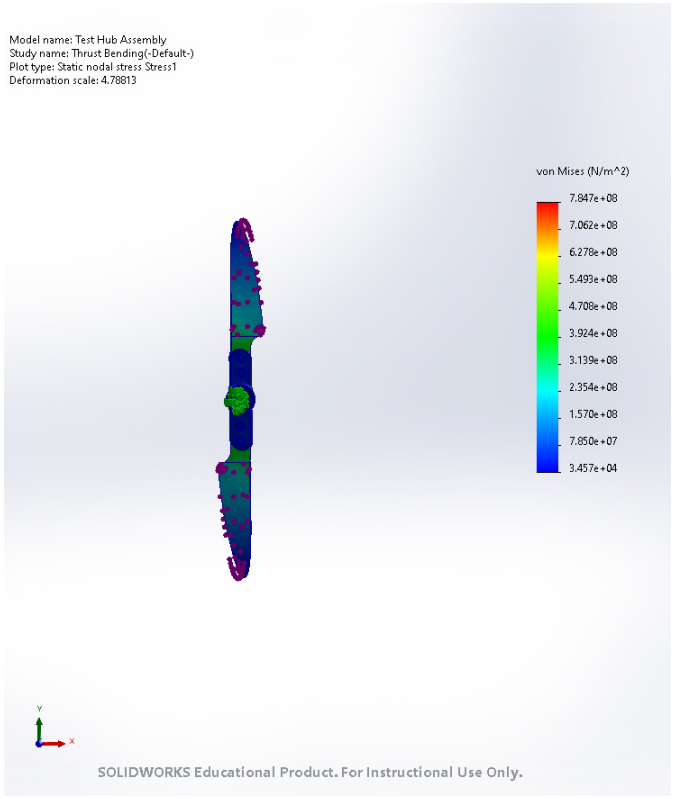

Figure 46: Test Assembly Thrust Bending Stress at 70N

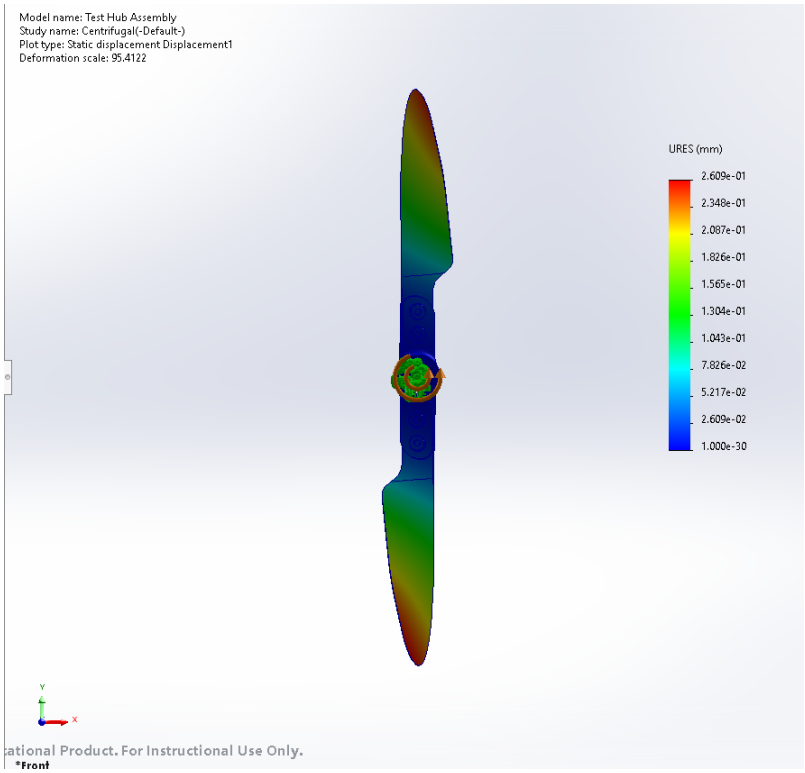

Figure 47: Test Assembly Displacement due to Centrifugal Loading at 19,000RPM (Front)

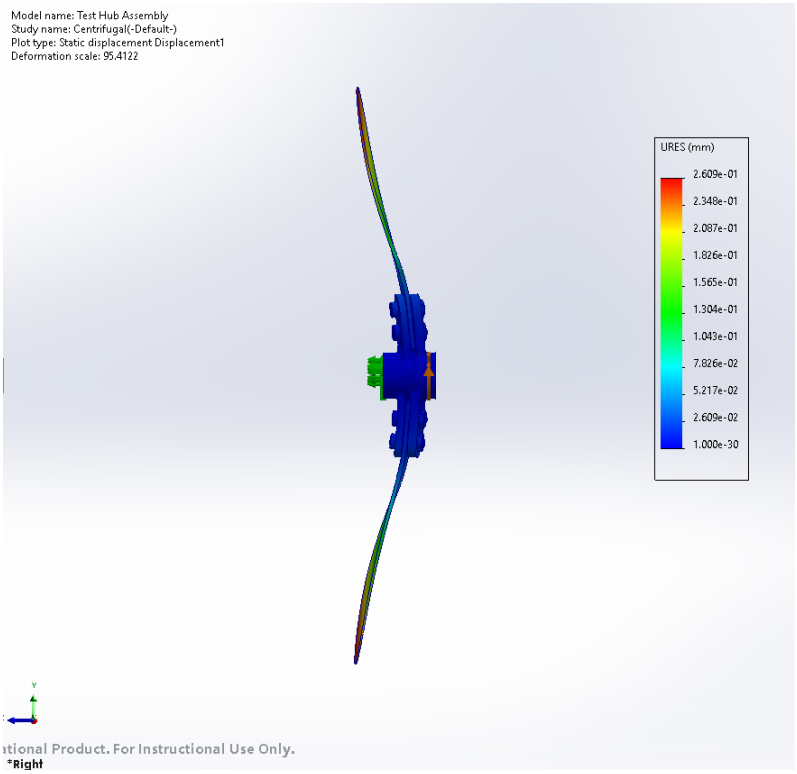

Figure 48: Test Assembly Displacement due to Centrifugal Loading at 19,000RPM (Right)

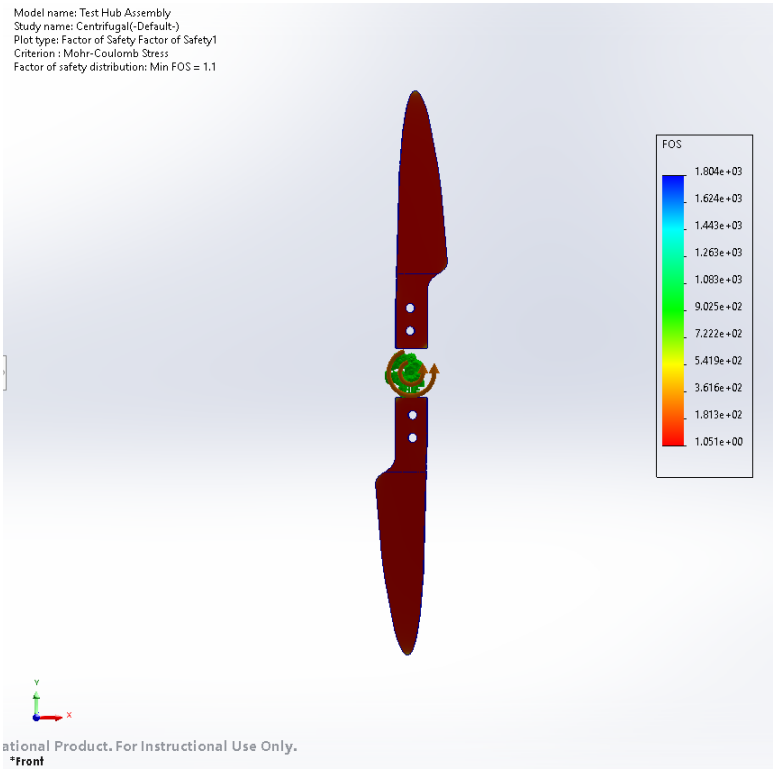

Figure 49: Test Assembly Centrifugal Loading Factor of Safety at 19,000RPM

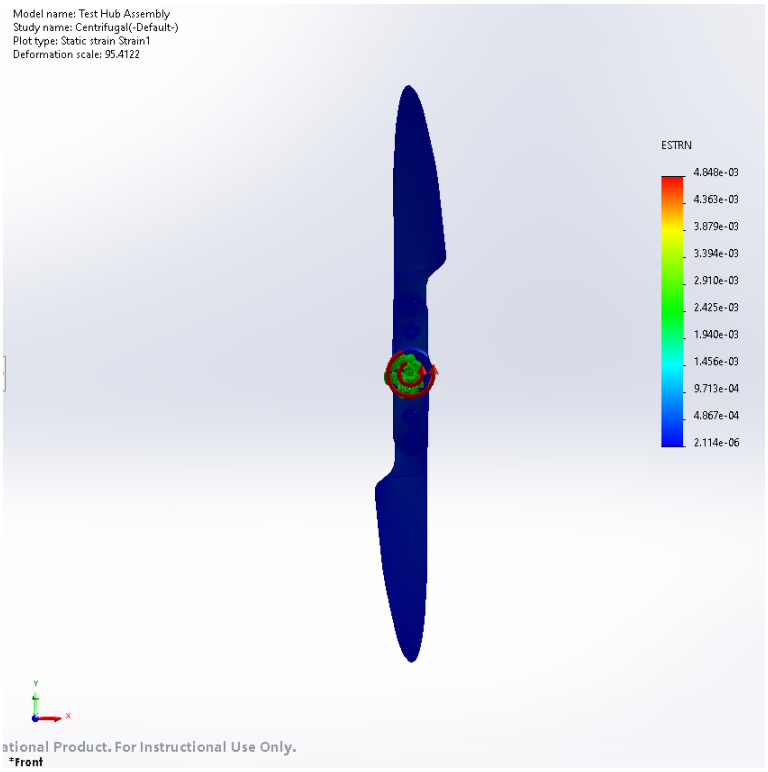

Figure 50: Test Assembly Centrifugal Loading Strain at 19,000RPM

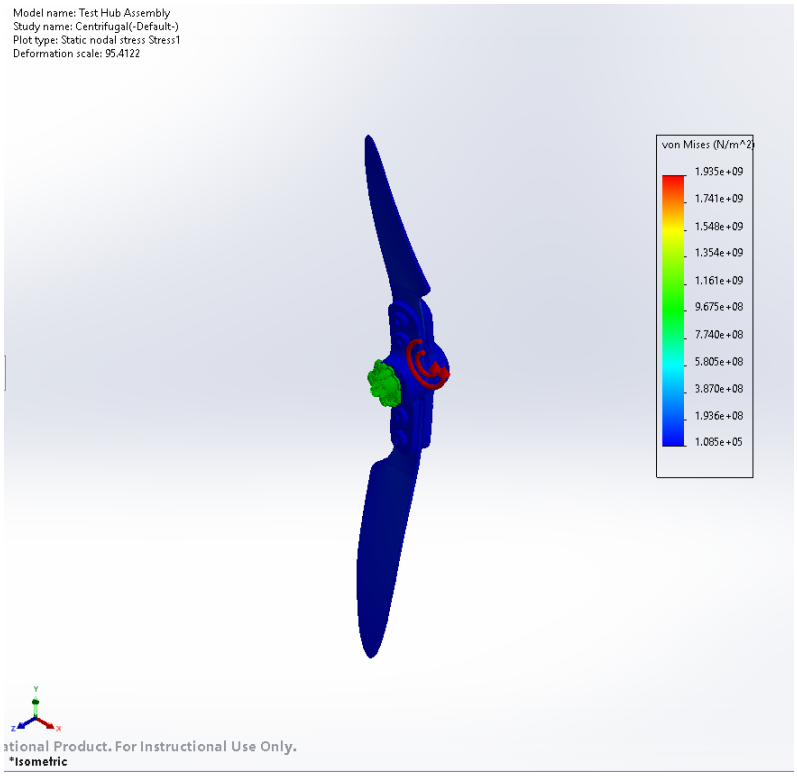

Figure 51: Test Assembly Centrifugal Loading Stress at 19,000RPM

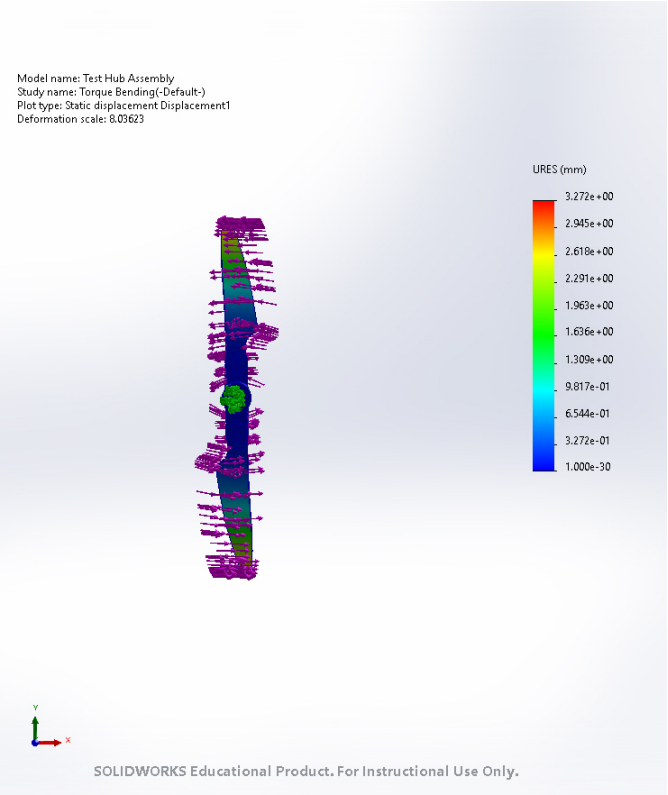

Figure 52: Test Assembly Displacement due to Torque Bending at 50Nm (Isometric)

Compressive Force	FOS
12kN	2.7
13kN	2.5
14kN	2.3
15kN	2.1
16kN	1.9
17kN	1.8
18kN	1.7
19kN	1.5
20kN	1.4
21kN	1.4
22kN	1.3
23kN	1.2
24kN	1.1
25kN	1.1
26kN	1

Table 9: Test Assembly Knife Compression Study Results

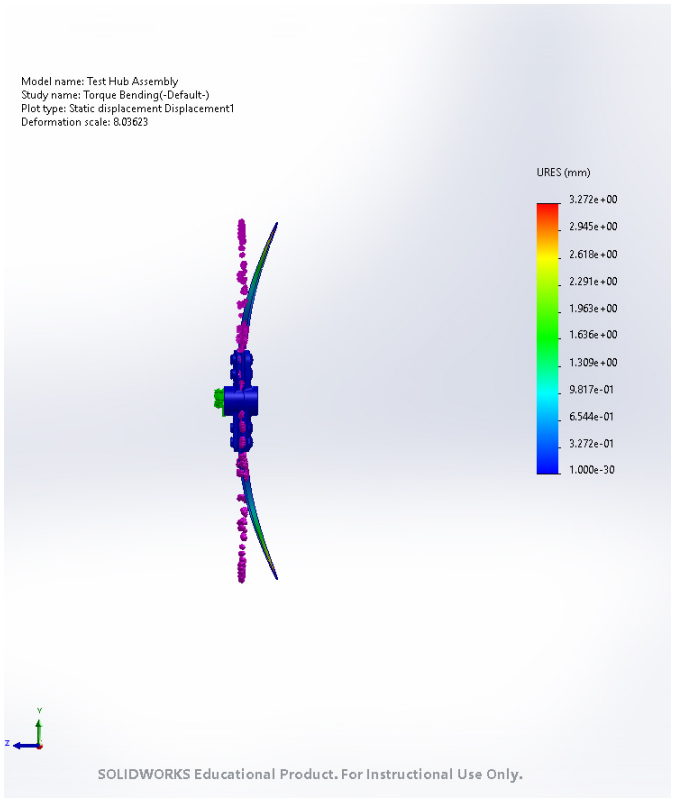

Figure 53: Test Assembly Displacement due to Torque Bending at 50Nm (Right)

Analysis	Force Applied	FOS-Mohr Coulomb	Max Displacement (mm)
1	10N	4.6	3.264
2	20N	2.3	6.526
3	30N	1.5	9.782
4	40N	1.2	13.03
5	50N	0.93	16.26

Table 10: Thrust Bending Failure Analysis-Thin Blade

4.4.1 Thrust Bending Forces

The thrust bending simulation was iterated until failure according to Mohr Coulomb criteria for brittle materials. The maximum deflection and minimum Factor of Safety (FOS) was determined for each simulation and recorded in tables 10-13. Failure was categorized as the applied force at which the Mohr Coulomb FOS was 1. FOS and max displacement at failure in Thrust bending was captured in figures 58-65.

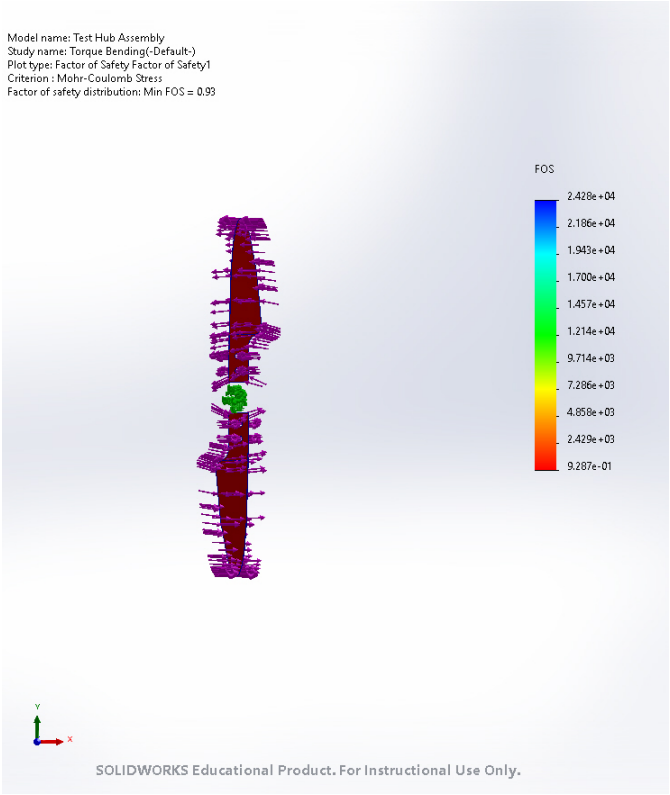

Figure 54: Test Assembly Torque Bending Factor of Safety at 50Nm

Analysis	Force Applied	FOS-Mohr Coulomb	Max Displacement (mm)
1	10N	4.9	3.272
2	20N	2.5	6.541
3	30N	1.6	9.805
4	40N	1.2	13.06
5	50N	0.99	16.3

Table 11: Thrust Bending Failure Analysis-Twisted Thin Blade

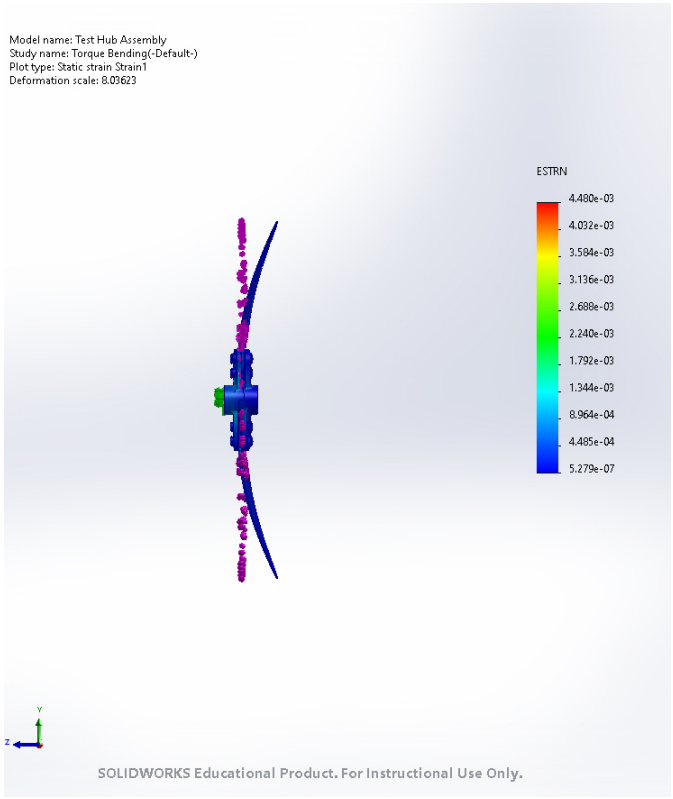

Figure 55: Test Assembly Torque Bending Strain at 50Nm

Analysis	Force Applied	FOS-Mohr Coulomb	Max Displacement (mm)
1	50N	15	0.3263
2	100N	7.4	0.6525
3	150N	4.9	0.9788
4	200N	3.7	1.305
5	250N	2.9	1.631
6	300N	2.5	1.958
7	350N	2.1	2.284
8	400N	1.8	2.61
9	450N	1.6	2.936
10	500N	1.5	3.263
11	550N	1.3	3.589
12	600N	1.2	3.915
13	650N	1.1	4.242
14	700N	1.1	4.568
15	750N	0.98	4.894

Table 12: Thrust Bending Failure Analysis-Simple Airfoil

Analysis	Force Applied	FOS-Mohr Coulomb	Max Displacement (mm)
1	50N	19	0.154
2	100N	9.7	0.308
3	150N	6.4	0.462
4	200N	4.8	0.616
5	250N	3.9	0.77
6	300N	3.2	0.924
7	350N	2.8	1.078
8	400N	2.4	1.232
9	450N	2.1	1.386
10	500N	1.9	1.54
11	550N	1.8	1.693
12	600N	1.6	1.847
13	650N	1.5	2.001
14	700N	1.4	2.155
15	750N	1.3	2.309
16	800N	1.2	2.463
17	850N	1.1	2.616
18	900N	1.1	2.77
19	950N	1	2.924
20	1000N	0.97	3.078

Table 13: Thrust Bending Failure Analysis-Twisted Blade with Airfoil

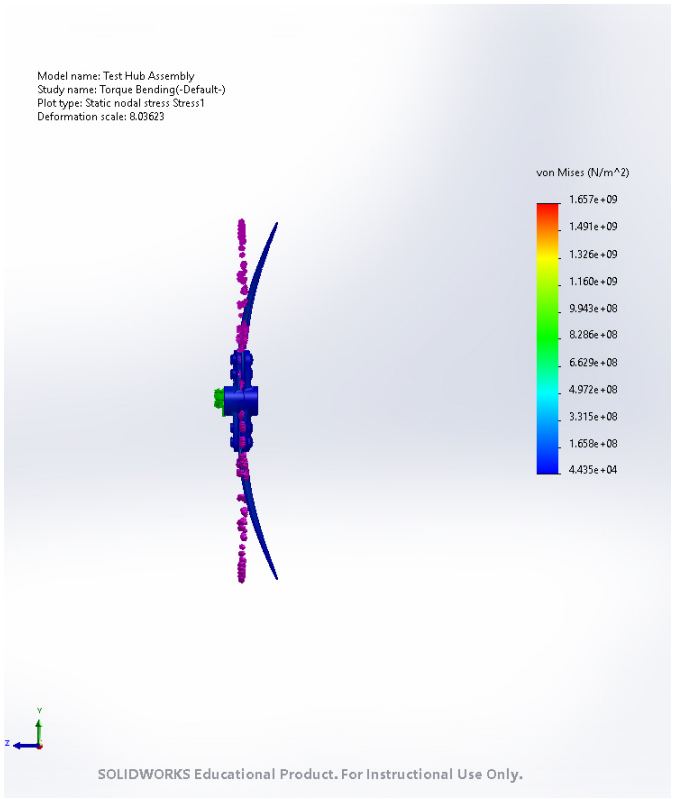

Figure 56: Test Assembly Torque Bending Stress at 50Nm

4.4.2 Centrifugal Loading

The centrifugal loading simulation was iterated until failure according to Mohr Coulomb criteria for brittle materials. The maximum deflection and minimum Factor of Safety (FOS) was determined for each simulation and recorded in tables 14-17. Failure was categorized as the applied force at which the Mohr Coulomb FOS was 1. FOS and max displacement at failure in centrifugal loading was captured in figures 74-81.

4.4.3 Torque Bending Forces

The torque bending simulation was iterated until failure according to Mohr Coulomb criteria for brittle materials. The maximum deflection and minimum Factor of Safety (FOS) was determined for each simulation and recorded in tables 18-21. Failure was categorized as the applied force at which the Mohr Coulomb FOS was 1. FOS and max displacement at failure in torque bending was captured in figures 74-79.

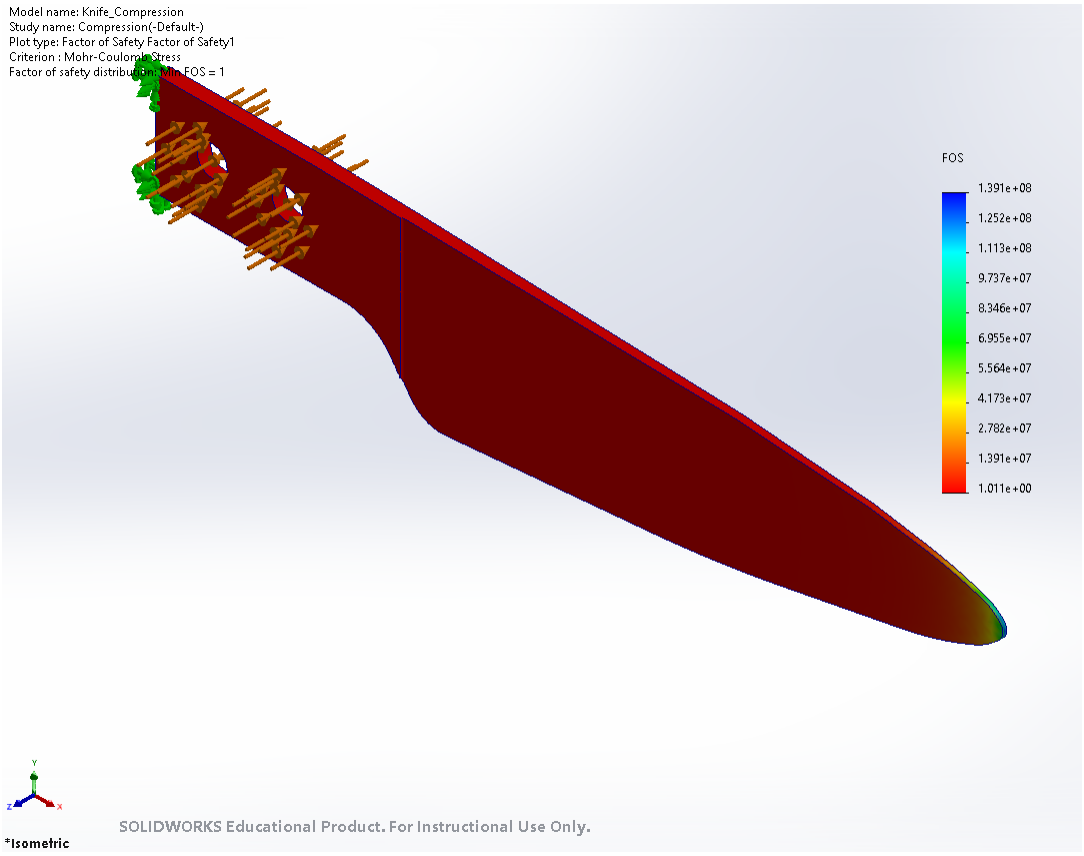

Figure 57: Test Assembly Knife Compression Factor of Safety

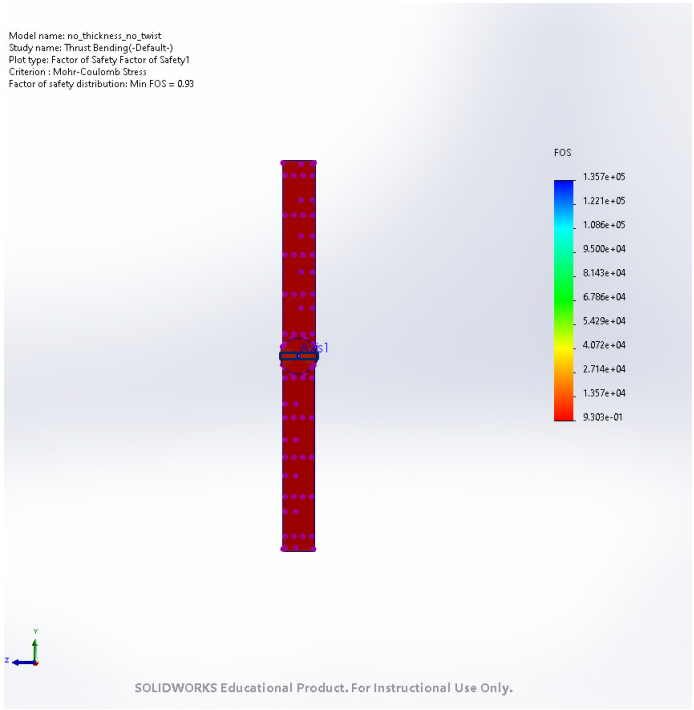

Figure 58: Thin Blade Thrust Bending FOS at 50N

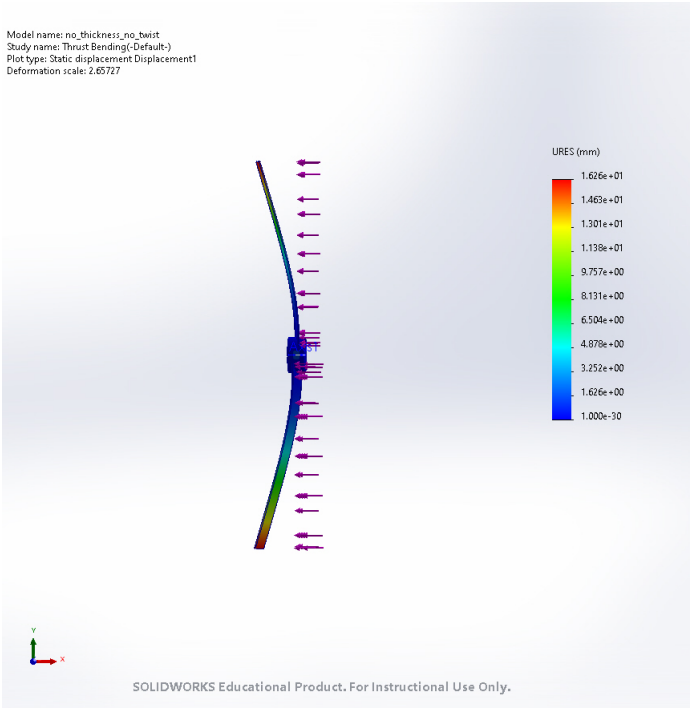

Figure 59: Thin Blade Thrust Bending Displacement at 50N

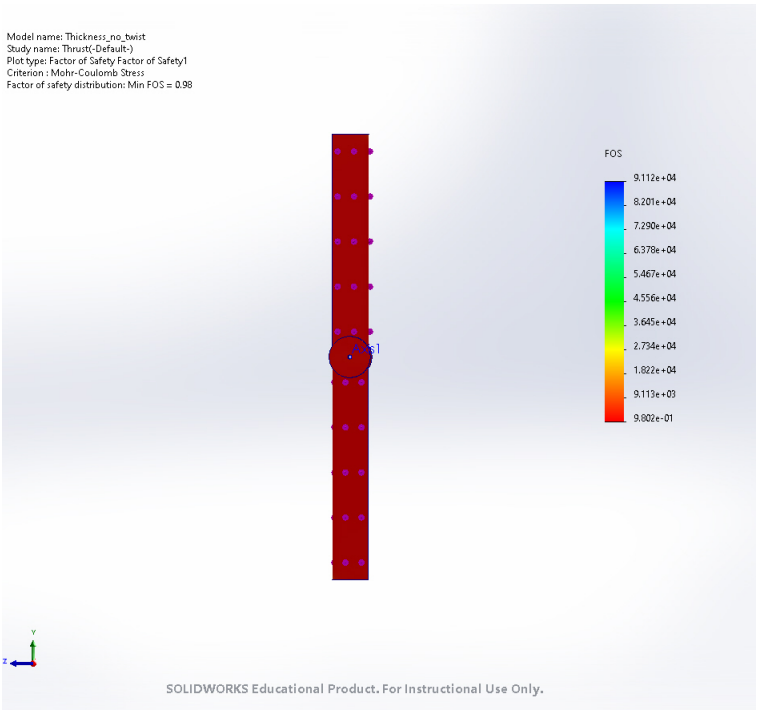

Figure 60: Simple Airfoil Thrust Bending FOS at 750N

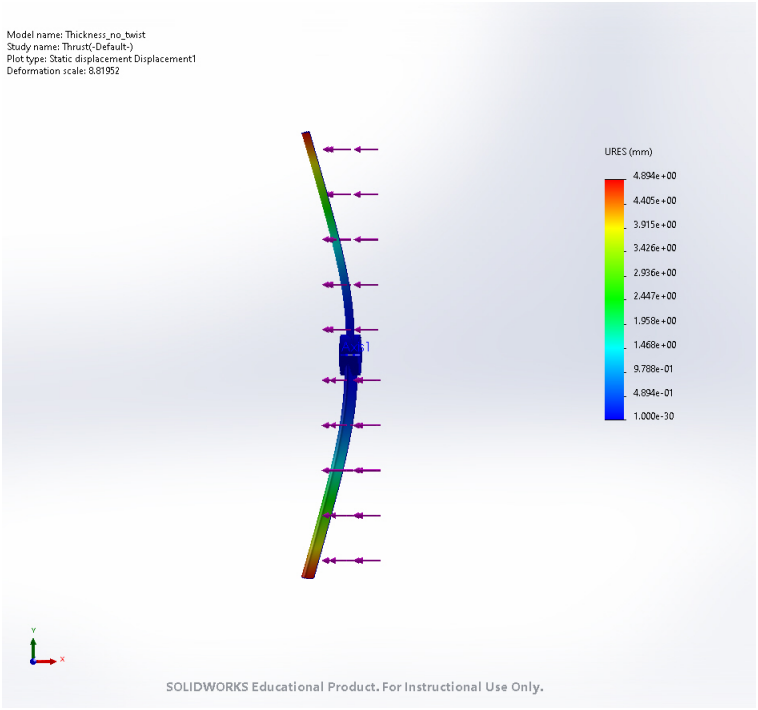

Figure 61: Simple Airfoil Thrust Bending Displacement at 750N

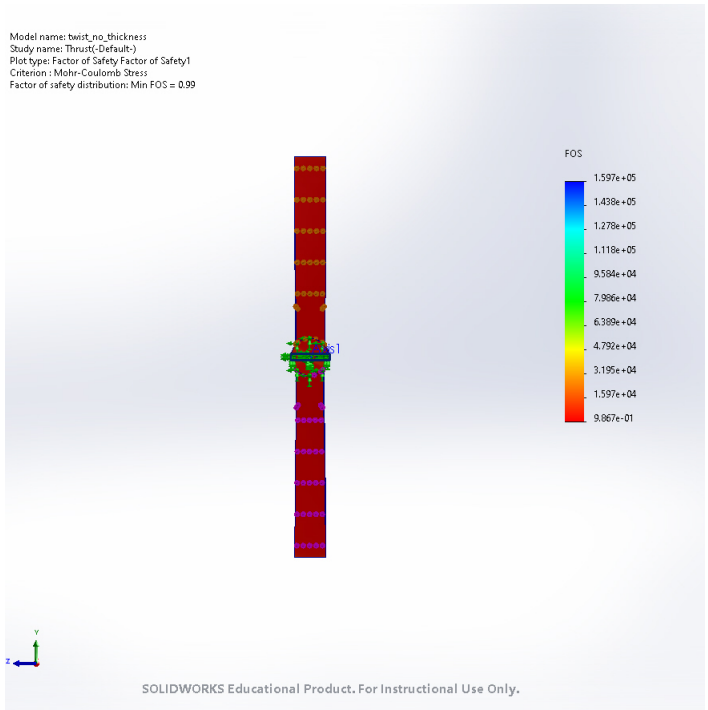

Figure 62: Twisted Thin Blade Thrust Bending FOS at 50N

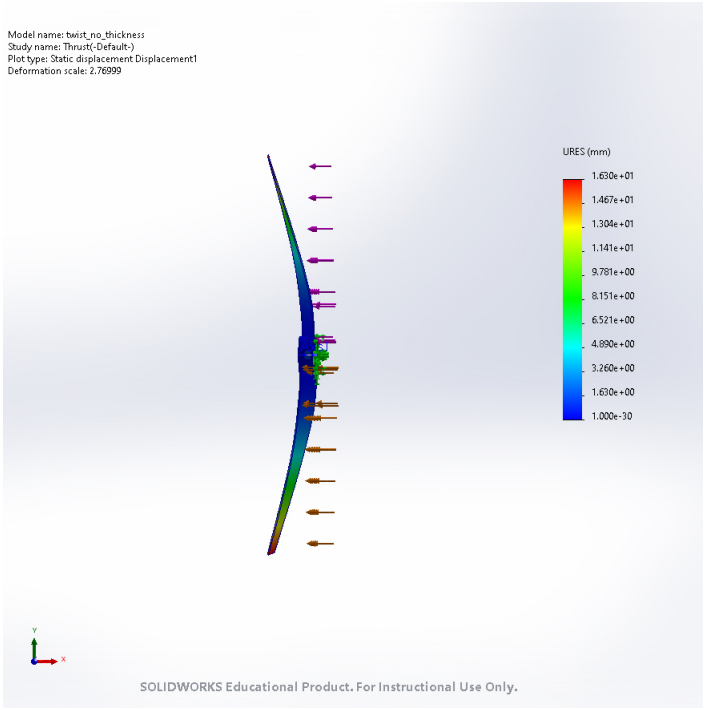

Figure 63: Twisted Thin Blade Thrust Bending Displacement at 50N

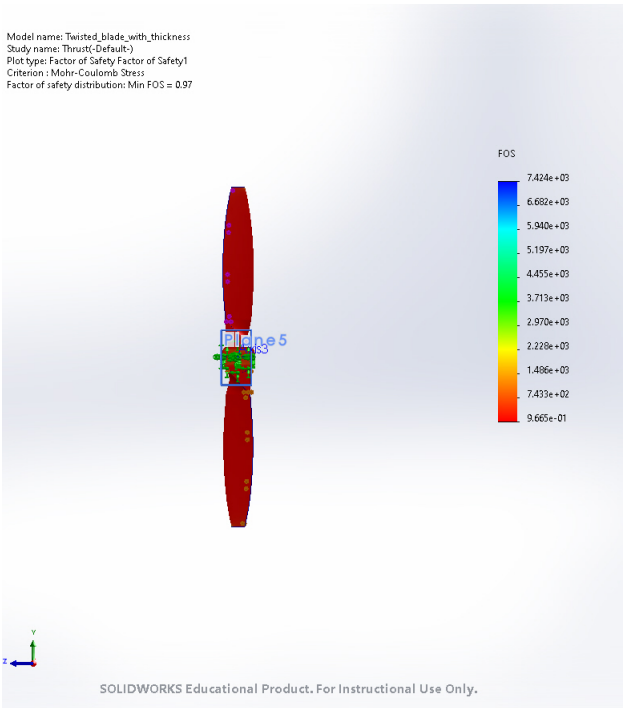

Figure 64: Twisted Blade with Airfoil Thrust Bending FOS at 1kN

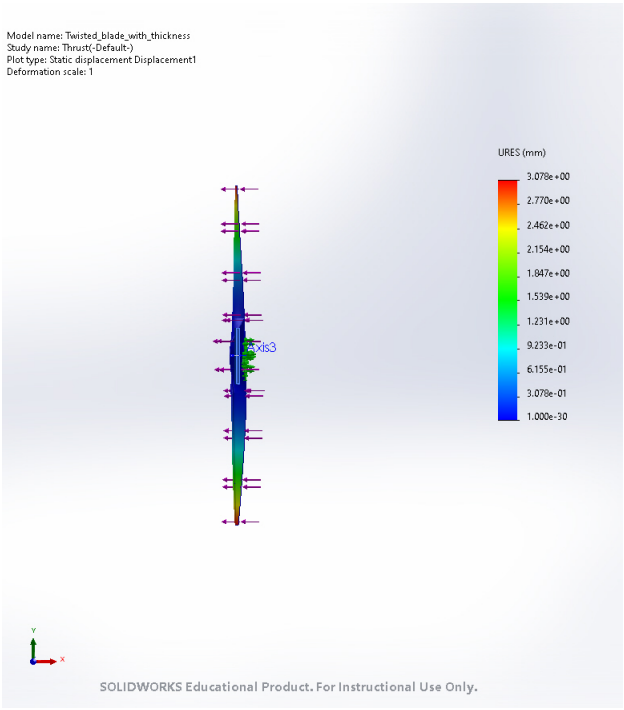

Figure 65: Twisted Blade with Airfoil Thrust Bending Displacement at 1kN

Analysis	Rad/s	RPM	FOS-Mohr Coulomb	Max Displacement (mm)
1	523	5,000	10	0.0987
2	628	6,000	7.2	0.1422
3	733	7,000	5.3	0.1938
4	837	8,000	4.1	0.2527
5	942	9,000	3.2	0.3200
6	1047	10,000	2.6	0.3953
7	1152	11,000	2.1	0.4786
8	1256	12,000	1.8	0.5689
9	1361	13,000	1.5	0.6680
10	1466	14,000	1.3	0.7751
11	1570	15,000	1.2	0.8890
12	1657	16,000	1	0.9902
13	1780	17,000	0.9	1.1430

Table 14: Centrifugal Loading Failure Analysis-Thin Blade

Analysis	Rad/s	RPM	FOS-Mohr Coulomb	Max Displacement (mm)
1	523	5,000	9.8	0.0261
2	628	6,000	6.8	0.0376
3	733	7,000	5	0.0512
4	837	8,000	3.8	0.0667
5	942	9,000	3	0.0845
6	1047	10,000	2.4	0.1044
7	1152	11,000	2	0.1264
8	1256	12,000	1.7	0.1502
9	1361	13,000	1.4	0.1764
10	1466	14,000	1.2	0.2047
11	1570	15,000	1.1	0.2347
12	1657	16,000	0.98	0.2615

Table 15: Centrifugal Loading Failure Analysis-Twisted Thin Blade

Analysis	Rad/s	RPM	FOS-Mohr Coulomb	Max Displacement (mm)
1	523	5,000	8.8	0.1403
2	628	6,000	6.3	0.1955
3	733	7,000	4.6	0.2663
4	837	8,000	3.5	0.3472
5	942	9,000	2.8	0.4398
6	1047	10,000	2.3	0.5433
7	1152	11,000	1.9	0.6578
8	1256	12,000	1.6	0.7819
9	1361	13,000	1.3	0.9181
10	1466	14,000	1.2	1.0650
11	1570	15,000	1	1.2220
12	1657	16,000	0.9	1.3610

Table 16: Centrifugal Loading Failure Analysis-Simple Airfoil

Analysis	Rad/s	RPM	FOS-Mohr Coulomb	Max Displacement (mm)
1	523	5,000	14	0.0770
2	628	6,000	9.8	0.1077
3	733	7,000	7.2	0.1418
4	837	8,000	5.5	0.1780
5	942	9,000	4.4	0.2164
6	1047	10,000	3.5	0.2558
7	1152	11,000	2.9	0.2956
8	1256	12,000	2.5	0.3350
9	1361	13,000	2.1	0.3743
10	1466	14,000	1.8	0.4128
11	1570	15,000	1.6	0.4499
12	1657	16,000	1.4	0.4800
13	1780	17,000	1.2	0.5211
14	1884	18,000	1.1	0.5544
15	1989	19,000	1	0.5867
16	2094	20,000	0.91	0.6176

Table 17: Centrifugal Loading Failure Analysis-Twisted Blade with Airfoil

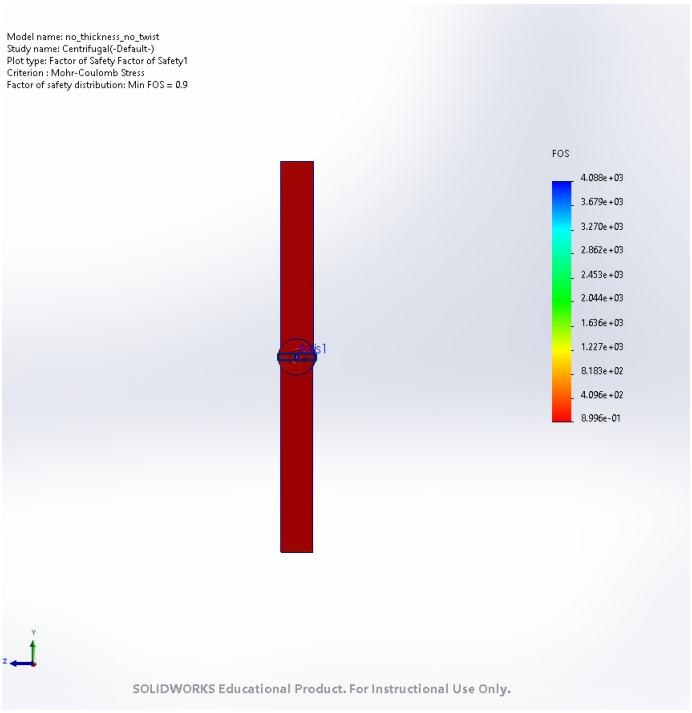

Figure 66: Thin Blade Centrifugal Loading FOS at 1780rad/sec

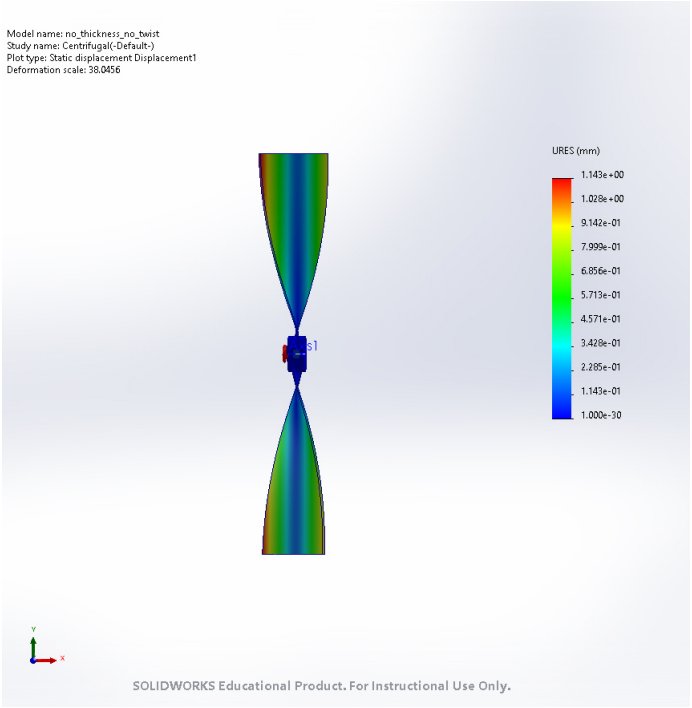

Figure 67: Thin Blade Centrifugal Loading Displacement at 1780rad/sec

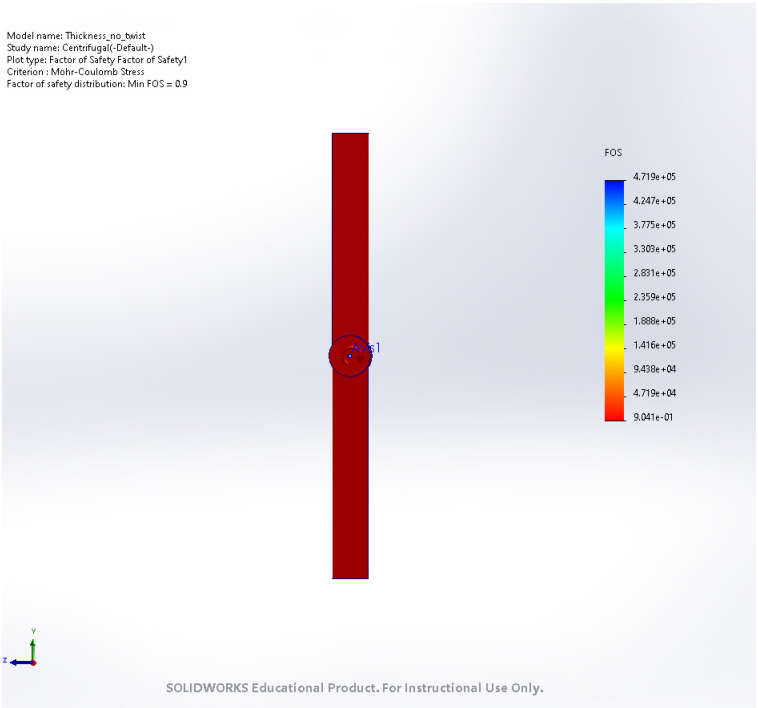

Figure 68: Simple Airfoil Centrifugal Loading FOS at 1657rad/sec

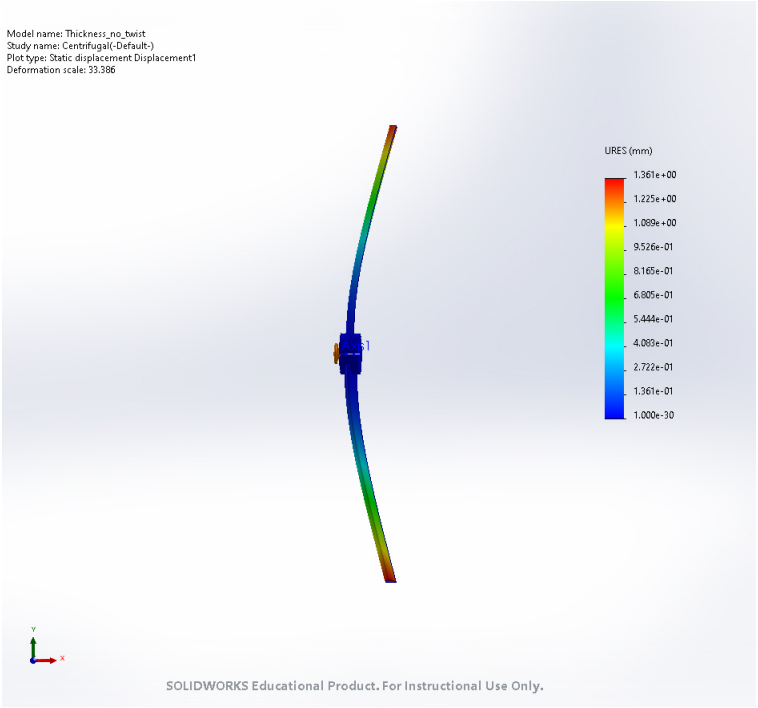

Figure 69: Simple Airfoil Centrifugal Loading Displacement at 1657rad/sec

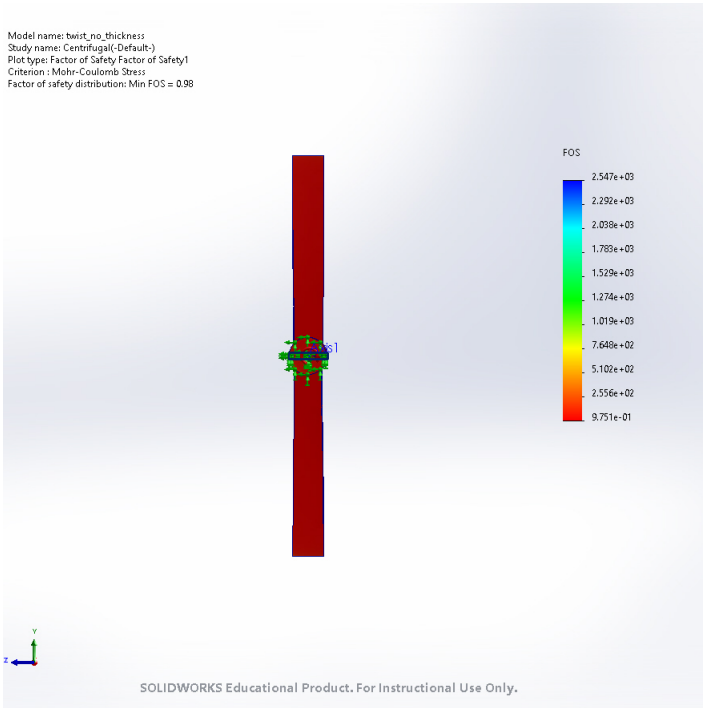

Figure 70: Twisted Thin Blade Centrifugal Loading FOS at 1657rad/sec

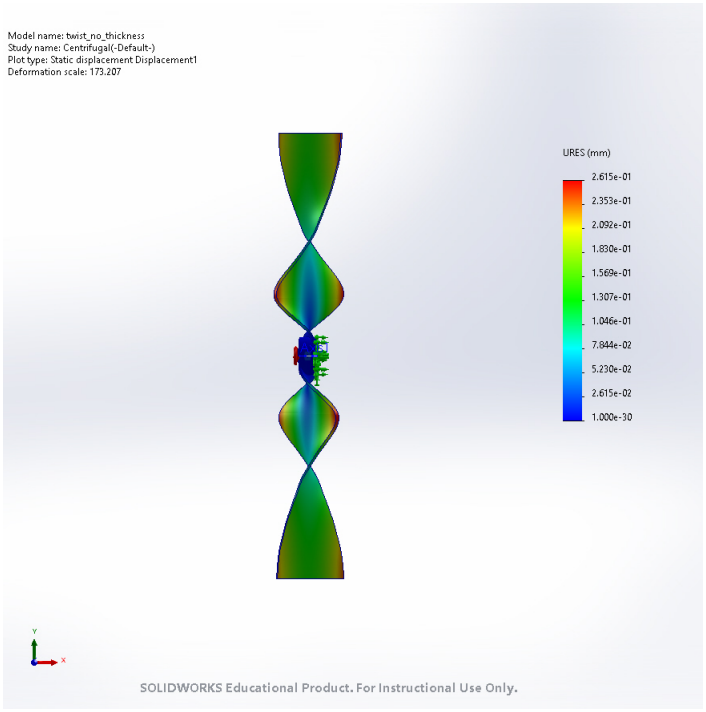

Figure 71: Twisted Thin Blade Centrifugal Loading Displacement at 1657rad/sec

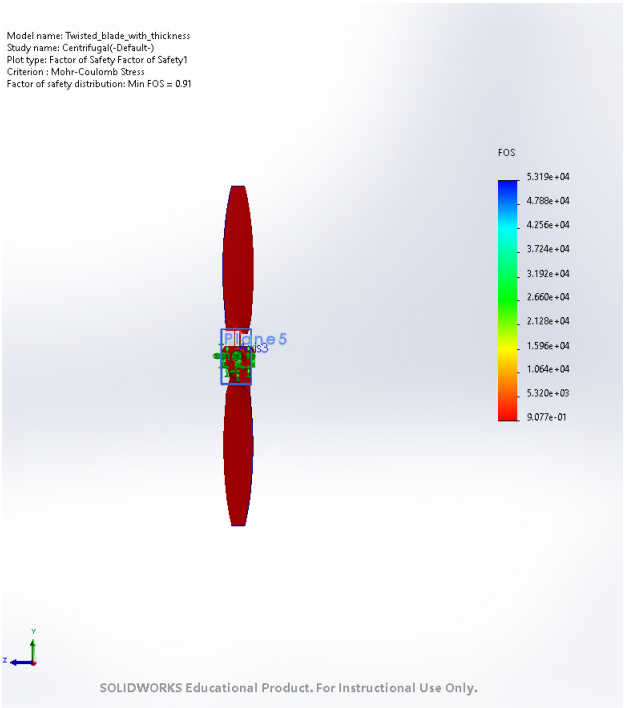

Figure 72: Twisted Blade with Airfoil Centrifugal Loading FOS at 2095rad/sec

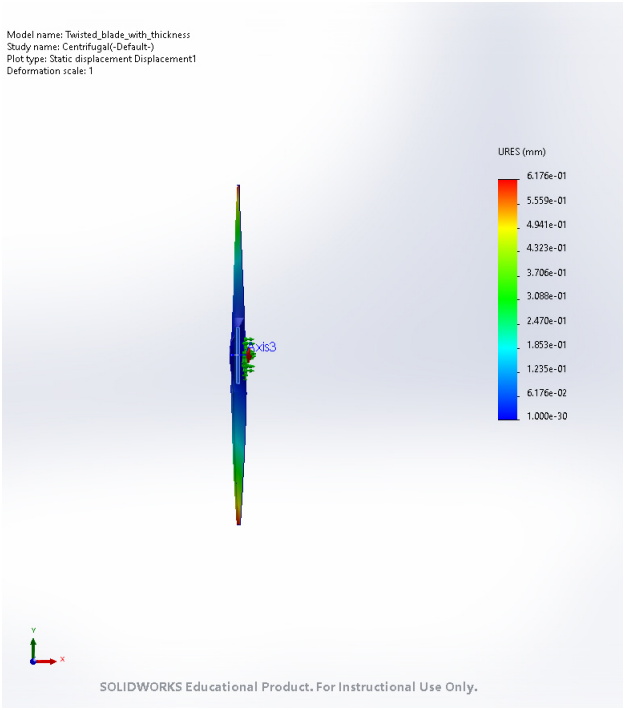

Figure 73: Twisted Blade with Airfoil Centrifugal Loading Displacement at 2095rad/sec

Analysis	Torque Applied	FOS-Mohr Coulomb	Max Displacement (mm)
1	5Nm	13	1.23
2	10Nm	6.2	2.464
3	15Nm	4.2	3.702
4	20Nm	3.1	4.946
5	25Nm	2.5	6.197
6	30Nm	2	7.457
7	35Nm	1.7	8.729
8	40Nm	1.5	10.02
9	45Nm	1.3	11.3
10	50Nm	1.2	11.26
11	55Nm	1.1	13.92
12	60Nm	1	15.26
13	65Nm	0.92	16.62

Table 18: Torque Bending Failure Analysis-Thin Blade

Analysis	Torque Applied	FOS-Mohr Coulomb	Max Displacement (mm)
1	5Nm	5.6	2.579
2	10Nm	2.8	5.162
3	15Nm	1.9	7.748
4	20Nm	1.4	10.034
5	25Nm	1.1	12.93
6	30Nm	0.92	15.53

Table 19: Torque Bending Failure Analysis-Twisted Thin Blade

Analysis	Torque Applied	FOS-Mohr Coulomb	Max Displacement (mm)
1	50Nm	13	0.2638
2	100Nm	6.4	0.5275
3	150Nm	4.2	0.7913
4	200Nm	3.2	1.055
5	250Nm	2.5	1.1319
6	300Nm	2.1	1.583
7	350Nm	1.8	1.846
8	400Nm	1.6	2.11
9	450Nm	1.4	2.374
10	500Nm	1.3	2.638
11	550Nm	1.2	2.902
12	600Nm	1.1	3.165
13	650Nm	0.98	3.429

Table 20: Torque Bending Failure Analysis-Simple Airfoil

Analysis	Torque Applied	FOS-Mohr Coulomb	Max Displacement (mm)
1	50Nm	7.7	0.2153
2	100Nm	3.8	0.4306
3	150Nm	2.6	0.6458
4	200Nm	1.9	0.861
5	250Nm	1.5	1.076
6	300Nm	1.3	1.291
7	350Nm	1.1	1.506
8	400Nm	0.96	1.722

Table 21: Torque Bending Failure Analysis-Twisted Blade with Airfoil

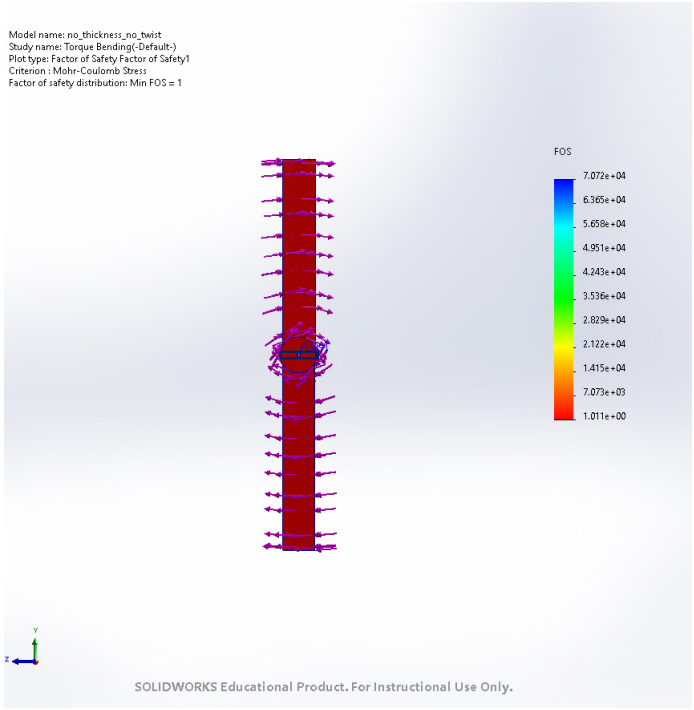

Figure 74: Thin Blade Torque Bending FOS at 60Nm

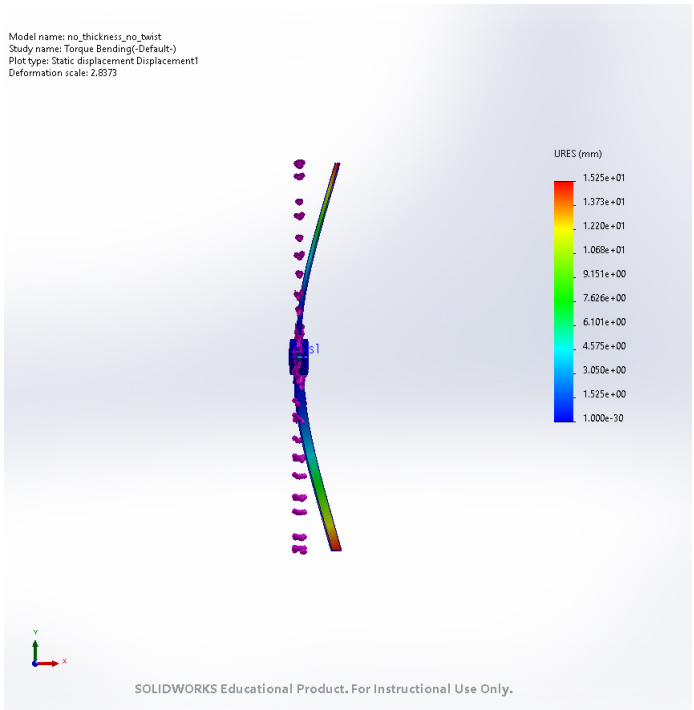

Figure 75: Thin Blade Torque Bending Displacement at 60Nm

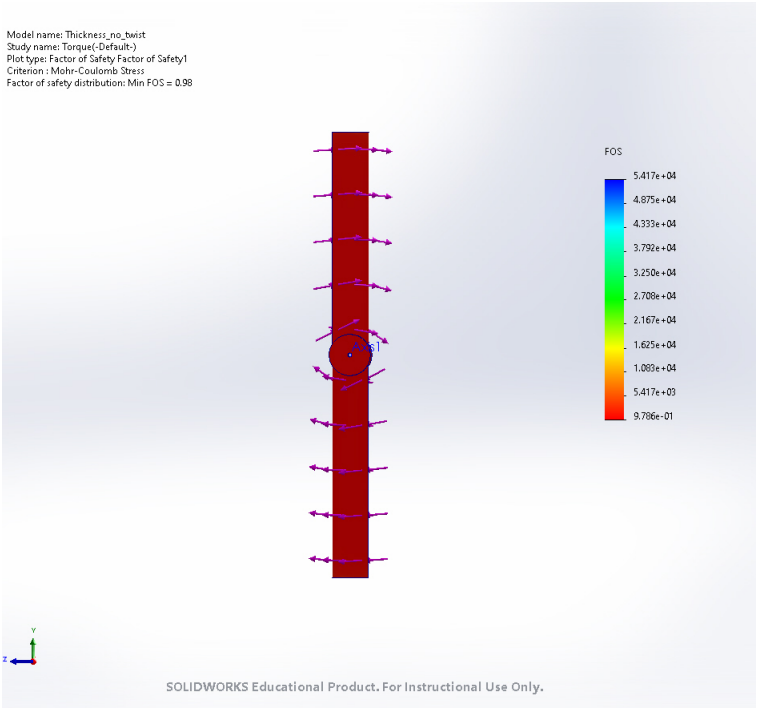

Figure 76: Simple Airfoil Torque Bending FOS at 650Nm

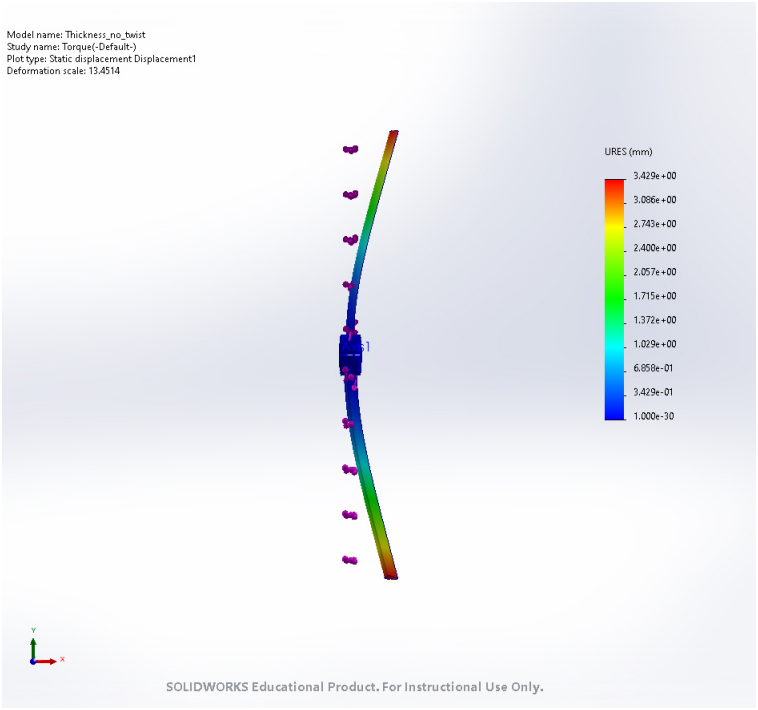

Figure 77: Simple Airfoil Torque Bending Displacement at 650Nm

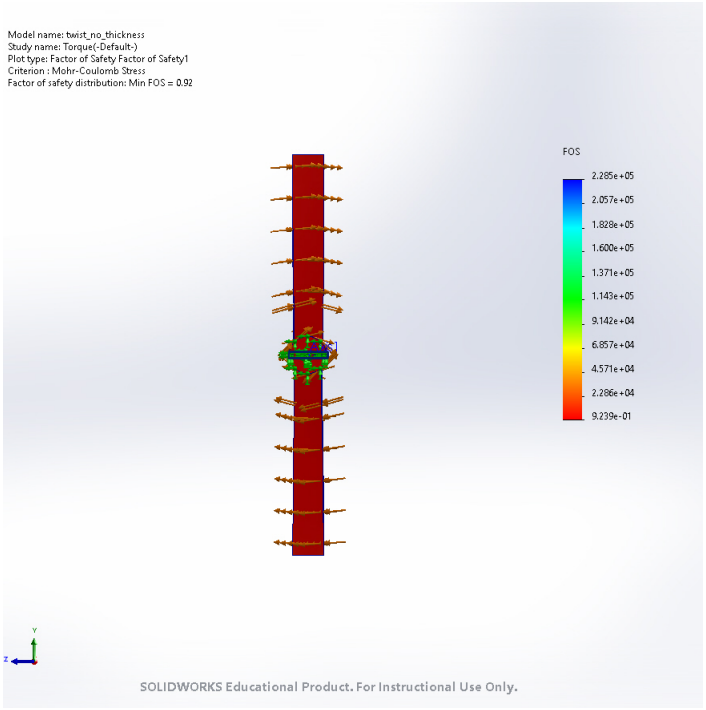

Figure 78: Twisted Thin Blade Torque Bending FOS at 30Nm

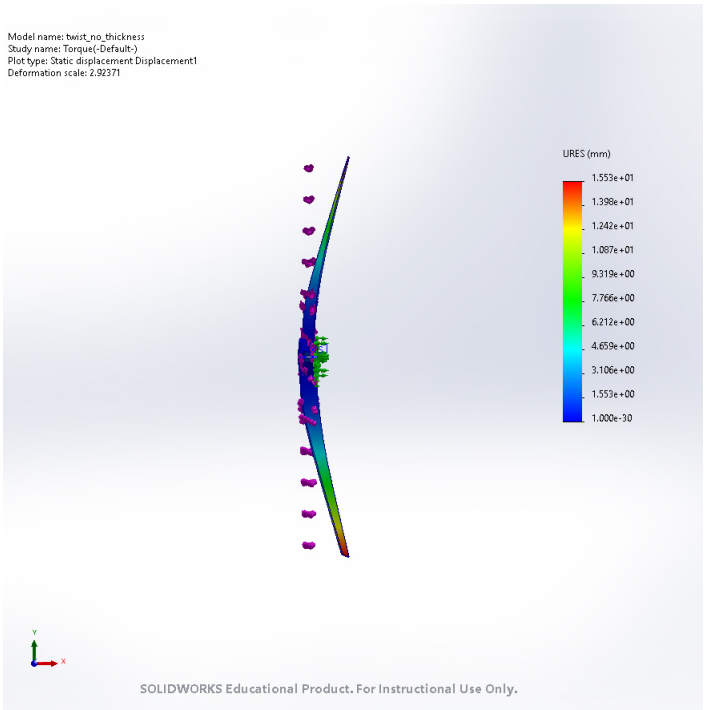

Figure 79: Twisted Thin Blade Torque Bending Displacement at 30Nm

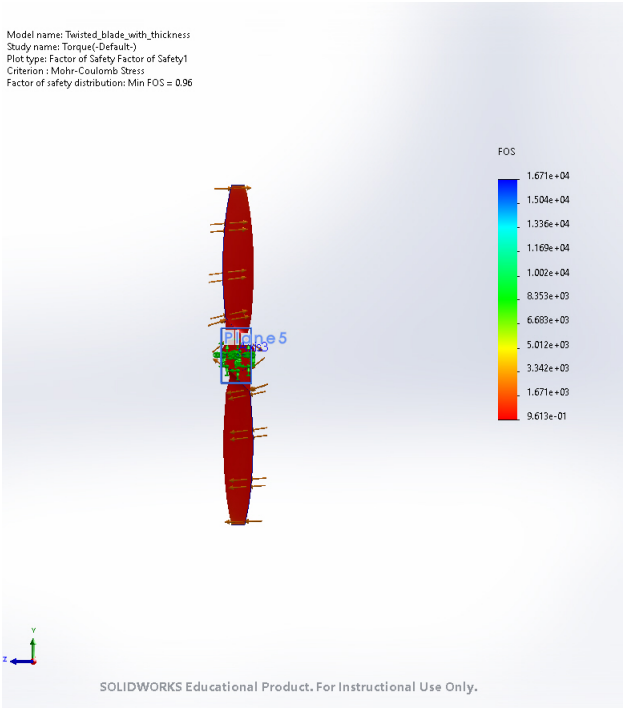

Figure 80: Twisted Blade with Airfoil Torque Bending FOS at 400Nm

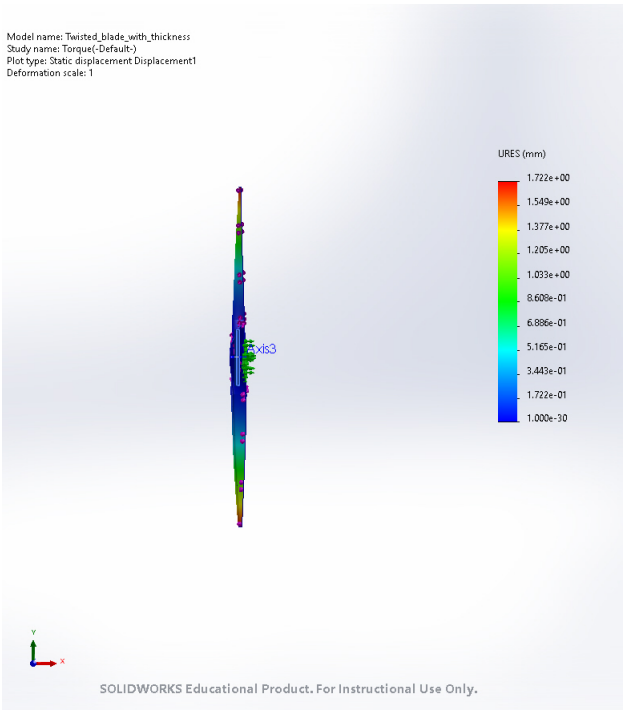

Figure 81: Twisted Blade with Airfoil Torque Bending Displacement at 400Nm

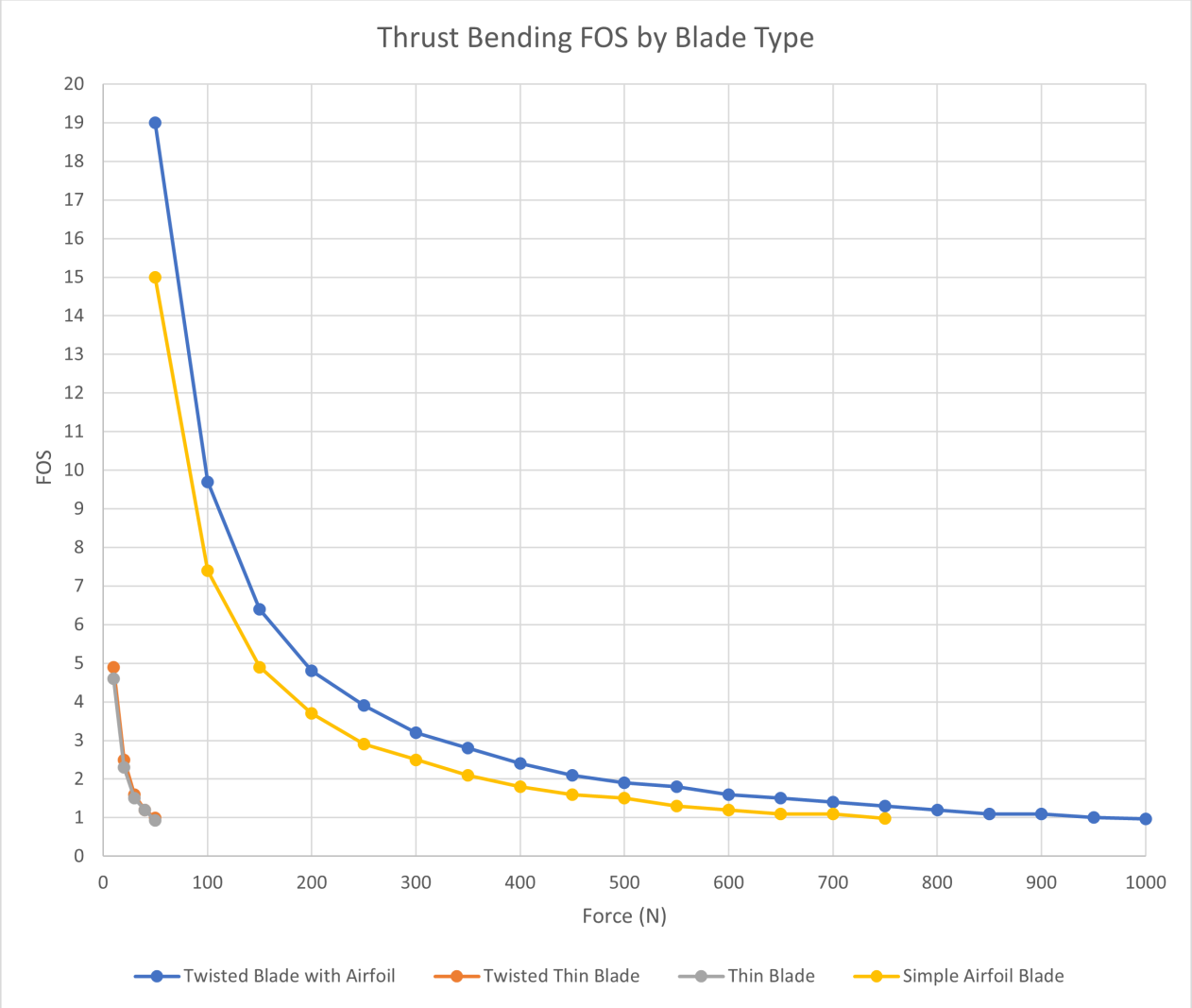

Figure 82: Thrust Bending FOS by Blade Type

4.4.4 Blade Type FOS and Displacement Comparison

Each iteration of of the failure analyses were charted based on the input thrust force vs FOS and Displacement (Figures 82 and 83). Additionally, each iteration of of the failure analyses were charted based on the input RPM vs FOS and Displacement (Figures 84 and 85). Also, each iteration of of the failure analyses were charted based on the input torque vs FOS and Displacement (Figures 86 and 87).

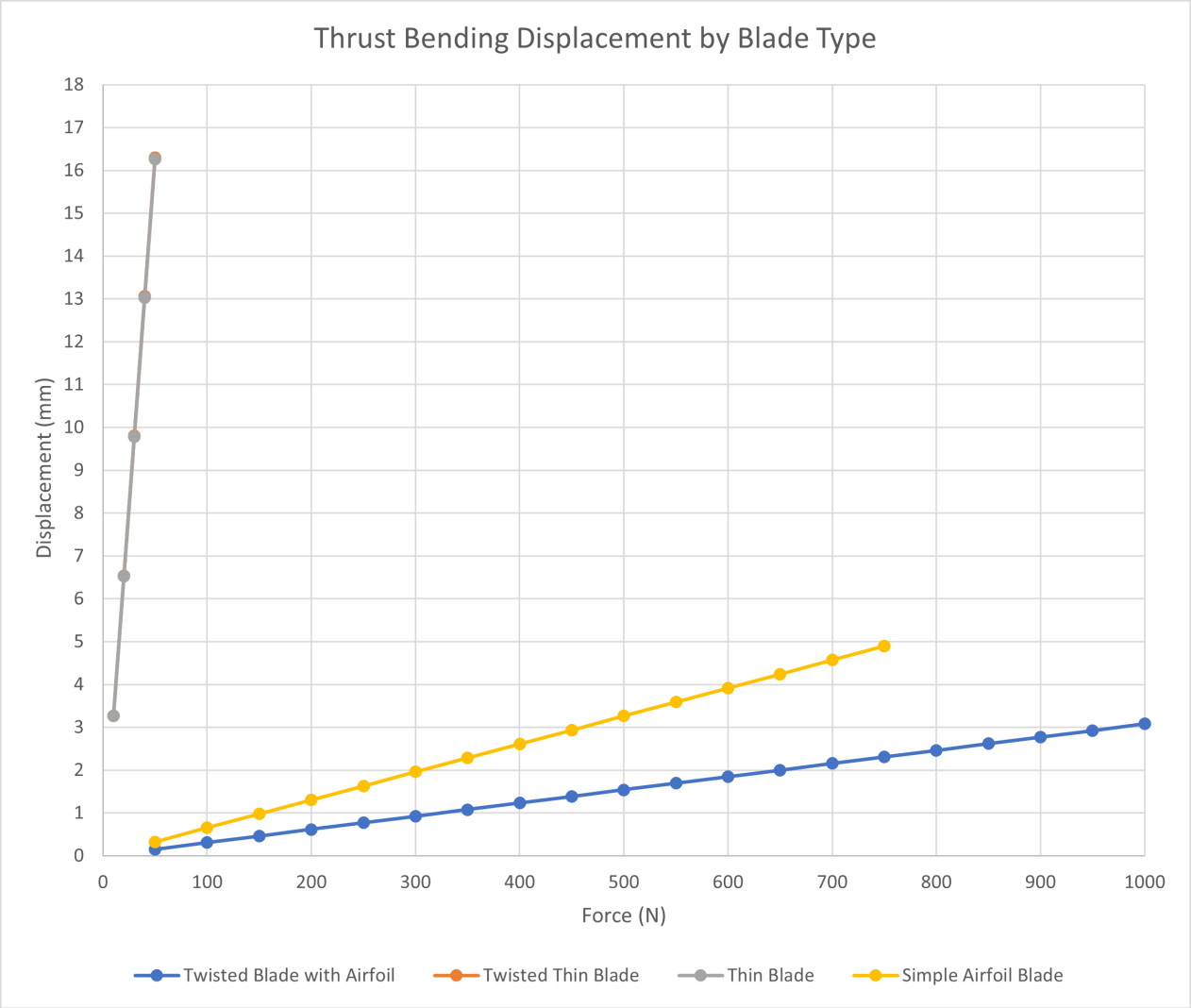

Figure 83: Thrust Bending Displacement by Blade Type

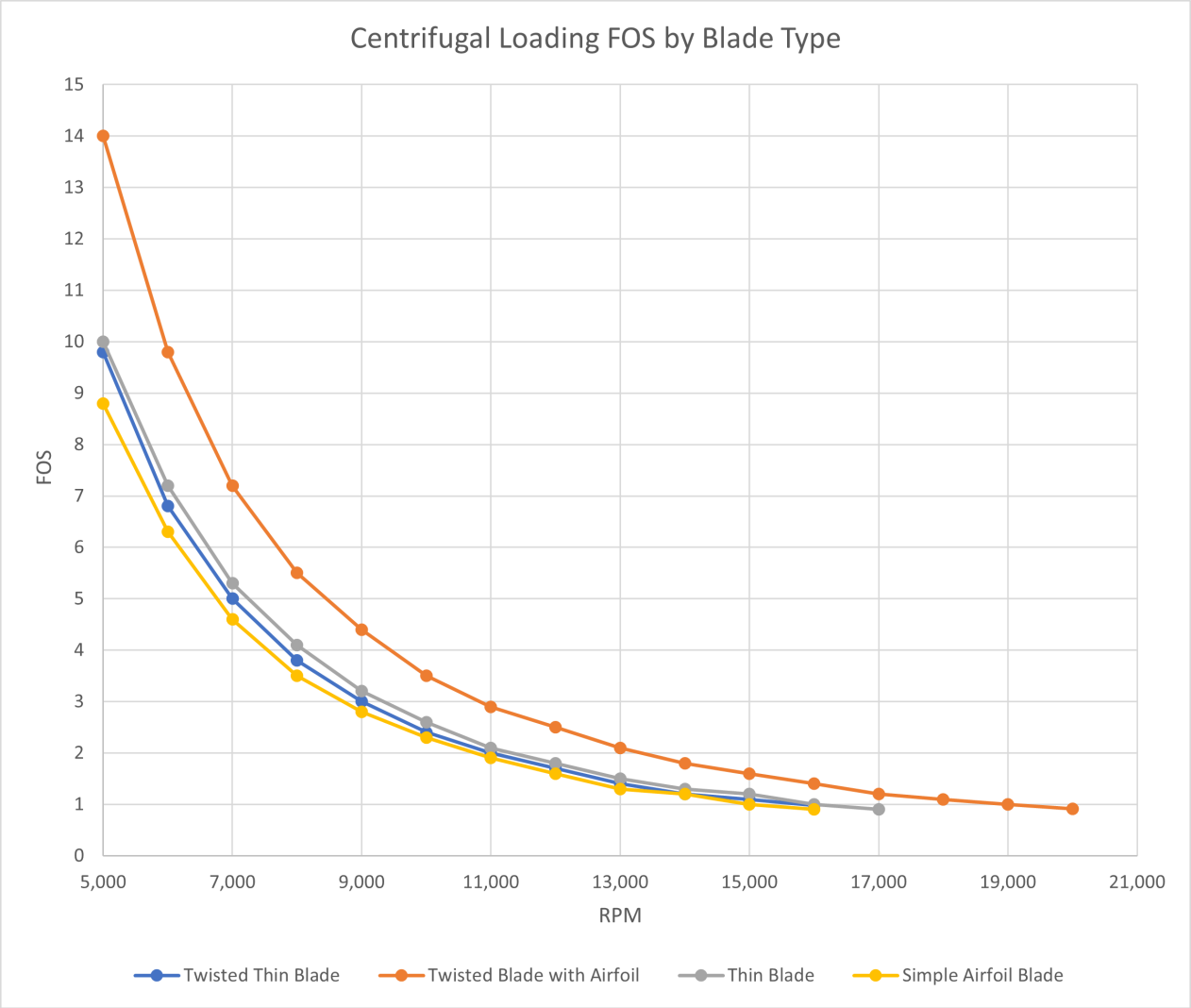

Figure 84: Centrifugal Loading FOS by Blade Type

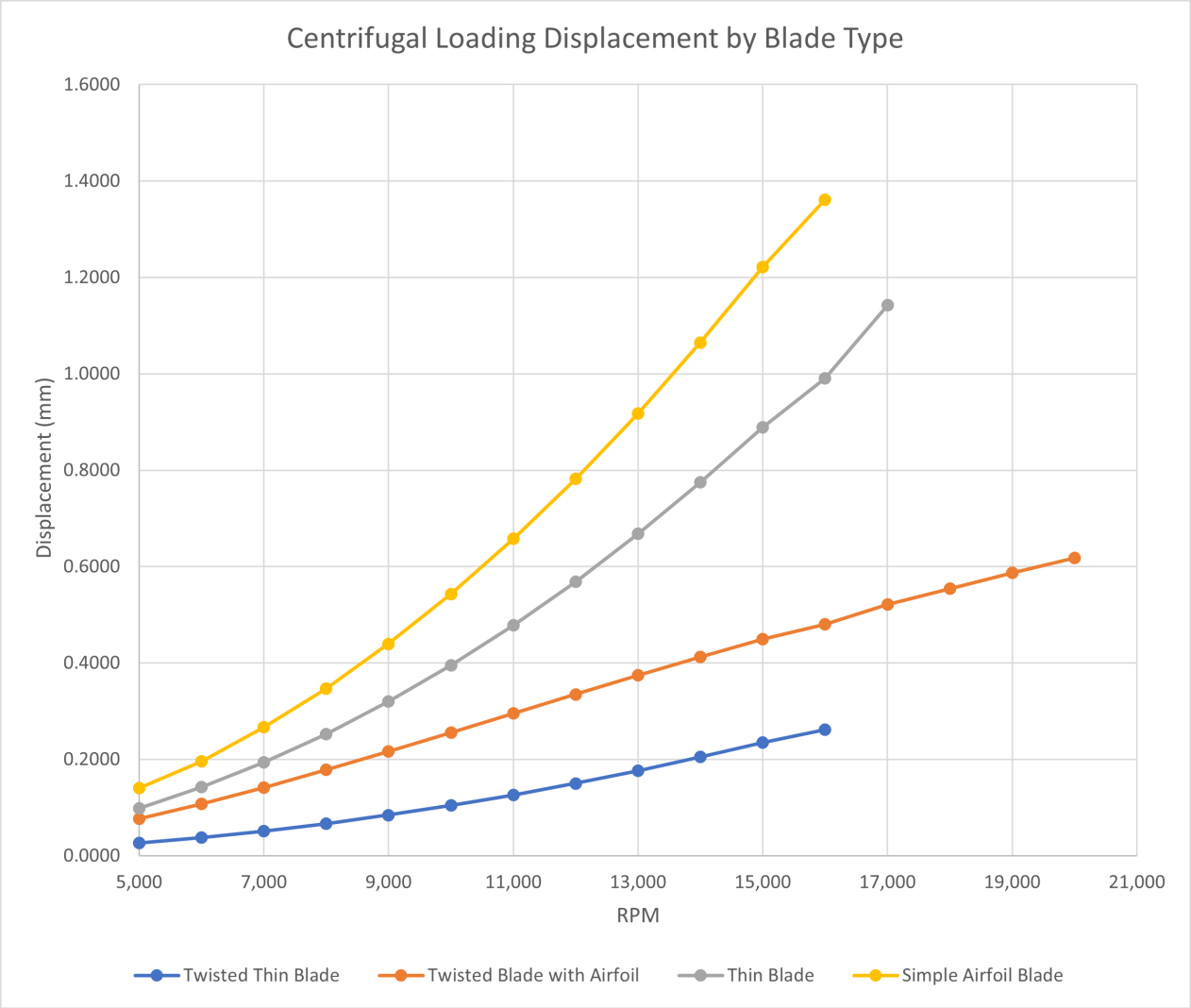

Figure 85: Centrifugal Loading Displacement by Blade Type

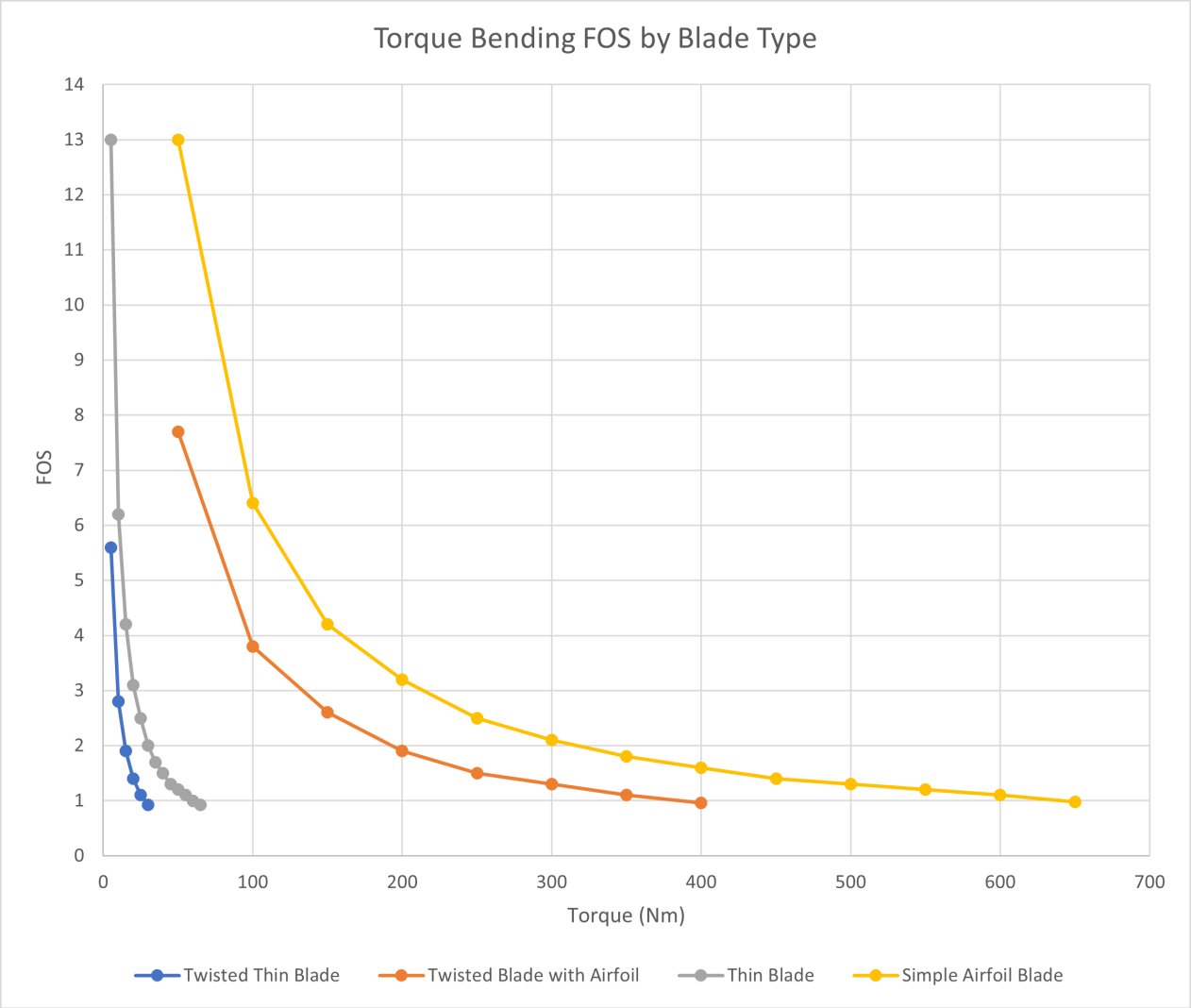

Figure 86: Torque Bending FOS by Blade Type

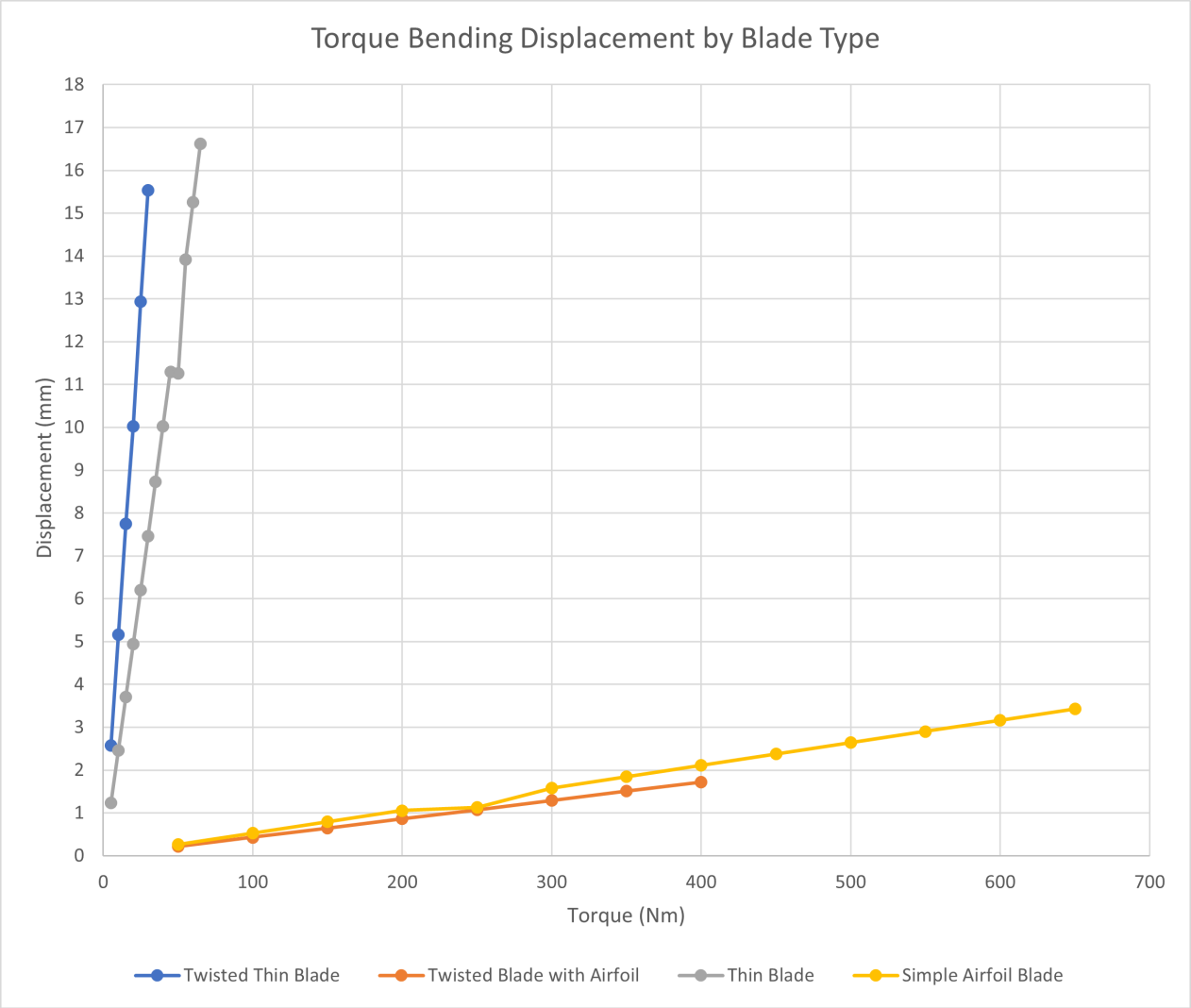

Figure 87: Torque Bending Displacement by Blade Type

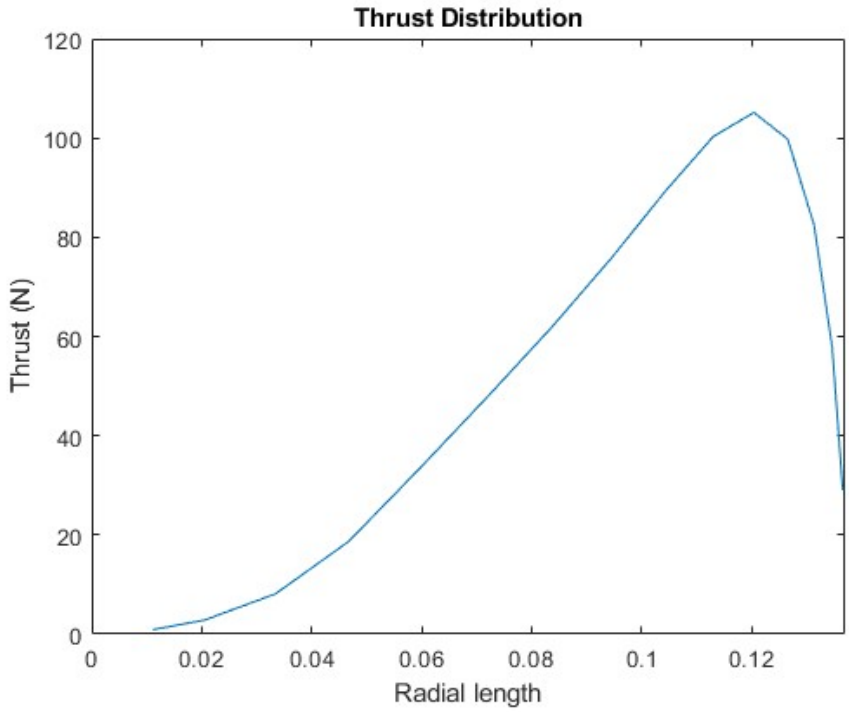

Figure 88: Test Assembly Thrust Distribution

4.5 Propeller Blade with Expected Forces Results

In the previous section, the failure modes were explored by individual loading situation on each type of blade. However, in a real application, these forces act simultaneously. Steps were taken to simulate realistic loading conditions at a given speed. The thrust and torque components were determined at a given speed, and these were used to apply to a study where all 3 loading situations were combined for each blade.

4.5.1 Thrust and Torque Distributions

The thrust and torque distributions for each propeller blade geometry type was determined at 12,000RPM. Radial length was measured in meters (Figures 88-97).

4.5.2 Combined Loading FEA

The thrust and torque components for each propeller blade geometry were determined at a given speed, 12,000 RPM. These values were used to simulate realistic loading conditions.

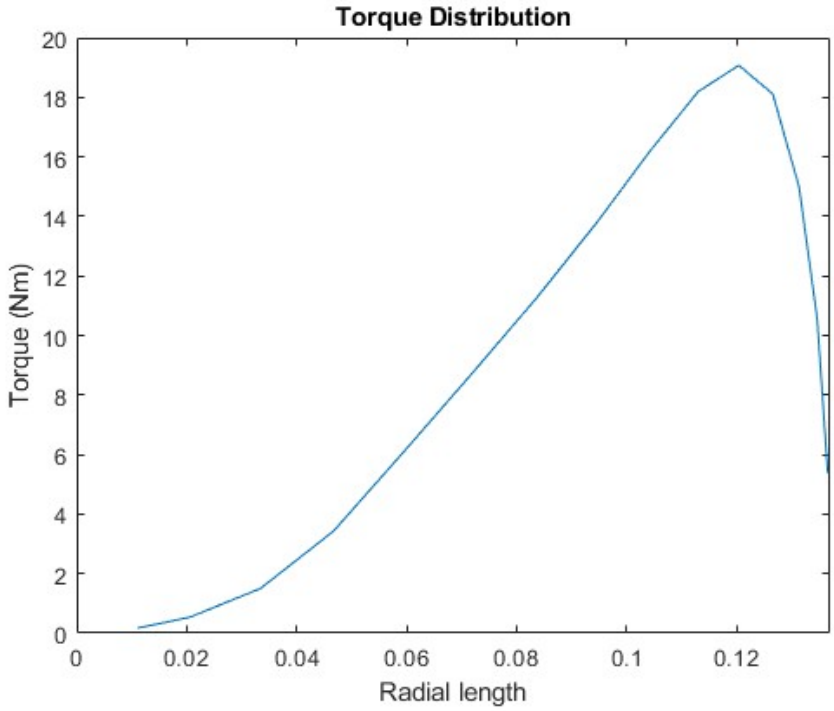

Figure 89: Test Assembly Torque Distribution

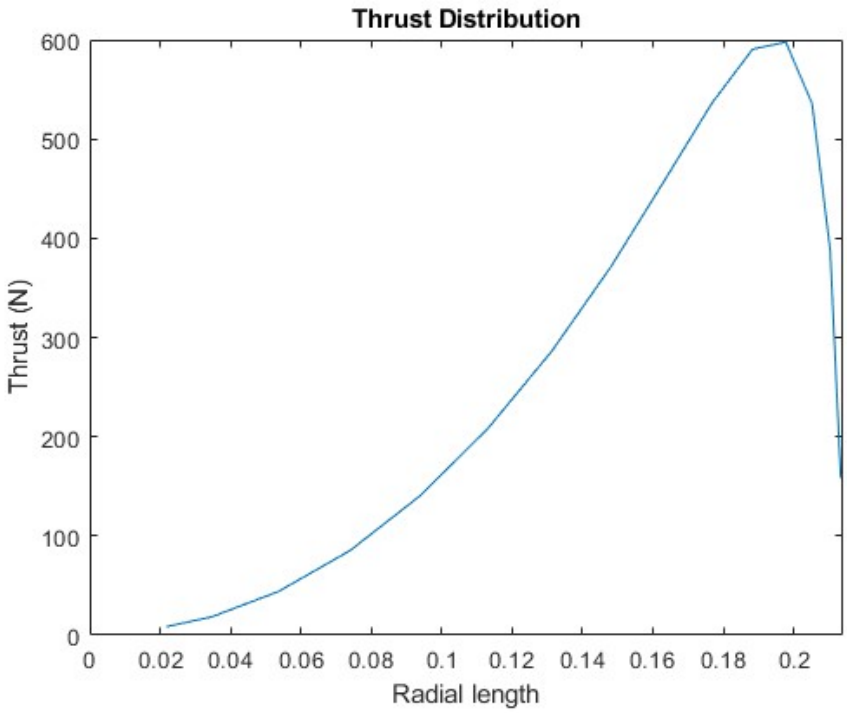

Figure 90: Thin Blade Thrust Distribution

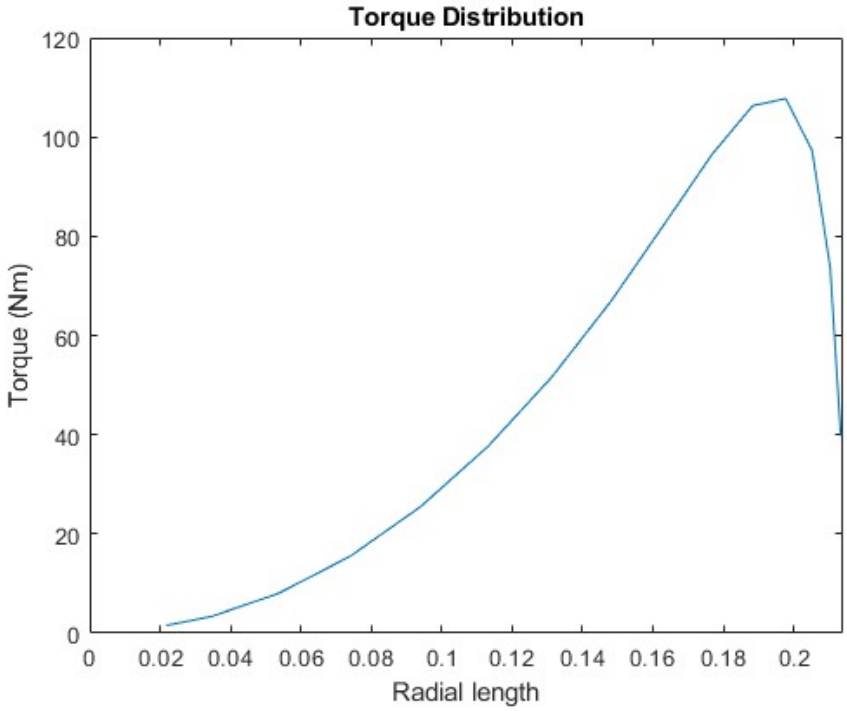

Figure 91: Thin Blade Torque Distribution

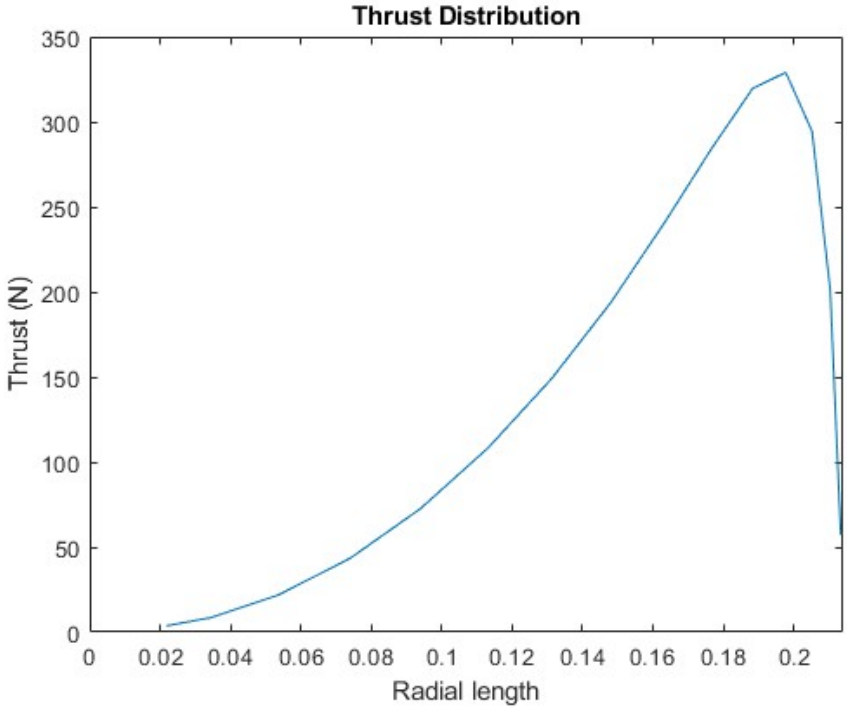

Figure 92: Simple Airfoil Blade Thrust Distribution

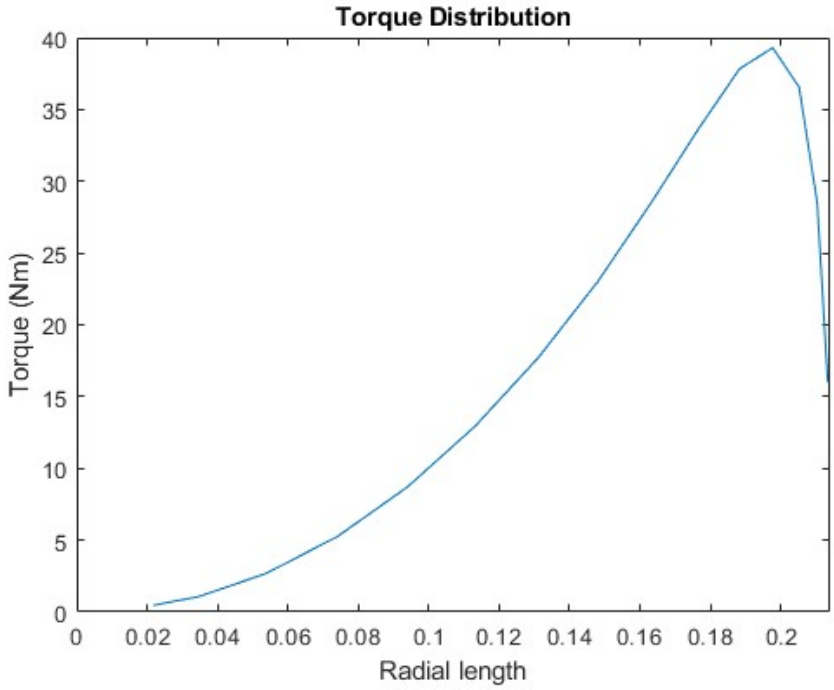

Figure 93: Simple Airfoil Blade Torque Distribution

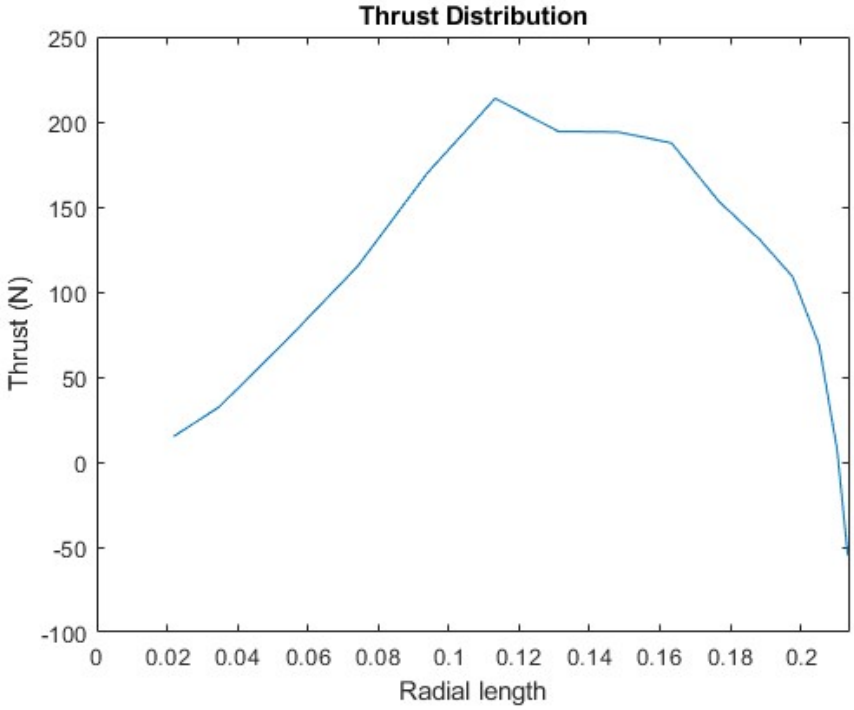

Figure 94: Twisted Thin Blade Thrust Distribution

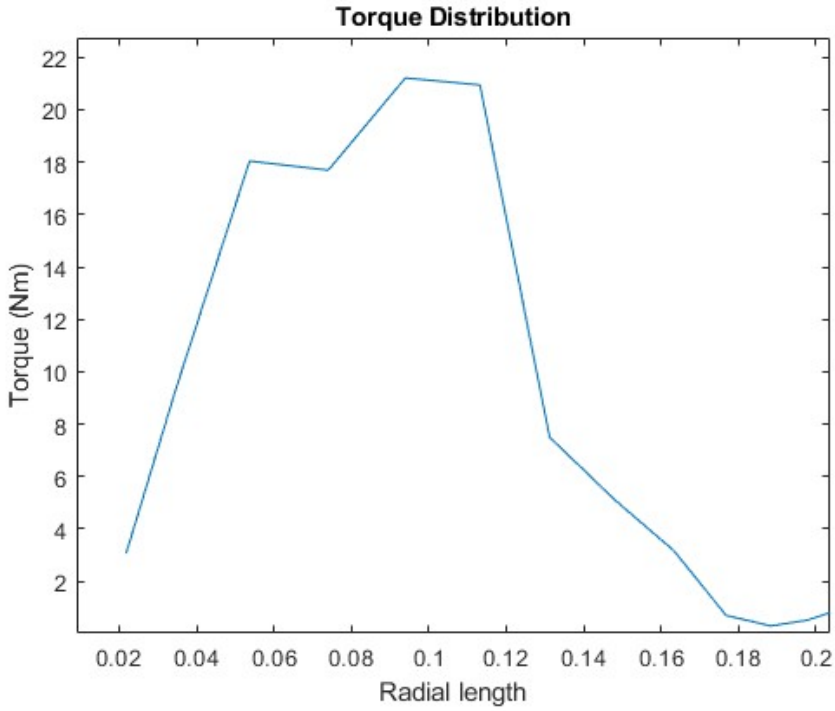

Figure 95: Twisted Thin Blade Torque Distribution

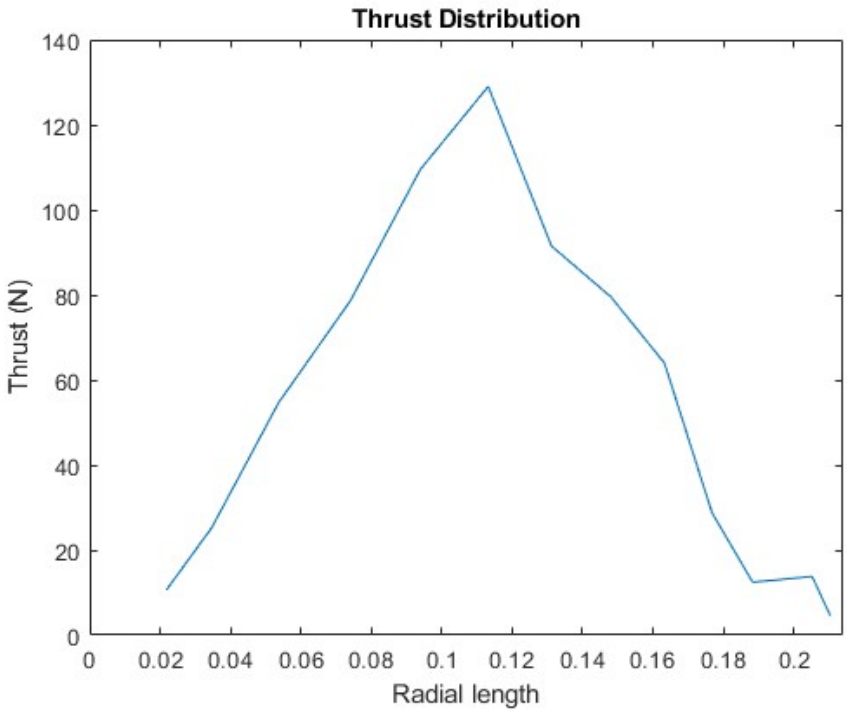

Figure 96: Twisted Blade with Airfoil Thrust Distribution

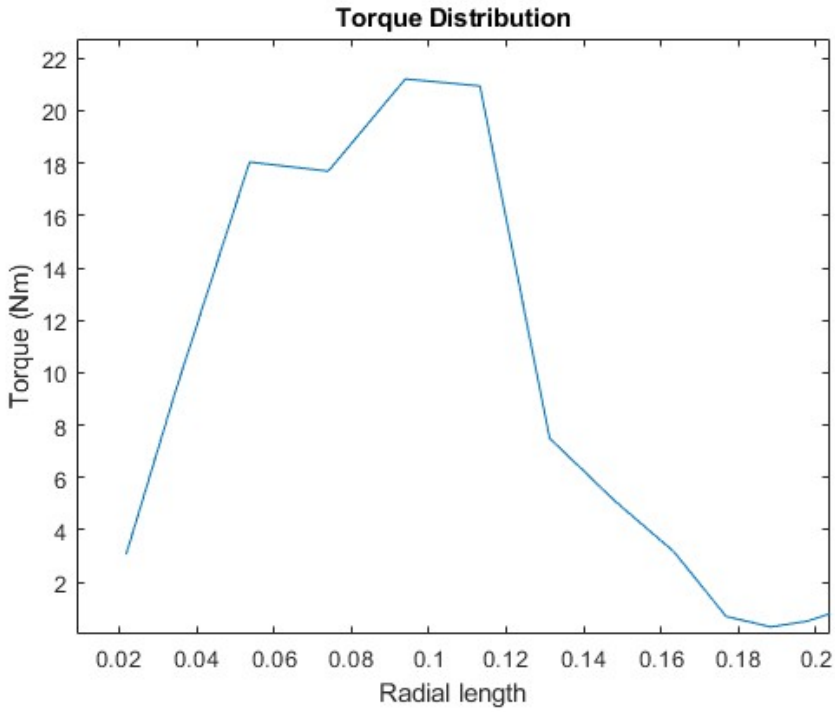

Figure 97: Twisted Blade with Airfoil Torque Distribution

Thrust Force Applied	Resultant Thrust Radial Location	Torque Applied	Rad/s	RPM	FOS-Mohr Coulomb	Max Displacement
6.37N	0.0953m	1.16Nm	1256	12,000	3.2	0.4031mm

Table 22: Test Assembly Combined Loading at 12,000 RPM

Test Assembly

The test assembly combined loading was simulated using the values in 22. The FOS was 3.2 and the max displacement was 0.4031mm (Figures 98 and 99). The stress and strain at 12,000 RPM were captured in 101 and 100.

Twisted Blade with Airfoil

The test assembly combined loading was simulated using the values in 23. The FOS was 2.5 and the max displacement was 0.3505mm (Figures 114 and 103). The stress and strain at 12,000 RPM were captured in 104 and 105.

Thrust Force Applied	Resultant Thrust Radial Location	Torque Applied	Rad/s	RPM	FOS-Mohr Coulomb	Max Displacement
11.61N	0.1164m	1.83Nm	1256	12,000	2.5	0.3505mm

Table 23: Twisted Blade with Airfoil Combined Loading at 12,000 RPM

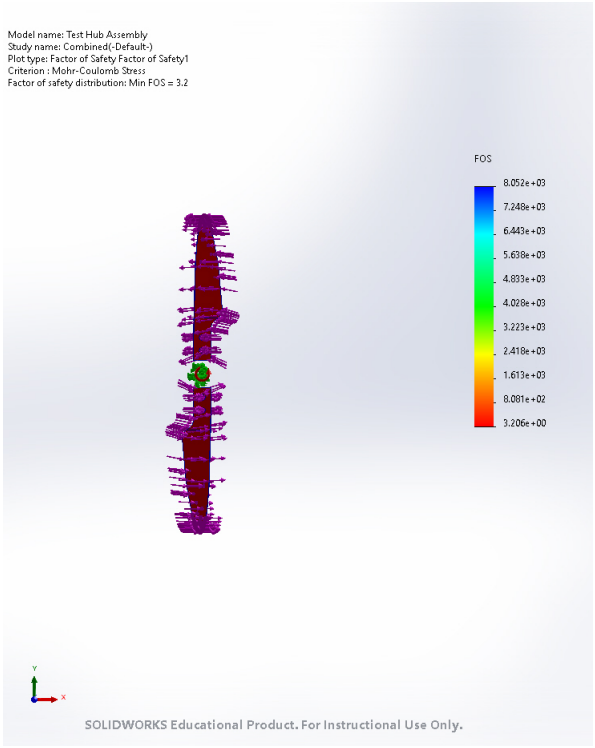

Figure 98: Test Assembly FOS at 12,000RPM-Combined Loading

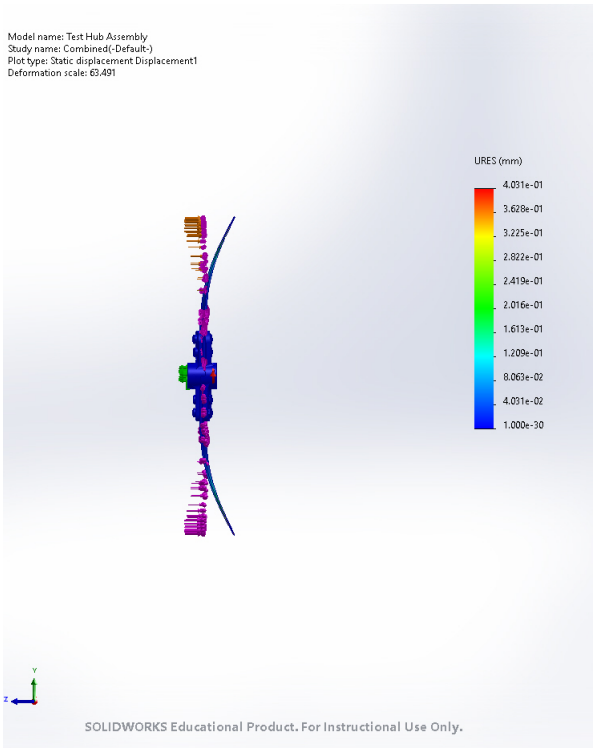

Figure 99: Test Assembly Displacement at 12,000RPM-Combined Loading

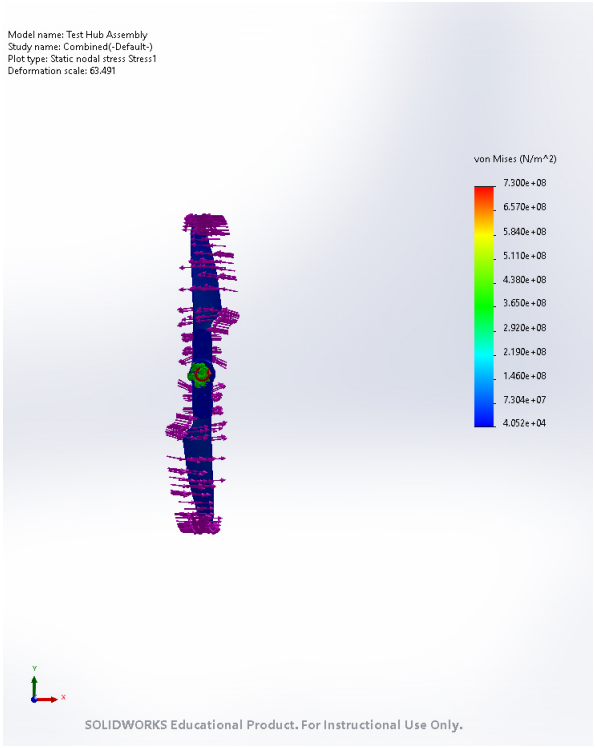

Figure 100: Test Assembly Stress at 12,000RPM-Combined Loading

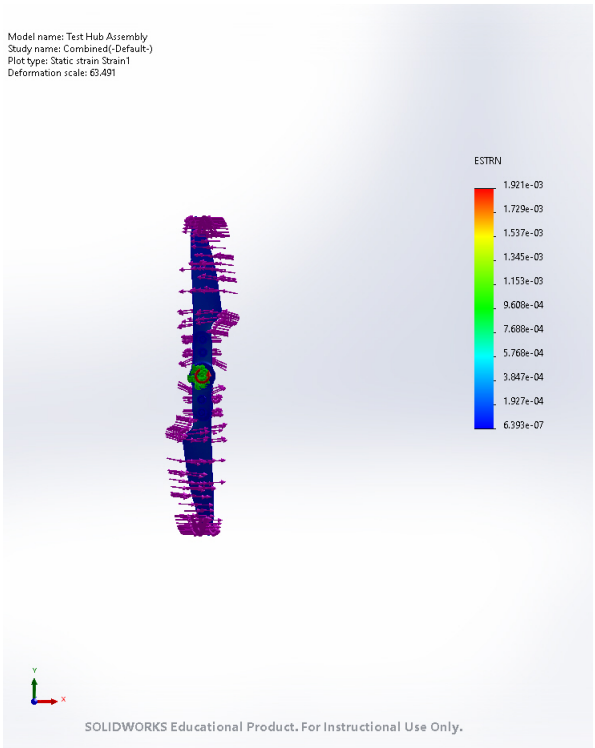

Figure 101: Test Assembly Stress at 12,000RPM-Combined Loading

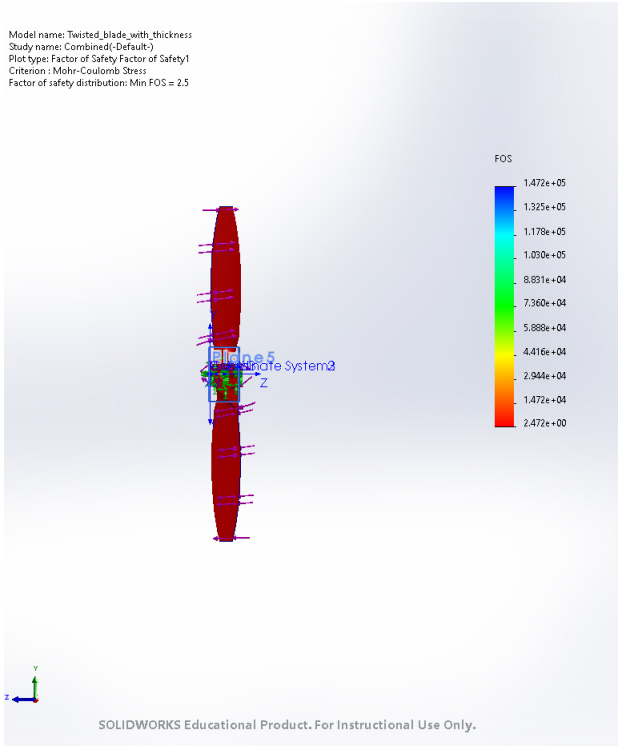

Figure 102: Twisted Blade with Airfoil FOS at 12,000RPM-Combined Loading

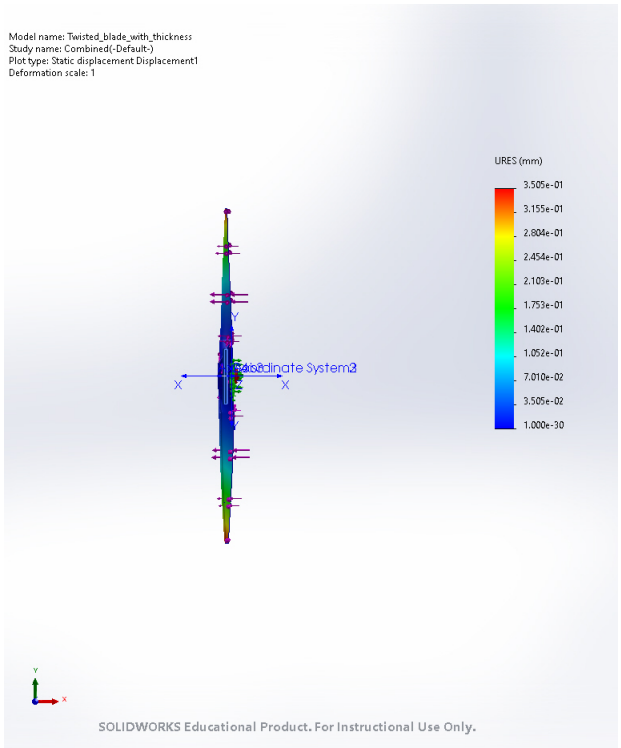

Figure 103: Twisted Blade with Airfoil Displacement at 12,000RPM-Combined Loading

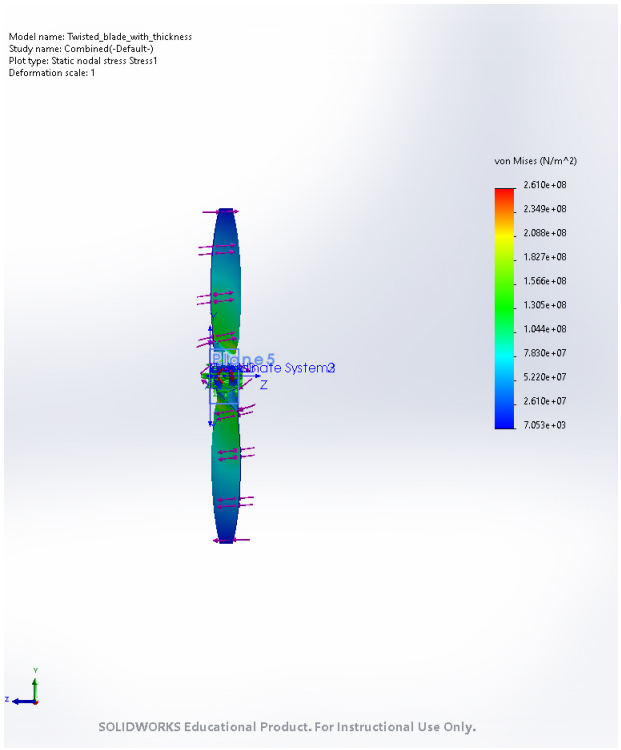

Figure 104: Twisted Blade with Airfoil Stress at 12,000RPM-Combined Loading

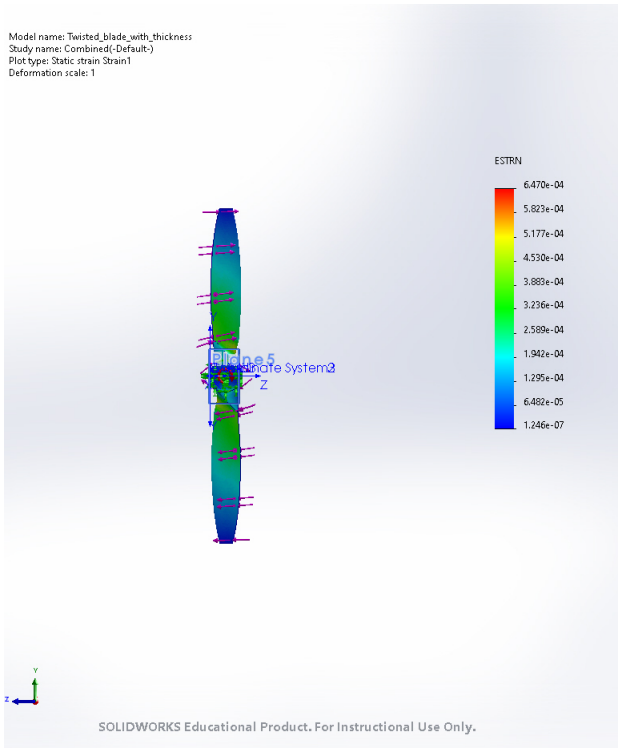

Figure 105: Twisted Blade with Airfoil Stress at 12,000RPM-Combined Loading

Thrust Force Applied	Resultant Thrust Radial Location	Torque Applied	Rad/s	RPM	FOS-Mohr Coulomb	Max Displacement
52.32N	0.1292m	9.44Nm	1256	12,000	1.5	1.468mm

Table 24: Thin Blade Combined Loading at 12,000 RPM

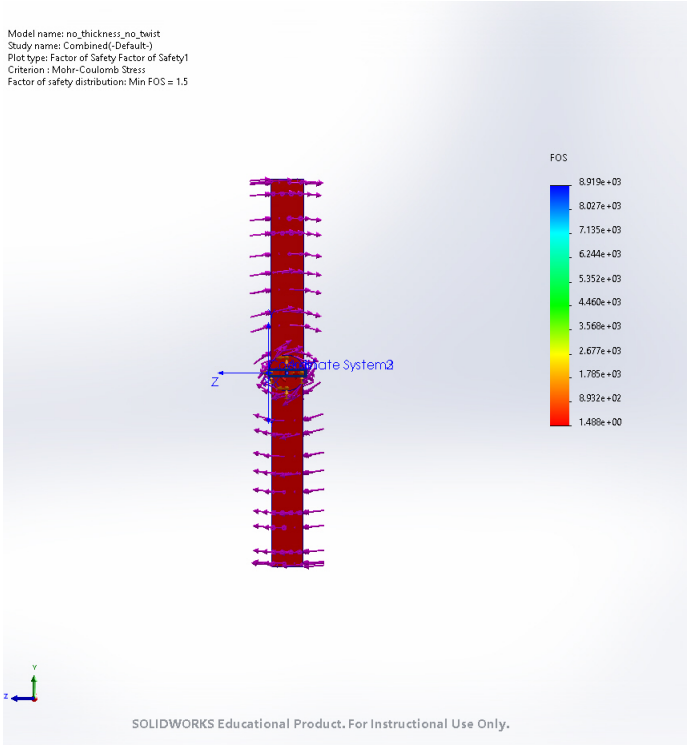

Figure 106: Thin Blade FOS at 12,000RPM-Combined Loading

Thin Blade

The test assembly combined loading was simulated using the values in 24. The FOS was 1.5 and the max displacement was 1.468mm (Figures 106 and 107). The stress and strain at 12,000 RPM were captured in 108 and 109.

Simple Airfoil Blade

The test assembly combined loading was simulated using the values in 25. The FOS was 1.7 and the max displacement was 0.5299mm (Figures 110 and 111. The stress and strain at 12,000 RPM were captured in 112 and 113.

Thrust Force Applied	Resultant Thrust Radial Location	Torque Applied	Rad/s	RPM	FOS-Mohr Coulomb	Max Displacement
27.66N	0.1492m	3.13Nm	1256	12,000	1.7	0.5299mm

Table 25: Simple Airfoil Blade Combined Loading at 12,000 RPM

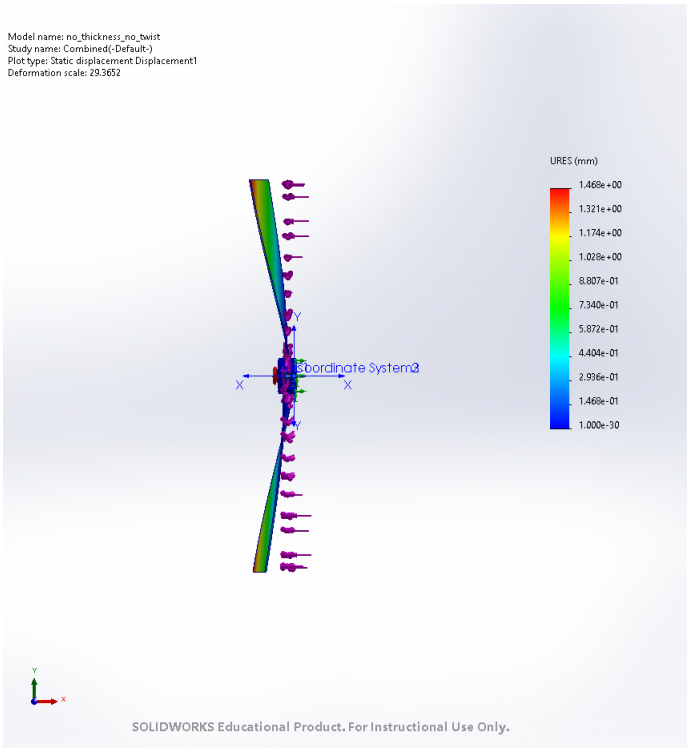

Figure 107: Thin Blade Displacement at 12,000RPM-Combined Loading

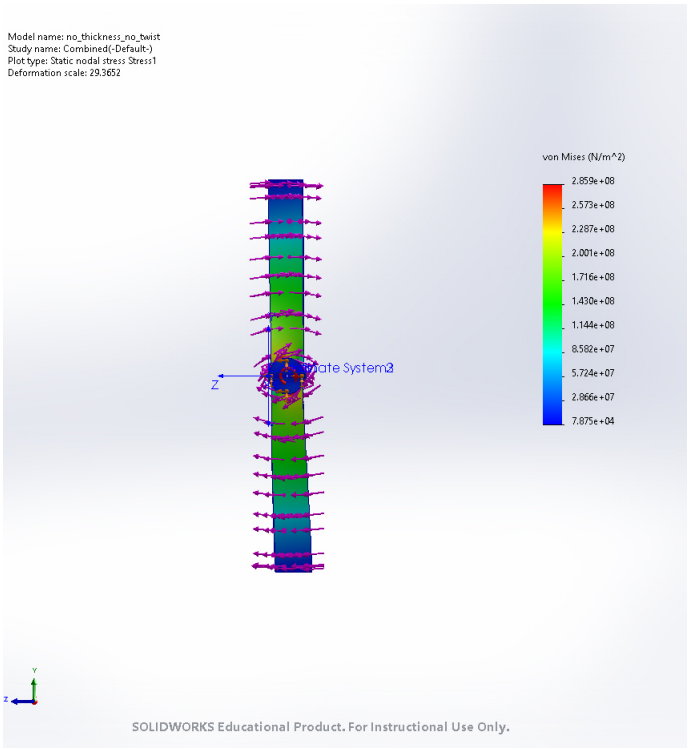

Figure 108: Thin Blade Stress at 12,000RPM-Combined Loading

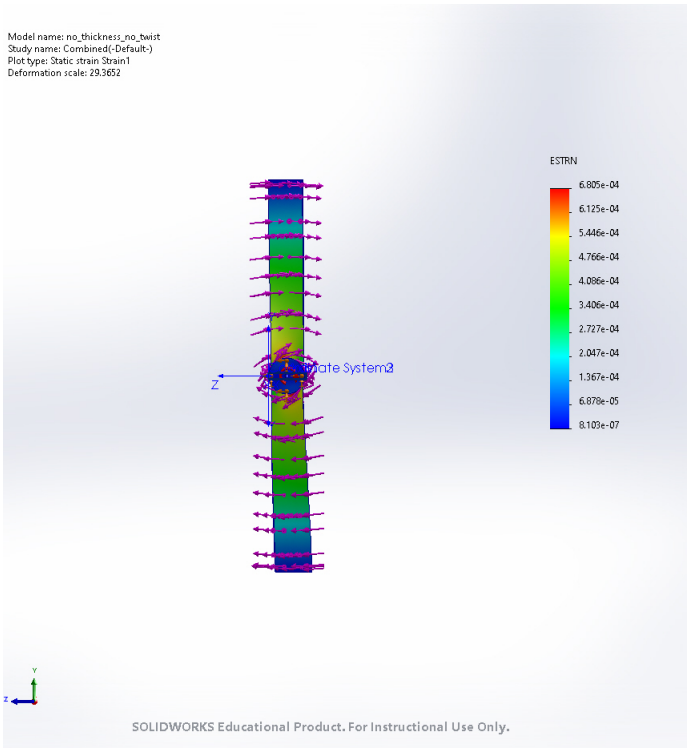

Figure 109: Thin Blade Stress at 12,000RPM-Combined Loading

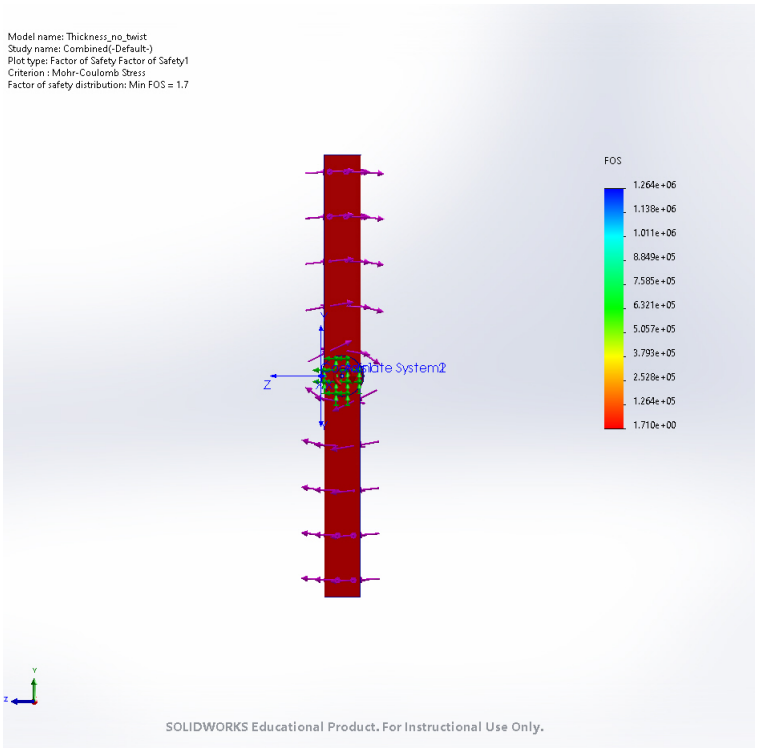

Figure 110: Simple Airfoil Blade FOS at 12,000RPM-Combined Loading

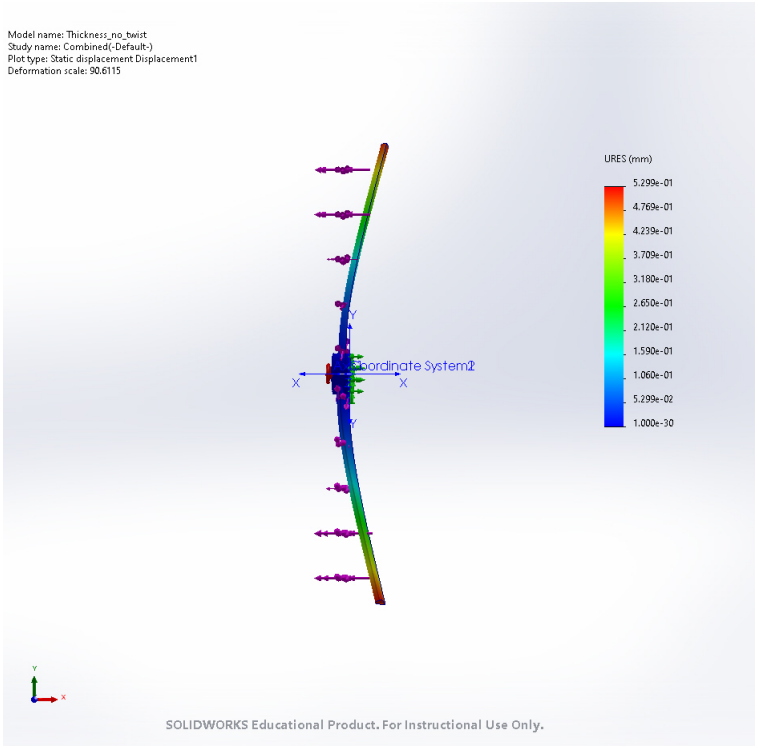

Figure 111: Simple Airfoil Blade Displacement at 12,000RPM-Combined Loading

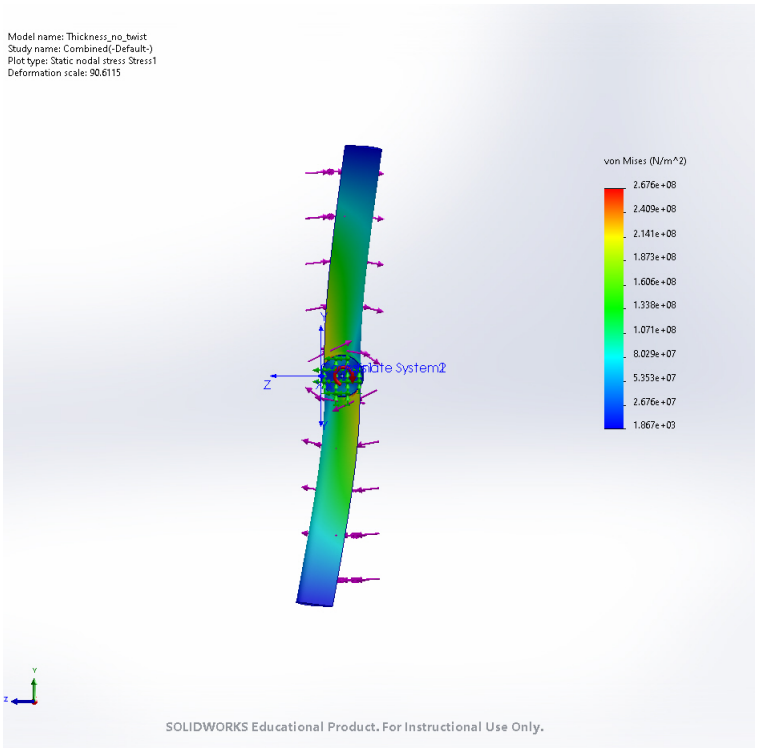

Figure 112: Simple Airfoil Blade Stress at 12,000RPM-Combined Loading

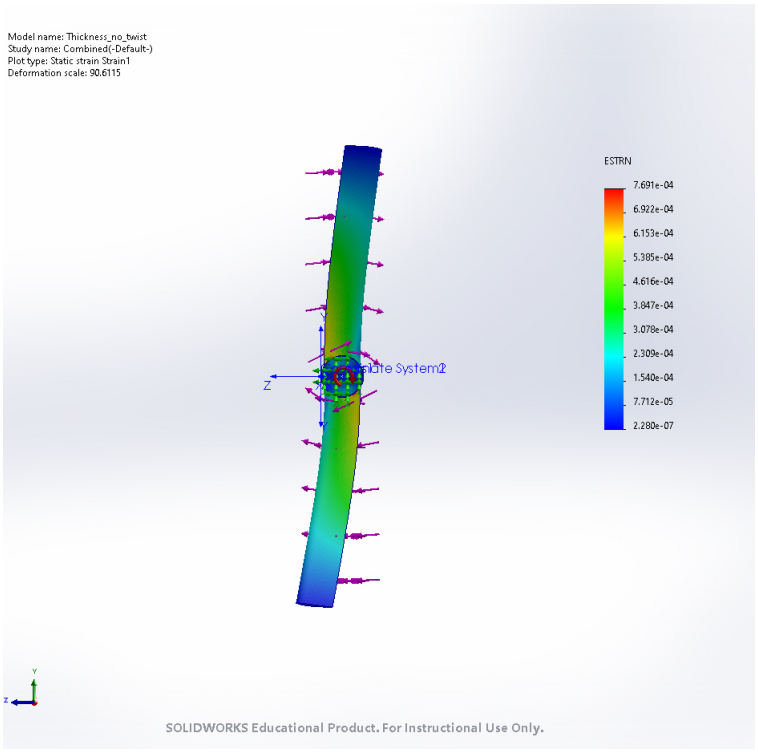

Figure 113: Simple Airfoil Blade Stress at 12,000RPM-Combined Loading

Thrust Force Applied	Resultant Thrust Radial Location	Torque Applied	Rad/s	RPM	FOS-Mohr Coulomb	Max Displacement
25.47N	0.1262m	4.24Nm	1256	12,000	1.6	0.3427mm

Table 26: Twisted Thin Blade Combined Loading at 12,000 RPM

Twisted Thin Blade

The test assembly combined loading was simulated using the values in 26. The FOS was 1.6 and the max displacement was 0.3427mm (Figures 114 and 115. The stress and strain at 12,000 RPM were captured in 116 and 117.

4.5.3 Mesh Convergence

The mesh convergence for each loading situation on each blade type was recorded in tables 28-31. The same loading situation was varied by each minimum and maximum element size using the adjustable slider in SolidWorks. The mesh type was blended-curvature based mesh, with a minimum number of elements per circle being 8 and the element size growth ratio at 1.4.

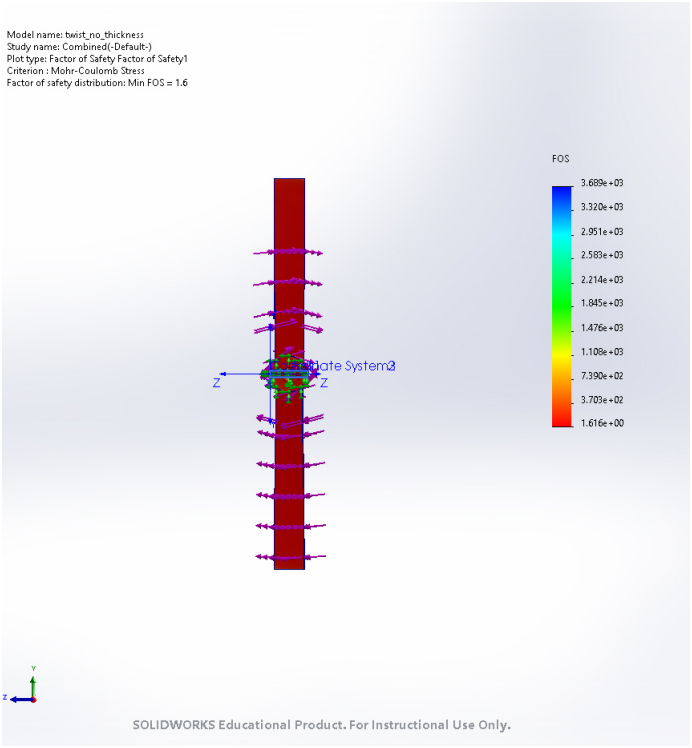

Figure 114: Twisted Thin Blade FOS at 12,000RPM-Combined Loading

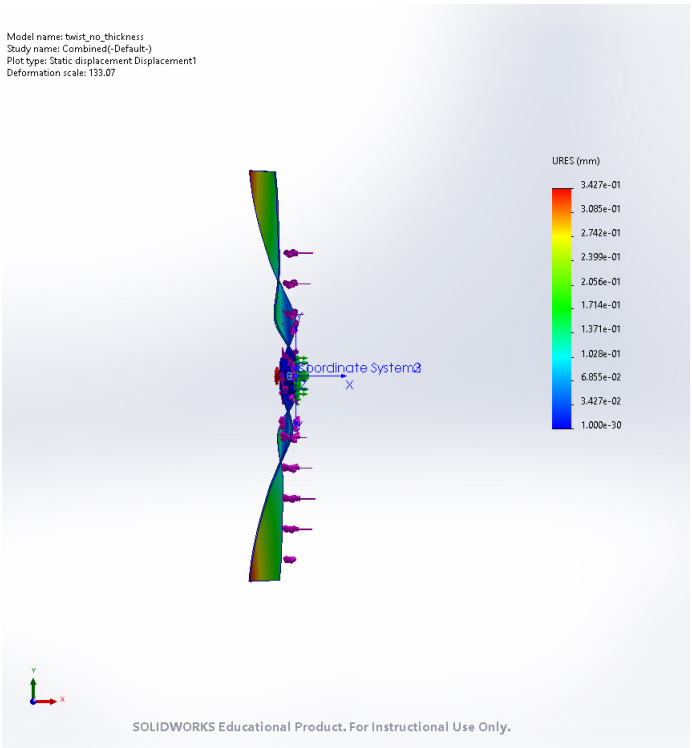

Figure 115: Twisted Thin Blade Displacement at 12,000RPM-Combined Loading

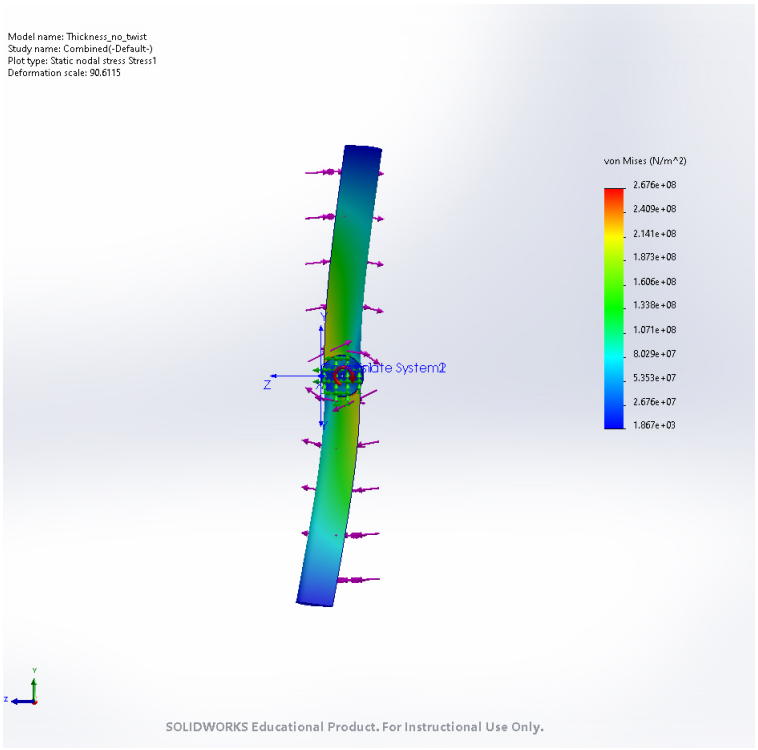

Figure 116: Twisted Thin Blade Stress at 12,000RPM-Combined Loading

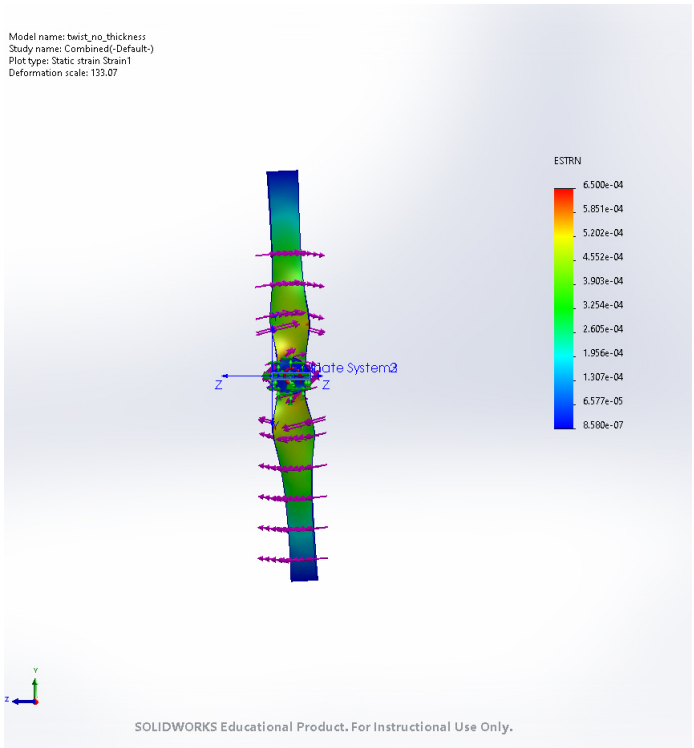

Figure 117: Twisted Thin Blade Stress at 12,000RPM-Combined Loading

Loading Applied	Max Element Size	Min Element Size	FOS-Mohr Coulomb	Max Displacement
70N Force	10.98300146mm	0.61229349mm	0.97	5.264
	9.0609762mm	0.50514213mm	0.95	5.24
	8.09996358mm	0.45156645mm	0.96	5.244
	7.13895095mm	0.39799077mm	0.94	5.251
	6.17793832mm	0.34441509mm	0.91	5.258
	5.07963817mm	0.28318574mm	0.88	5.246
	4.18726931mm	0.23343689mm	0.9	5.236
	3.3635442mm	0.18751488mm	0.92	5.228
	2.74575036mm	0.15307337mm	0.96	5.23
1989rad/sec Centrifugal	10.98300146mm	0.61229349mm	1.1	0.2706
	9.19826372mm	0.5127958mm	0.9	0.2705
	8.23725109mm	0.45922012mm	0.9	0.2736
	7.13895095mm	0.39799077mm	0.84	0.2764
	6.0406508mm	0.33676142mm	1.1	0.269
	5.07963817mm	0.28318574mm	1	0.2728
	4.18726931mm	0.23343689mm	1	0.2648
	3.15761292mm	0.17603438mm	1.1	0.2615
	2.74575036mm	0.15307337mm	1.1	0.2609
50Nm Torque	10.98300146mm	0.61229349mm	0.94	3.292
	9.88470131mm	0.55106414mm	0.94	3.291
	8.78640117mm	0.48983479mm	0.94	3.287
	7.96267606mm	0.44391278mm	0.93	3.28
	6.86437591mm	0.38268343mm	0.93	3.279
	5.90336328mm	0.32910775mm	0.93	3.276
	4.8737069mm	0.27170524mm	0.93	3.282
	3.98133803mm	0.22195639mm	0.93	3.28
	3.08896916mm	0.17220754mm	0.93	3.275
	2.74575036mm	0.15307337mm	0.93	3.272
6.37N; 1256rad/sec; 1.16Nm;	10.98300146mm	0.61229349mm	3.2	0.4001
	10.02198883mm	0.55871781mm	2.6	0.4043
	9.19826372mm	0.5127958mm	2.7	0.4018
	8.09996358mm	0.45156645mm	2.8	0.402
	7.13895095mm	0.39799077mm	2.6	0.4012
	6.0406508mm	0.33676142mm	3.2	0.3984
	5.14828193mm	0.28701257mm	3.1	0.4024
	4.18726931mm	0.23343689mm	3.2	0.4021
	3.15761292mm	0.17603438mm	3.2	0.4028
	2.74575036mm	0.15307337mm	3.2	0.4031

Table 27: Mesh Convergence-Test Assembly

Loading Applied	Max Element Size	Min Element Size	FOS-Mohr Coulomb	Max Displacement
50N Force	7.4511818mm	1.86277682mm	2.4	7.99
	6.14722498mm	2.0490545mm	2.2	8.041
	5.02954771mm	1.67649914mm	2.1	8.099
	4.09814999mm	1.36603634mm	2	8.12
	3.12018238mm	1.04005039mm	1.9	8.136
	2.23535454mm	0.74511073mm	1.9	8.149
	1.86279545mm	0.62092561mm	1.9	8.154
1000rad/sec Centrifugal	7.4511818mm	1.86277682mm	3.4	0.3483
	6.05408521mm	2.01800822mm	3.3	0.3559
	5.02954771mm	1.67649914mm	3.2	0.3569
	4.09814999mm	1.36603634mm	3.1	0.3579
	3.12018238mm	1.04005039mm	3	0.3589
	2.18878465mm	0.72958759mm	2.9	0.3599
	1.86279545mm	0.62092561mm	2.9	0.3607
30Nm Torque	7.4511818mm	2.48370243mm	2.5	7.305
	6.05408521mm	2.01800822mm	2.5	7.365
	5.02954771mm	1.67649914mm	2.3	7.412
	4.09814999mm	1.36603634mm	2.2	7.432
	3.16675226mm	1.05557353mm	2.1	7.449
	2.23535454mm	0.74511073mm	2	7.46
	1.86279545mm	0.62092561mm	2	7.464
52.32N; 1256rad/sec; 9.44Nm;	7.4511818mm	1.86277682mm	1.8	1.455
	6.05408521mm	2.01800822mm	1.7	1.46
	5.02954771mm	1.67649914mm	1.7	1.462
	4.00501022mm	1.33499006mm	1.6	1.464
	3.21332215mm	1.07109667mm	1.6	1.465
	2.32849431mm	0.77615701mm	1.5	1.467
	1.86279545mm	0.62092561mm	1.5	1.468

Table 28: Mesh Convergence-Thin Blade

Loading Applied	Max Element Size	Min Element Size	FOS-Mohr Coulomb	Max Displacement
750N Force	17.89474952mm	0.89473748mm	1.1	4.875
	16.10527457mm	0.80526373mm	1	4.884
	15.21053710mm	0.76052685mm	1.1	4.881
	14.09211525mm	0.70460576mm	1.1	4.883
	13.19737777mm	0.65986889mm	1	4.881
	12.07895593mm	0.6039478mm	1.1	4.881
	11.18421845mm	0.55921092mm	1.1	4.886
	10.28948098mm	0.51447405mm	1	4.88
	9.17105913mm	0.45855296mm	1.1	4.877
	8.16447947mm	0.40822397mm	1.1	4.877
	7.04605762mm	0.35230288mm	1	4.881
	6.15132015mm	0.30756601mm	1	4.881
	4.47368738mm	0.22368437mm	0.98	4.894
1657rad/sec Centrifugal	17.89474952mm	0.89473748mm	0.98	1.36
	16.10527457mm	0.80526373mm	1	1.362
	15.21053710mm	0.76052685mm	1	1.364
	14.09211525mm	14.09211525mm	0.99	1.36
	13.19737777mm	0.65986889mm	1	1.36
	12.07895593mm	0.6039478mm	1	1.361
	10.28948098mm	0.51447405mm	1	1.356
	9.17105913mm	0.45855296mm	0.98	1.357
	8.16447947mm	0.40822397mm	1	1.356
	7.04605762mm	0.35230288mm	0.98	1.359
	6.15132015mm	0.30756601mm	1	1.36
	4.47368738mm	0.22368437mm	0.9	1.361
650Nm Torque	17.89474952mm	0.89473748mm	1.1	3.417
	16.10527457mm	0.80526373mm	1.1	3.421
	15.21053710mm	0.76052685mm	1.1	3.421
	14.09211525mm	0.70460576mm	1	3.421
	13.19737777mm	0.65986889mm	1.1	3.419
	12.07895593mm	0.6039478mm	1.1	3.421
	10.96053408mm	0.5480267mm	1.1	3.419
	10.06579661mm	0.50328983mm	1.1	3.419
	8.94737476mm	0.44736874mm	1.1	3.42
	8.05263729mm	0.40263186mm	1.1	3.42
	7.15789981mm	0.35789499mm	1.1	3.421
	6.15132015mm	0.30756601mm	1.1	3.42
	5.25658267mm	0.26282913mm	1	3.428
27.66N; 1256rad/sec; 3.13Nm;	17.89474952mm	0.89473748mm	1.8	0.5306
	16.10527457mm	0.80526373mm	1.9	0.5302
	15.21053710mm	0.76052685mm	1.9	0.5321
	14.09211525mm	0.70460576mm	1.9	0.5297
	13.19737777mm	0.65986889mm	1.9	0.5301
	11.85527156mm	0.59276358mm	1.9	0.5288
	10.06579661mm	0.50328983mm	1.9	0.53
	9.17105913mm	0.45855296mm	1.8	0.5283
	8.16447947mm	0.40822397mm	1.8	0.528
	7.04605762mm	0.35230288mm	1.8	0.5293
	6.15132015mm	0.30756601mm	1.9	0.5295
	4.47368738mm	0.22368437mm	1.7	0.5299

Table 29: Mesh Convergence-Simple Airfoil Blade

Loading Applied	Max Element Size	Min Element Size	FOS-Mohr Coulomb	Max Displacement
50N Force	7.37158175mm	1.84287701mm	1.2	16.03
	6.08155494mm	2.02716471mm	1.2	16.15
	5.06796245mm	1.68930392mm	1.1	16.2
	4.05436996mm	1.35144314mm	1.1	16.24
	3.13292224mm	1.04429697mm	1	16.27
	1.84289544mm	0.61429234mm	0.99	16.3
1657rad/sec Centrifugal	7.37158175mm	1.78144778mm	1.2	0.2554
	6.08155494mm	2.02716471mm	1.1	0.2543
	5.16010723mm	1.72001854mm	1.1	0.2534
	4.14651473mm	1.38215776mm	1.1	0.2566
	3.08684986mm	1.02893966mm	1	0.259
	1.84289544mm	0.61429234mm	0.98	0.2615
5Nm Torque	7.37158175mm	2.45716934mm	6.7	2.535
	6.08155494mm	2.02716471mm	6.3	2.556
	5.06796245mm	1.68930392mm	6	2.567
	4.14651473mm	1.38215776mm	5.9	2.574
	3.08684986mm	1.02893966mm	5.6	2.58
	2.02718498mm	0.67572157mm	5.4	2.584
	1.84289544mm	0.61429234mm	5.3	2.585
25.47N; 1256rad/sec; 20Nm;	7.37158175mm	1.84287701mm	2	0.2396
	6.08155494mm	2.02716471mm	2	0.2389
	5.06796245mm	1.68930392mm	1.9	0.2382
	4.14651473mm	1.38215776mm	1.9	0.2382
	3.17899463mm	1.05965428mm	1.8	0.238

Table 30: Mesh Convergence-Twisted Thin Blade

Loading Applied	Max Element Size	Min Element Size	FOS-Mohr Coulomb	Max Displacement
1000N Force	17.28970204mm	0.8644851mm	1	3.08
	15.12848929mm	0.75642446mm	0.93	3.08
	14.26400419mm	0.71320021mm	0.94	3.08
	13.18339781mm	0.65916989mm	0.96	3.08
	12.10279143mm	0.60513957mm	0.95	3.08
	10.15769995mm	0.507885mm	0.95	3.08
	9.7254574mm	0.48627287mm	0.95	3.08
	8.32066911mm	0.41603346mm	0.95	3.08
	7.34812337mm	0.36740617mm	0.97	3.08
	6.15945635mm	0.30797282mm	0.96	3.08
	5.40303189mm	0.27015159mm	0.96	3.079
	4.32242551mm	0.21612128mm	0.97	3.078
2094rad/sec Centrifugal	17.28970204mm	0.8644851mm	0.92	0.6169
	15.34461056mm	0.76723053mm	0.92	0.617
	14.26400419mm	0.71320021mm	0.91	0.617
	13.39951908mm	0.66997595mm	0.91	0.617
	12.10279143mm	0.60513957mm	0.91	0.6171
	10.15769995mm	0.507885mm	0.91	0.6171
	9.29321485mm	0.46466074mm	0.91	0.6171
	8.21260847mm	0.41063042mm	0.92	0.6171
	7.24006273mm	0.36200314mm	0.92	0.6171
	6.26751699mm	0.31337585mm	0.91	0.6171
	5.29497125mm	0.26474856mm	0.91	0.6174
	4.43048615mm	0.22152431mm	0.91	0.6175
	4.32242551mm	0.21612128mm	0.91	0.6176
400Nm Torque	17.28970204mm	0.8644851mm	1.1	1.723
	15.34461056mm	0.76723053mm	1.2	1.723
	14.26400419mm	0.71320021mm	1.2	1.723
	13.18339781mm	0.65916989mm	1.2	1.723
	12.10279143mm	0.60513957mm	1.1	1.723
	10.15769995mm	0.507885mm	0.99	1.723
	9.29321485mm	0.46466074mm	1.1	1.723
	8.32066911mm	0.41603346mm	1.1	1.723
	7.24006273mm	0.36200314mm	0.95	1.723
	6.26751699mm	0.31337585mm	1	1.723
	5.29497125mm	0.26474856mm	1	1.722
	4.8627287mm	0.24313644mm	1	1.722
	4.32242551mm	0.21612128mm	0.96	1.722
11.61NN; 1256rad/sec; 1.83Nm;	17.28970204mm	0.8644851mm	2.5	0.3502
	15.12848929mm	0.75642446mm	2.5	0.3503
	14.04788291mm	0.70239415mm	2.5	0.3505
	13.18339781mm	0.65916989mm	2.5	0.3502
	12.10279143mm	0.60513957mm	2.5	0.3503
	10.15769995mm	0.507885mm	2.5	0.3503
	9.07709357mm	0.45385468mm	2.5	0.3503
	8.10454783mm	0.40522739mm	2.5	0.3504
	7.24006273mm	0.36200314mm	2.5	0.3503
	6.05139572mm	0.30256979mm	2.5	0.3505
	5.18691061mm	0.25934553mm	2.5	0.3504
	4.32242551mm	0.21612128mm	2.5	0.3505

Table 31: Mesh Convergence-Twisted Blade with Airfoil

CHAPTER V

Discussion

5.1 3D Scanning

The difference in the airfoil trailing edges shows that the trailing edge lost sharpness in the 3D scanning process. Some of this 2.77% error was due to shrinkage in the 3D printing process (1.25%) but the rest of it was due to the error in the scanning process itself (1.52%). This must be accounted for in modelling of propellers when looking at sections of airfoil geometries. The difference is not very large, but the modelling process should take into account a need for a minor correction on the trailing edge from the scanned data.

The sectioned method was sufficient to collect data on the structural loading. Multiple assumptions were made from the scanned data, such as the airfoil type. There could be some minor error in the pitch measurements as well as the thickness due to limitations with the scanner.

5.2 Test Assembly FEA

The primary forces on a spinning propeller were modeled using FEA. The ceramic knives, as expected, showed minimal deflection as they are quite stiff. However, the modeled ceramic knives are assumed to be in ideal conditions, and there is a possibility that the ceramic knives fail at a lower value than what is modeled. Ceramics are prone to small imperfections in the manufacturing process, and as a brittle material, these are generally the site of cracks

that lead to failure of the component. It can be expected that a large enough force on an imperfection will cause the part to fail, and in a brittle fracture mode. This is concerning given the variation of direction the expected forces will be in. Failure in a brittle fracture mode during a dynamic application is not ideal.

The centrifugal loading situation is the most concerning failure situation. If the test assembly failed in this model, the brittle pieces of the fracture would separate from the assembly at a high tangential velocity in an unpredictable direction. Translating this failure mode into a real-life device, such a form of failure would result in sharp pieces of ceramic being launched in any direction from elevation and the remaining propellers would likely fracture on impact in the resulting crash. A significant safety factor would need to be implemented to avoid this catastrophic failure mode, which has implications on the ability to generate thrust.

The flexural strength of the ceramic knives in thrust bending was adequate. The deflection was low, which would have a positive effect on the performance of the propeller. The results had similar implications for the torque bending tests as well. Minimal deflection is ideal for performance. But this comes at the price of a total loss of the propellers in any failure situation and a significant safety risk. Stiffness at the cost of toughness means that the blades will shatter under certain forces. An unexpected impact will likely lead to the failure of the blade. The ceramic knives are a relatively low complexity geometry compared to a well designed propeller.

5.3 Finite Element Analysis By Propeller Blade Geometry

In thrust, the presence of an airfoil had a clear structural advantage over the thin blade types. This is due to the added thickness. Additionally, the displacement was more pronounced for the thin blade types, regardless of twist. Thickness of the propeller blade is necessary to endure performance and integrity of the propeller blade in thrust. Similar to the thrust bending analysis, the added thickness of an airfoil positively affected both torque at failure

and drove the deflection down. Structurally, an airfoil maintains the integrity of the propeller blade.

Centrifugal loading failure is the most concerning failure mode for all types. The RPM of the blade drives the other factors in this failure analysis study. All blade types fail between 16,000-19,000 RPM. However, the blade geometry affected the deflection. The presence of a twist drove the deflection down due and the added weight of an airfoil drove the deflection up.

Structurally, the propeller blade needs a twist to control failure in the centrifugal mode due to the relative velocity at the propeller tip. Added weight affects the centrifugal loading endurance. However, the propeller must also be able to withstand flexural loads in the thrust and torque directions, which is best with added thickness. From this analysis, the twisted blade with an airfoil balances the structural needs from all 3 failure modes as shown in Figure 118 as compared to 119.

For the thin blade, the thrust drove the deflection direction. The highest deflection was at the blade tips and the highest stress and strain was at the hub interface. For the twisted thin blade, this was true as well. However, for the simple airfoil blade type, the thrust did not drive the deflection direction, and the main deflection was in the opposing direction, driven by the torque and centrifugal loading. Deflection was minimal for the twisted blade with airfoil. All meshes showed adequate convergence for the conclusions drawn in this study. Figure 120 was plotted as an example. As the mesh element size is lowered, the results do not change significantly.

5.4 Manufacturing and Application Implications

The propeller geometries with the added thickness of an airfoil showed great potential for lowering efficiency-limiting deflection. However, in all geometry types as well as the test assembly, the centrifugal loading situation is the most concerning. From a manufacturing

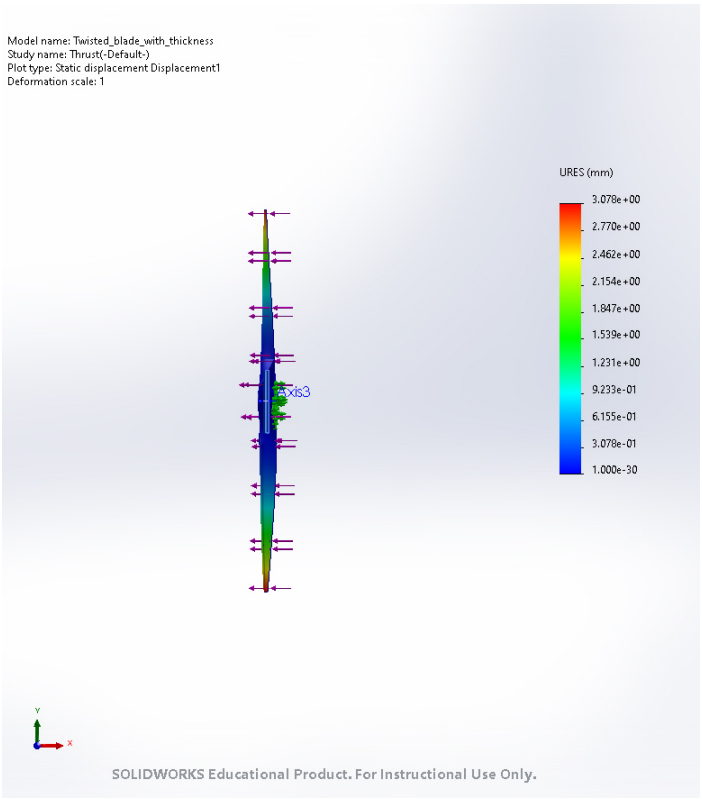

Figure 118: Twisted Blade with Airfoil Thrust Loading

perspective, this is the challenge to address. In the current application, the blades will fail in centrifugal loading long before any deflection limit is reached. The ideal geometry will be one with both the added thickness of an airfoil and a twist, which will add complexity to the manufacturing process. The propellers will also need to be balanced [4], so geometrically both sides must be the exact same or some sort of coating must be applied until balanced.

Alternatively, a hybrid propeller could be explored where the stiffness of the ceramic is leveraged in combination with the toughness of a material such as carbon-fiber reinforced polymers. In such a set-up, a ceramic core structure could maintain the flexural properties while the CFRP maintained the structural integrity during centrifugal loading. The carbon-fiber reinforced polymers would need to be 3D printed using the continuous fiber deposition method in the direction of the radial length of the blade. This would offer the weight reduction for low noise and performance requirements, flexural strength for thrust/torque bending

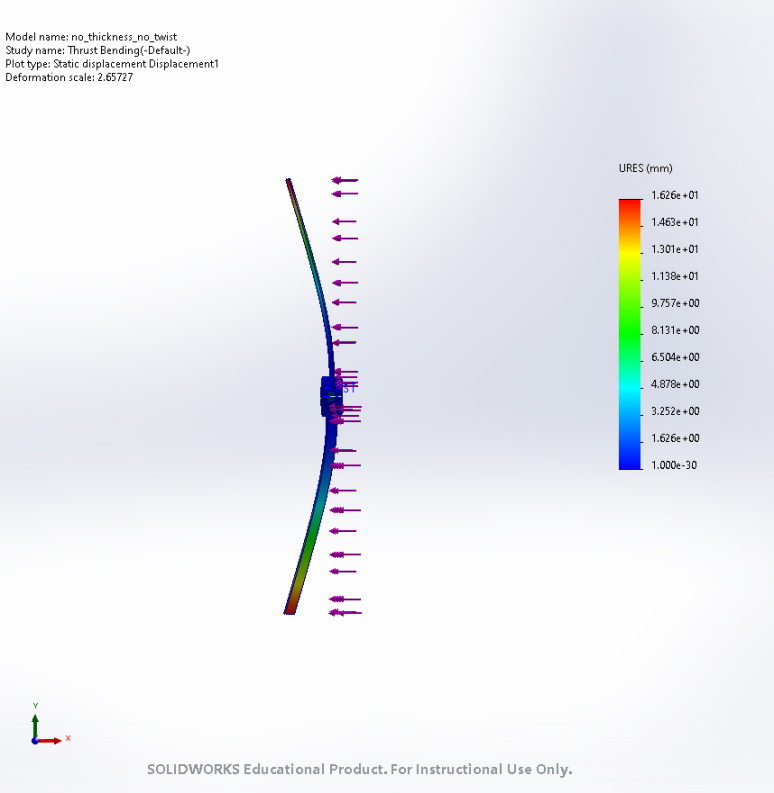

Figure 119: Thin Blade Thrust Loading

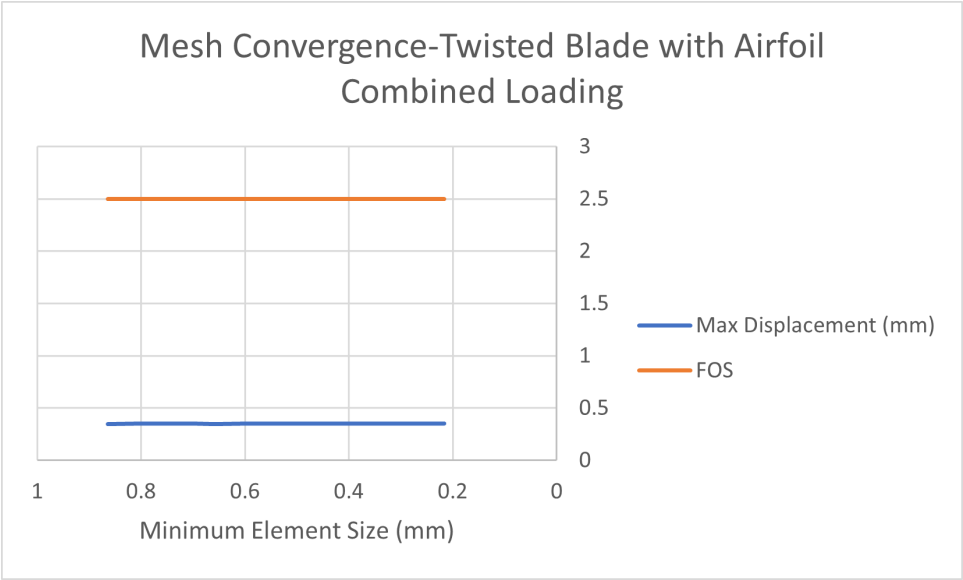

Figure 120: Example Mesh Convergence-Twisted Blade with Airfoil Combined Loading

and directional mechanical properties for the centrifugal loading mode. Ceramic coatings are another option to increase stiffness without compromising toughness in combination with another material. Vibration analysis was not performed, but is still a concern in UAS applications. When a full geometry and attachment mechanisms are defined, this will be a necessary analysis to determine other failure modes.

5.5 Conclusion

This study provided insights that can inform the design of novel ceramic propellers. This material selection holds a lot of potential to increase the efficiency and lower the sound pressure level of unmanned systems, but limitations were found as well. 3D scanning equipment was used to create SolidWorks models based on existing propellers. When this data was validated against a 3D printed part with known dimensions a minor loss of sharpness on the trailing edge of the airfoil structure was observed and accounted for in the modelling process. Multiple propeller geometries were modeled to understand how the structural changes affected the failure mode in various types of loading. Finite element modeling of thrust and torque bending showed a significant structural advantage for geometries with the added thickness of an airfoil. The twisted blade with airfoil was the most promising geometry for all loading situations. Centrifugal loading is an area of concern for all blade types. All parts failed between 16,000-19,000 RPM, which is a limiting factor for the intended application. This is the primary challenge the manufacturing process will need to address from this study.

REFERENCES

[1] Faraz Ahmad, Pushpendra Kumar, P. Pravin Patil, and Vijay Kumar, *Design and modal analysis of a quadcopter propeller through finite element analysis*, Materials today : proceedings, vol. 46, Elsevier Ltd, 2021, pp. 10322–10328 (eng).

[2] Airfoiltools.com, *Tools to search, compare and plot airfoils*, 2022, note.

[3] Gilvan Barroso, Quan Li, Rajendra K Bordia, and Günter Motz, *Polymeric and ceramic silicon-based coatings - a review*, Journal of materials chemistry. A, Materials for energy and sustainability **7** (2019), no. 5, 1936–1963 (eng).

[4] Ben Bettinger, *Manufacturing, analysis and experimental testing of multi-bladed propellers for suas*, 2012.

[5] Rajendra K. Bordia and Anand Jagota, *Crack growth and damage in constrained sintering films*, Journal of the American Ceramic Society **76** (1993), no. 10, 2475–2485 (eng).

[6] R.K. BORDIA and R. RAJ, *Sintering behavior of ceramic films constrained by a rigid substrate*, Journal of the American Ceramic Society **68** (1985), no. 6, 287–292 (eng).

[7] Michael Borish, Brian K. Post, Alex Roschli, Phillip C. Chesser, and Lonnie J. Love, *Real-time defect correction in large-scale polymer additive manufacturing via thermal imaging and laser profilometer*, Procedia manufacturing **48** (2020), no. C, 625–633 (eng).

[8] Javaid Butt, Raghunath Bhaskar, and Vahaj Mohaghegh, *Non-destructive and destructive testing to analyse the effects of processing parameters on the tensile and flexural properties of fff-printed graphene-enhanced pla*, Journal of Composites Science **6** (2022), no. 5, 148– (eng).

[9] M. Campo, A. Jiménez-Suárez, and A. Ureña, *Effect of type, percentage and dispersion method of multi-walled carbon nanotubes on tribological properties of epoxy composites*, Wear **324-325** (2015), 100–108 (eng).

[10] Inc. CerCo, *Industrial ceramic component material selection criteria*, 2019.

[11] Jiye Chen, Stephen Hallett, and Michael R. Wisnom, *Modelling complex geometry using solid finite element meshes with correct composite material orientations*, Computers structures **88** (2010), no. 9, 602–609 (eng).

[12] Tancredi Cilia, Daniele Bertetta, Paola Gualeni, Giorgio Tani, and Michele Viviani, *Additive manufacturing application to a ship propeller model for experimental activity in the cavitation tunnel*, Journal of ship production and design **35** (2019), no. 4, 364–373 (eng).

[13] Robert P Dahlgren, Ethan A Pinsker, Omar G Dary, Joab A Ogunbiyi, and Arash Alex Mazhari, *3d scanning and printing of airfoils for modular uas*, vol. 10095, SPIE, 2017, pp. 100950J–100950J–12 (eng).

[14] José Gustavo de Almeida Machado, Juliana Peixoto Rufino Gazem de Carvalho, Anna Carolina Cerqueira Neves, Felipe Perissé Duarte Lopes, Sérgio Neves Monteiro, and Carlos Mauricio Fontes Vieira, *Charpy impact test of polymer composites with epoxy resin reinforced jute fabric*, Green Materials Engineering (Cham), The Minerals, Metals Materials Series, Springer International Publishing, 2019, pp. 203–207 (eng).

[15] Maren Erdmann, Ute Niebergall, Volker Wachtendorf, and Martin Böhning, *Evaluation of uv-induced embrittlement of pe-hd by charpy impact test*, Journal of applied polymer science **137** (2020), no. 36, 49069–n/a (eng).

[16] Maria Laura Gatto, Riccardo Groppo, Michele Furlani, Alessandra Giuliani, Carlo Mangano, and Francesco Mangano, *Lithography-based ceramic manufacturing (lcm) versus milled zirconia blocks under uniaxial compressive loading: An in vitro comparative study*, Journal of dentistry **116** (2022), 103886–103886 (eng).

[17] Jiefei Gu and Puhui Chen, *A failure criterion for isotropic materials based on mohr's failure plane theory*, Mechanics research communications **87** (2018), 1–6 (eng).

[18] Muammel M. Hanon, József Dobos, and László Zsidai, *The influence of 3d printing process parameters on the mechanical performance of pla polymer and its correlation with hardness*, Procedia manufacturing **54** (2021), 244–249 (eng).

[19] Bryce Humpert, *Low noise propeller design using numerical analysis*, 2015.

[20] Reji John, Larry P. Zawada, and Joseph L. Kroupa, *Stresses due to temperature gradients in ceramic-matrix-composite aerospace components*, Journal of the American Ceramic Society **82** (1999), no. 1, 161–168 (eng).

[21] Tuchinda Karuna and Nathathai Saithongkum, *Mechanical properties of 3d printed carbon fiber composite*, Solid state phenomena **304** (2020), 15–23 (eng).

[22] Huei-Jeng Lin, Wei-Ming Lai, and Yan-Min Kuo, *Combined analytical and finite element beam model for wind turbine blades*, Journal of reinforced plastics and composites **29** (2010), no. 16, 2422–2437 (eng).

[23] P.J. Maljaars, M.L. Kaminski, and J.H. den Besten, *Finite element modelling and model updating of small scale composite propellers*, Composite structures **176** (2017), 154–163 (eng).

[24] Markforged, *Markforged material datasheet-composites*, 2022, note.

[25] Frederic Monteverde and Luigi Scatteia, *Resistance to thermal shock and to oxidation of metal diborides-sic ceramics for aerospace application*, Journal of the American Ceramic Society **90** (2007), no. 4, 1130–1138 (eng).

[26] Yuki Nakagawa, Ken-ichiro Mori, and Tomoyoshi Maeno, *3d printing of carbon fibre-reinforced plastic parts*, International journal of advanced manufacturing technology **91** (2017), no. 5-8, 2811–2817 (eng).

[27] Jamey Jacob Ranji Vaidyanathan, *Statement of work sttr phase ii: Cerfoil – high efficiency ceramic propellers for uxs*, 2021.

[28] Seyed Hamid Reza Sanei and Diana Popescu, *3d-printed carbon fiber reinforced polymer composites: A systematic review*, Journal of Composites Science **4** (2020), no. 3, 98– (eng).

[29] Uwe Scheithauer, Eric Schwarzer, Tassilo Moritz, and Alexander Michaelis, *Additive manufacturing of ceramic heat exchanger: Opportunities and limits of the lithography-based ceramic manufacturing (lcm)*, Journal of materials engineering and performance **27** (2018), no. 1, 14–20 (eng).

[30] MC Thompson, CJ Field, and MV Swain, *The all-ceramic, inlay supported fixed partial denture. part 2. fixed partial denture design: a finite element analysis: All-ceramic inlay supported fpd: a finite element analysis*, Australian dental journal **56** (2011), no. 3, 302–311 (eng).

[31] Nahum Travitzky, Alexander Bonet, Benjamin Dermeik, Tobias Fey, Ina Filbert-Demut, Lorenz Schlier, Tobias Schlordt, and Peter Greil, *Additive manufacturing of ceramic-based materials*, Advanced engineering materials **16** (2014), no. 6, 729–754 (eng).

[32] Michael D. Waldmeier, Evan H. Greener, Eugene P. Lautenschlager, and Michael D. Nowak, *Effects of simulated clinical fabrication heat treatment and artificial weathering on the hardness testing of prosthetics/orthotics polymers*, Journal of applied polymer science **60** (1996), no. 11, 2033–2037 (eng).

[33] Agnieszka Ewa Wiacek, Konrad Terpiłowski, Małgorzata Jurak, and Marta Worzakowska, *Low-temperature air plasma modification of chitosan-coated peek biomaterials*, Polymer testing **50** (2016), 325–334 (eng).

APPENDICES

Matlab Code

0.0.1 Thin Blade Thrust and Torque Calculation

```
clc;

clearvars;


%%%%% INPUTS %%%%%%%%%

RPM=12000; %rpm

rho=1.226; %desnity kg/m^3

omega=1256; %rad/sec

beta=10; %deg

R=0.214; %m


%%%%% FROM CROTOR %%%%%%%


c_over_R=[0.1683;

0.1683;

0.1683;

0.1683;

0.1683;
```

```
0.1683;
0.1683;
0.1683;
0.1683;
0.1683;
0.1683;
0.1683;
0.1683;
0.1683;
];

r_over_R=[0.102;
0.162;
0.251;
0.346;
0.439;
0.529;
0.613;
0.692;
0.763;
0.826;
0.88;
0.924;
0.959;
0.983;
0.997;
];
```

```
CL=[0.543;
0.464;
0.46;
0.467;
0.476;
0.485;
0.494;
0.503;
0.51;
0.509;
0.494;
0.454;
0.38;
0.272;
0.137;
];

CD=[0.0202;
0.0168;
0.0141;
0.0123;
0.0112;
0.0104;
0.0098;
0.0093;
0.009;
0.0087;
```

```
0.0085;

0.0083;

0.0092;

0.0165;

0.0355;

];


%%%%%%% Conversion %%%%%%%%%%%

r=r_over_R*R;

c=c_over_R*R;


%%%%%% Lift and Drag Components %%%%%%

L=(rho.*(omega.*r).^2.*c.*CL)/2;

D=(rho.*(omega.*r).^2.*c.*CD)/2;


%%%%% Thrust and Torque %%%%%%%%%%%%%%

Thrust=L.*cosd(beta)- D.*cosd(beta);

Q=L.*sind(beta)+ D.*sind(beta).*r;


%%%%%%%% Plots %%%%%%%%%%%%%%%%%%%%%%%%


figure(1)

plot(r, Thrust)

hold on

title('Thrust Distribution')

xlabel('Radial length')

ylabel('Thrust (N)')
```

```
fit=polyfit(r, Thrust, 3)
xlim([0 R])
hold off

figure(2)
plot(r, Q)
hold on
title('Torque Distribution')
xlabel('Radial length')
ylabel('Torque (Nm)')
fitQ=polyfit(r, Q, 3)
xlim([0 R])
hold off



%%%%%%% Integration %%%%%^%%%%

Curve_fit_equation=@(x)fit(1)*x.^3+fit(2)*x.^2+fit(3)*x+fit(4);
Thrust_resultant=integral(Curve_fit_equation, R,0)

x_bar=@(x)fit(1)*x.^4+fit(2)*x.^3+fit(3)*x.^2+fit(4)*x;
Resultant_loc=integral(x_bar, R, 0)/Thrust_resultant

%%%%%%%%%%%%%%%%% Torque %%%%%%%%%%%%%%%%%

Curve_fit_equationQ=@(x)fitQ(1)*x.^3+fitQ(2)*x.^2+fitQ(3)*x+fitQ(4);
Q_resultant=integral(Curve_fit_equationQ, R,0)
```

```
x_barQ=@(x)fitQ(1)*x.^4+fitQ(2)*x.^3+fitQ(3)*x.^2+fitQ(4)*x;
Resultant_locQ=integral(x_barQ, R, 0)/Q_resultant
```

0.0.2 Twisted Thin Blade Thrust and Torque Calculation

```
%%%%% INPUTS %%%%%%%%%

RPM=12000; %rpm
rho=1.226; %desnity kg/m^3
omega=1256; %rad/sec
beta=10; %deg
R=0.214; %m

%%%%% FROM CROTOR %%%%%%%

beta=[19.28;
19.99;
19.07;
15.23;
14.04;
12.44;
7.62;
6.2;
5.07;
3.36;
2.65;
2.43;
```

```
2.21;
1.78;
1.12;
];

c_over_R=[0.1683;
0.1683;
0.1683;
0.1683;
0.1683;
0.1683;
0.1683;
0.1683;
0.1683;
0.1683;
0.1683;
0.1683;
0.1683;
0.1683;
];

r_over_R=[0.102;
0.162;
0.251;
0.346;
0.439;
```

```
0.529;
0.613;
0.692;
0.763;
0.826;
0.88;
0.924;
0.959;
0.983;
0.997;
];

CL=[0.98;
0.837;
0.764;
0.636;
0.581;
0.501;
0.337;
0.265;
0.212;
0.15;
0.116;
0.096;
0.074;
0.046;
0.02;
```

```
];

CD=[0.0219;
0.0175;
0.0144;
0.0124;
0.0112;
0.0104;
0.0099;
0.0095;
0.0092;
0.009;
0.01;
0.016;
0.0271;
0.0415;
0.0546;
];

%%%%%%% Conversion %%%%%%%%%%%%
r=r_over_R*R;
c=c_over_R*R;

%%%%%% Lift and Drag Components %%%%%%
L=(rho.*(omega.*r).^2.*c.*CL)/2;
D=(rho.*(omega.*r).^2.*c.*CD)/2;
```

```
%%%% Thrust and Torque %%%%%%%%%%%%%

Thrust=L.*cosd(beta)- D.*cosd(beta);

Q=L.*sind(beta)+ D.*sind(beta).*r;


%%%%%%%% Plots %%%%%%%%%%%%%%%%%%%%%%


figure(1)

plot(r, Thrust)

hold on

title('Thrust Distribution')

xlabel('Radial length')

ylabel('Thrust (N)')

fit=polyfit(r, Thrust, 3)

xlim([0 R])

hold off


figure(2)

plot(r, Q)

hold on

title('Torque Distribution')

xlabel('Radial length')

ylabel('Torque (Nm)')

fitQ=polyfit(r, Q, 3)

xlim([0 R])

hold off


%%%%%%% Integration %%%%%^%%%%
```

```
Curve_fit_equation=@(x)fit(1)*x.^3+fit(2)*x.^2+fit(3)*x+fit(4);
Thrust_resultant=integral(Curve_fit_equation, R,0)

x_bar=@(x)fit(1)*x.^4+fit(2)*x.^3+fit(3)*x.^2+fit(4)*x;
Resultant_loc=integral(x_bar, R, 0)/Thrust_resultant

%%%%%%%%%%%%%%%%% Torque %%%%%%%%%%%%%%%%%

Curve_fit_equationQ=@(x)fitQ(1)*x.^3+fitQ(2)*x.^2+fitQ(3)*x+fitQ(4);
Q_resultant=integral(Curve_fit_equationQ, R,0)

x_barQ=@(x)fitQ(1)*x.^4+fitQ(2)*x.^3+fitQ(3)*x.^2+fitQ(4)*x;
Resultant_locQ=integral(x_barQ, R, 0)/Q_resultant
```

0.0.3 Simple Airfoil Blade Thrust and Torque Calculation

```
clc;
clearvars;

%%%% INPUTS %%%%%%%%
RPM=12000; %rpm
rho=1.226; %desnity kg/m^3
omega=1256; %rad/sec
beta=6.5; %deg
R=0.214; %m
```

```
%%%%% FROM CROTOR %%%%%%%

c_over_R=[0.1683;
0.1683;
0.1683;
0.1683;
0.1683;
0.1683;
0.1683;
0.1683;
0.1683;
0.1683;
0.1683;
0.1683;
0.1683;
0.1683;
];

r_over_R=[0.102;
0.162;
0.251;
0.346;
0.439;
0.529;
0.613;
0.692;
```

```
0.763;
0.826;
0.88;
0.924;
0.959;
0.983;
0.997;
];

CL=[0.246;
0.225;
0.234;
0.242;
0.249;
0.255;
0.26;
0.265;
0.27;
0.272;
0.269;
0.253;
0.217;
0.158;
0.08;
];

CD=[0.0205;
```

```
0.0171;
0.0143;
0.0126;
0.0114;
0.0106;
0.0099;
0.0095;
0.0091;
0.0088;
0.0086;
0.0098;
0.0151;
0.0264;
0.0437;
];

%%%%%%% Conversion %%%%%%%%%%%
r=r_over_R*R;
c=c_over_R*R;

%%%%%% Lift and Drag Components %%%%%%
L=(rho.*(omega.*r).^2.*c.*CL)/2;
D=(rho.*(omega.*r).^2.*c.*CD)/2;

%%%%% Thrust and Torque %%%%%%%%%%%%%%
Thrust=L.*cosd(beta)- D.*cosd(beta);
Q=L.*sind(beta)+ D.*sind(beta).*r;
```

```
%%%%%%%% Plots %%%%%%%%%%%%%%%%%%%%%%%

figure(1)
plot(r, Thrust)
hold on
title('Thrust Distribution')
xlabel('Radial length')
ylabel('Thrust (N)')
fit=polyfit(r, Thrust, 3)
xlim([0 R])
hold off

figure(2)
plot(r, Q)
hold on
title('Torque Distribution')
xlabel('Radial length')
ylabel('Torque (Nm)')
fitQ=polyfit(r, Q, 3)
xlim([0 R])
hold off

%%%%%%% Integration %%%%%%^%%%%

Curve_fit_equation=@(x)fit(1)*x.^3+fit(2)*x.^2+fit(3)*x+fit(4);
Thrust_resultant=integral(Curve_fit_equation, R,0)
```

```
x_bar=@(x)fit(1)*x.^4+fit(2)*x.^3+fit(3)*x.^2+fit(4)*x;
Resultant_loc=integral(x_bar, R, 0)/Thrust_resultant

%%%%%%%%%%%%%%%%% Torque %%%%%%%%%%%%%%%%%

Curve_fit_equationQ=@(x)fitQ(1)*x.^3+fitQ(2)*x.^2+fitQ(3)*x+fitQ(4);
Q_resultant=integral(Curve_fit_equationQ, R,0)

x_barQ=@(x)fitQ(1)*x.^4+fitQ(2)*x.^3+fitQ(3)*x.^2+fitQ(4)*x;
Resultant_locQ=integral(x_barQ, R, 0)/Q_resultant
```

0.0.4 Twisted Blade with Airfoil Blade Thrust and Torque Calculation

```
clc;
clearvars;

%%%%% INPUTS %%%%%%%%%
RPM=12000; %rpm
rho=1.226; %density kg/m^3
omega=1256; %rad/sec
beta=10; %deg
R=0.214; %m


%%%%% FROM CROTOR %%%%%%%

beta=[15.55;
19.81;
```

```
17.84;

12.32;

10.61;

8.87;

4.37;

3.33;

2.48;

1.03;

0.65;

0.88;

1.23;

1.31;];


c_over_R=[0.1619;

0.1454;

0.1511;

0.1621;

0.1673;

0.1695;

0.1633;

0.1541;

0.1417;

0.1256;

0.1088;

0.0932;

0.0788;

0.0621;
```

```
];

r_over_R=[0.102;
0.162;
0.251;
0.346;
0.439;
0.529;
0.613;
0.692;
0.763;
0.826;
0.88;
0.924;
0.959;
0.983;
];

CL=[0.714;
0.761;
0.652;
0.45;
0.376;
0.301;
0.168;
0.124;
0.092;
```

```
0.046;
0.03;
0.04;
0.053;
0.053;
];

CD=[0.0209;
0.0182;
0.0147;
0.0125;
0.0113;
0.0105;
0.0102;
0.0101;
0.0101;
0.0105;
0.0144;
0.0225;
0.0329;
0.0449;
];

%%%%%%% Conversion %%%%%%%%%%%
r=r_over_R*R;
c=c_over_R*R;
```

```
%%%%%% Lift and Drag Components %%%%%%
L=(rho.*(omega.*r).^2.*c.*CL)/2;
D=(rho.*(omega.*r).^2.*c.*CD)/2;

%%%%% Thrust and Torque %%%%%%%%%%%%%%
Thrust=L.*cosd(beta)- D.*cosd(beta);
Q=L.*sind(beta)+ D.*sind(beta).*r;

%%%%%%%% Plots %%%%%%%%%%%%%%%%%%%%%%%%

figure(1)
plot(r, Thrust)
hold on
title('Thrust Distribution')
xlabel('Radial length')
ylabel('Thrust (N)')
fit=polyfit(r, Thrust, 3)
xlim([0 R])
hold off

figure(2)
plot(r, Q)
hold on
title('Torque Distribution')
xlabel('Radial length')
ylabel('Torque (Nm)')
fitQ=polyfit(r, Q, 3)
```

```
xlim([0 R])
hold off

%%%%%% Integration %%%%%^%%%%

Curve_fit_equation=@(x)fit(1)*x.^3+fit(2)*x.^2+fit(3)*x+fit(4);
Thrust_resultant=integral(Curve_fit_equation, R,0)

x_bar=@(x)fit(1)*x.^4+fit(2)*x.^3+fit(3)*x.^2+fit(4)*x;
Resultant_loc=integral(x_bar, R, 0)/Thrust_resultant

%%%%%%%%%%%%%%%% Torque %%%%%%%%%%%%%%%%

Curve_fit_equationQ=@(x)fitQ(1)*x.^3+fitQ(2)*x.^2+fitQ(3)*x+fitQ(4);
Q_resultant=integral(Curve_fit_equationQ, R,0)

x_barQ=@(x)fitQ(1)*x.^4+fitQ(2)*x.^3+fitQ(3)*x.^2+fitQ(4)*x;
Resultant_locQ=integral(x_barQ, R, 0)/Q_resultant
```

0.0.5 Test Assembly Thrust and Torque Calculation

```
clearvars;

%%%%% INPUTS %%%%%%%%%
RPM=12000; %rpm
P=101325;
rho=1.226; %desnity kg/m^3
```

```
omega=1256; %rad/sec

beta=10; %deg

R=0.137; %m


%%%%% FROM CROTOR %%%%%%%


c_over_R=[0.1176;

0.1073;

0.1047;

0.1369;

0.1721;

0.1553;

0.1342;

0.1196;

0.1107;

0.1034;

0.0936;

0.077;

0.0545; 0.0353;

0.0187];


r_over_R=[0.081;

0.15;

0.244;

0.341;

0.435;

0.526;
```

```
0.611;
0.69;
0.762;
0.825;
0.879;
0.924;
0.959;
0.983;
0.997;
];

CL=[0.513;
0.511;
0.557;
0.498;
0.434;
0.471;
0.52;
0.559;
0.583;
0.597;
0.609;
0.636;
0.69;
0.714;
0.666
];
```

```
CD=[0.0363;
0.0296;
0.0245;
0.0192;
0.0159;
0.0154;
0.0153;
0.0153;
0.0152;
0.0151;
0.0153;
0.0163;
0.0185;
0.0219;
0.0279;
];

%%%%%%% Conversion %%%%%%%%%%%%
r=r_over_R*R;
c=c_over_R*R;

%%%%%% Lift and Drag Components %%%%%%
L=(rho.*(omega.*r).^2.*c.*CL)/2;
D=(rho.*(omega.*r).^2.*c.*CD)/2;

%Q_torque=P/(2*pi*RPM)
```

```
%%%% Thrust and Torque %%%%%%%%%%%%%

Thrust=L.*cosd(beta)- D.*cosd(beta);

Q=L.*sind(beta)+ D.*sind(beta).*r;


%%%%%%%% Plots %%%%%%%%%%%%%%%%%%%%%%%


figure(1)

plot(r, Thrust)

hold on

title('Thrust Distribution')

xlabel('Radial length')

ylabel('Thrust (N)')

fit=polyfit(r, Thrust, 3)

xlim([0 R])

hold off


figure(2)

plot(r, Q)

hold on

title('Torque Distribution')

xlabel('Radial length')

ylabel('Torque (Nm)')

fitQ=polyfit(r, Q, 3)

xlim([0 R])

hold off


%%%%%%% Integration %%%%%%^%%%%
```

```
Curve_fit_equation=@(x)fit(1)*x.^3+fit(2)*x.^2+fit(3)*x+fit(4);
Thrust_resultant=integral(Curve_fit_equation, R,0)

x_bar=@(x)fit(1)*x.^4+fit(2)*x.^3+fit(3)*x.^2+fit(4)*x;
Resultant_loc=integral(x_bar, R, 0)/Thrust_resultant

%%%%%%%%%%%%%%%%% Torque %%%%%%%%%%%%%%%%%

Curve_fit_equationQ=@(x)fitQ(1)*x.^3+fitQ(2)*x.^2+fitQ(3)*x+fitQ(4);
Q_resultant=integral(Curve_fit_equationQ, R,0)

x_barQ=@(x)fitQ(1)*x.^4+fitQ(2)*x.^3+fitQ(3)*x.^2+fitQ(4)*x;
Resultant_locQ=integral(x_barQ, R, 0)/Q_resultant
```

VITA

Katelynn Harmon

Candidate for the Degree of

Master of Science

Thesis: FINITE ELEMENT ANALYSIS FOR THE DESIGN OF NOVEL CERAMIC PROPELLERS

Major Field: Mechanical and Aerospace Engineering

Biographical:

Education:

Completed the requirements for the Master of Science in Mechanical and Aerospace Engineering at Oklahoma State University, Stillwater, Oklahoma in December, 2022

Completed the requirements for the Bachelor of Science in Mechanical Engineering at Oklahoma Christian University, Edmond, Oklahoma in 2017.

Experience:

Manufacturing Technology Engineer, Niagara Bottling, 2021-Present
Production Supervisor, Niagara Bottling, 2020-2021
Process Engineer, Baker Hughes, 2018-2020